Die approbierte Originalversion dieser Dissertation ist in der Hauptbibliothek der Technischen Universität Wien aufgestellt und zugänglich.
http://www.ub.tuwien.ac.at

The approved original version of this thesis is available at the main library of the Vienna University of Technology.
http://www.ub.tuwien.ac.at/eng

TECHNISCHE UNIVERSITÄT WIEN
Vienna University of Technology

Dissertation

In Situ Assessment of Sputter Target Erosion and Poisoning by Laser Reflectometry

Ausgeführt zum Zwecke der Erlangung des akademischen Grades eines Doktors der technischen Wissenschaften unter der Leitung von

a.o. Univ. Prof. Dipl.-Ing Dr. techn. Christoph Eisenmenger-Sittner
E138
Institut für Festkörperphysik
eingerreicht an der Technischen Universität Wien

Fakultät für Physik
von

Muhammad Arif
e1428895
Muthgasse 66/217, 1190 Wien

Wien on: July 27, 2017 **Signature**

Abstract

We present an experimental approach for the in-situ characterization of the surface roughness of a uniformly eroded cylindrical magnetron target based on the reflectance pattern of a laser beam. The surface of the eroded region was modeled as a random arrangement of tilted plane facets with large surface extensions as compared to the wavelength of the laser. The target surface was hit by a laser beam and the reflection of the laser was captured on the screen. A simple algorithm was used to reconstruct the surface profiles form the intensity values reflected from the facets of the eroded surface. Aluminum (Al), Copper (Cu) and Titanium (Ti) targets were sputtered for different time intervals and the surface profiles were reconstructed. From these generated profiles, the roughness parameters, RMS roughness, correlation length, skewness and kurtosis of different target materials were calculated. The results measured with this in-situ technique under high vacuum conditions without disturbing the processing parameters of the magnetron sputtering plant are in good agreement with comparable measurements using a mechanical profilometer outside the sputtering system. However, some deviation was observed for surfaces with higher roughness and mean tilt angles.

As a proof of concept, we demonstrate that this approach can be used for the in-situ monitoring of poisoning of the target during reactive magnetron sputtering. The Al and Ti targets were reactively sputtered in the presence of Nitrogen (N_2) and Oxygen (O_2), separately. From hysteresis loops of reactive gas flow and discharge voltage, the threshold flow rates of N_2 and O_2 were determined for complete poisoning of Al and Ti targets, respectively. These targets were then sputtered up to 60 minutes in metallic and poisoned modes at different flow rate of the reactive gases. For each time interval, a laser beam hit the eroded regions of the cylindrical sputtering targets and reflected images were captured. The reflected intensity distribution of the laser was utilized for the characterization of the poisoned surface. The mean tilt angle of the surface roughness for both nitride and oxide formation on the Al and Ti targets were measured from the reflected intensity profiles. A change in surface roughness of the poisoned targets was observed after different poisoning time. After poisoning, the targets were sputter cleaned in the absence of reactive gas and de-poisoning time was measured. The de-poisoning time was found to be in good agreement with the change in surface roughness of the targets.

As a step further in this direction, we investigated the effect of the target poisoning level on the microstructure, preferred orientation and composition of the deposited films.

Aluminum nitride (AlN) and Titanium nitride (TiN) films were grown on natively oxidized Silicon (Si) wafers after different poisoning levels of the respective targets. For each target, the nitride films were deposited during the first 10 min of poisoning and after 60 min of poisoning again for 10 minutes. Higher substrate temperatures were observed for both AlN and TiN samples prepared after long-term poisoning. A change in surface morphology and film structure was also observed at different poisoning levels of the targets. For AlN, for long-term poisoning, the nitrogen content was increased and the XRD peak of maximum intensity became the [103] plane. This is characteristic for piezo electric AlN material. In the case of TiN, the deposited films were transformed to Ti-rich coatings with higher compressive stress and a preferred orientation of [220] for samples prepared after long-term poisoning of the target. It was found that the different target poisoning levels and the corresponding energy of the incident particles influence the properties of the deposited films.

The method of laser reflectometry can be used for in-situ monitoring the condition of sputter targets during reactive and non-reactive sputtering to extract the surface features which may correlate with sputtering parameters. These results can also be utilized for in-situ monitoring the target poisoning and respective changes in the properties of the sputter deposited films.

Keywords:

Sputtering, Target erosion, Laser reflectometry, Surface analysis, Reactive deposition, Target poisoning, Film structure

Student Number: e1428895

Contents

1. Introduction and general overview 4

2. Fundamentals 9

2.1 Sputtering 9
2.2 Reactive sputtering 14
2.3 Surface characterization 20

3. Experimental setup 25

3.1 Roughness measurement 27
3.2 Assessment of poisoning 30
3.3 Characterization of deposited films 33

4. In-situ assessment of target roughening 36

4.1 Reflection of a beam of light from a tilted plane 37
4.2 Algorithm for the reconstruction of a linear surface profile from a diffuse reflection pattern 42
4.3 Determination of roughness parameters 45

5. Assessment of target poisoning in reactive sputtering by laser reflectometry 55

5.1 Hysteresis behaviour during reactive sputtering 56
5.2 Reflection of a laser beam from the poisoned target surface 60
5.3 Roughness evolution 62
5.4 Poisoning and deposition rate 67
5.5 De-poisoning measurement 69

6. Characterization of Aluminium and Titanium nitride films prepared by sputtering under different target poisoning conditions 73

6.1 Poisoning and hysteresis behaviour 74
6.2 Microstructure of the deposited films 77
6.3 Crystallographic orientation 80
6.4 Chemical composition 85

7. Conclusions and outlook 90

References 92

Acknowledgements 99

Appendix 100

Curriculum Vitae 106

1. Introduction and general overview

The surface properties of a material can be tailored by depositing a thin film on it. Among different physical vapor deposition (PVD) techniques, sputter deposition is a well-established process at industrial scale due to its flexibility and scalability. In magnetron sputtering, an additional magnetic field enhances the plasma density which enables the sputtering process to work even at low working gas pressure [1, 2]. It is a widely used technique for high-quality functional coatings at both laboratory and industrial scale. Particularly, cylindrical magnetrons exhibit higher deposition rate, greater stability, low deposition temperatures, and better control of material composition.

During the sputtering process, the deposited material is ejected from the surface of a target (cathode) due to bombardment with the energetic particles. In magnetron sputtering, a magnetic field close to the target confines the motion of secondary electrons near the target surface. The resulting higher plasma density enhances the sputtering process at low inert gas pressure. However, the plasma is generally not uniform over the target surface, and regions of different plasma densities lead to a non-uniform target utilization. The surface morphology of the target affects the angular distribution and deposition rate of the sputtered atoms [3]. Therefore, the monitoring of the target surface during the sputtering process is of great importance.

Magnetron sputtering is not only confined to elemental pure single material deposition. During the sputtering process, an additional reactive gas can be used to form coatings of different chemical compositions. Once a reactive gas is introduced during the sputtering process, it not only interacts with the substrate as desired to form compounds, but also a compound layer on the target surface is formed. These compound layers poison the target surface and this target poisoning is one of the technological drawbacks of the reactive sputtering process. The additional compound layer on the target surface might change the surface morphology of the target. The poisoning of the target significantly decreases the sputter yield and also changes the chemical composition of the deposited coatings [4-6]. As the thickness of the compound layer varies under different sputtering parameters, the surface morphology of a target becomes important also for reactive sputtering.

Optical techniques have great potential for non-contact and on-line measurement of surface roughness [7]. When electromagnetic radiation is incident on a surface, the reflected beam bears useful information about the roughness of the surface. The proportion

of specular to diffuse reflection of incident radiation on a rough surface depends on the surface properties, including surface roughness. In a preliminary work, *Clark* [8] suggested the use of a laser beam for the application of real time, non-contact surface roughness measurement. *Persson* [9] has demonstrated the in-process measurement of surface roughness of a specimen on a grinding machine using laser scattering. The on-line roughness measurement method proposed by *Wang* [10] is also based on a laser-scattering probe. For roughness measurement, different authors have assumed the rough surface as a combination of mirror-like microfacets with different orientations. *Torrance* [11] considered these randomly placed facets as the basic mechanism for both specular and diffuse reflection from a rough surface. By considering the reflection from these facets, *Oren* [12] presented a comprehensive model to predict the reflection from a rough surface. Based on reflection, these models explain how surface orientations affect the intensity and the shape of the specular and diffuse patterns. They also account for the geometrical effects such as masking, shadowing and inter-reflection between different points.

On the other hand, for reactive sputtering, many efforts have been devoted to measure the thickness of the compound layer on the target surface. *Jonsson et al*. [13] estimated the oxide layer on Al by measuring different system parameters. Based on an extension of the basic Bergs models [14], it is assumed that the target surface consists of $n+1$ fractions and the ith fraction is covered by i monolayers of the compound. The thickness of the compound layer was related to the reactive gas pressure and voltage drop during transition from compound to metallic mode. Similarly, the thickness of an oxide layer on a Tantalum target surface was determined by the sputter cleaning method [15]. The discharge voltage behavior during the sputter removal of the oxide layer was attributed to the thickness of the oxide layer. The time for sputter erosion of compound layers is more pronounced for oxides due to the higher reactivity of oxygen, so such techniques are generally used for the measurement of oxide layer thickness. *Abe et al*.[16] reported an oxide layer of up to 100 nm of varying thickness on a Ti target surface (using a model target by depositing a 1 µm Ti film on a Si wafer) by changing the process parameters. The thickness of the oxide layer on the model target was measured by ellipsometry. In a recent study, using a similar model target (1 µm thick, sputter deposited, Al film on a Si wafer), the oxide layer thickness on the Al target was estimated to be 5–7 nm by ellipsometry at 100 % flow ratio of oxygen [17]. However, the thickness of a nitride layer on the Ti target surface is low (2.5 nm) [18] as compared to the oxide layers [16]. So, for nitride thickness

measurement, state of the art instruments (spectroscopic analysis) are required and generally measurements are done on a model target with rather small dimensions.

Using optical spectroscopic analysis of the discharge from the poisoned target, *Combadiere* and *Machet* [19] have predicted the degree of target erosion of Ti covered by a TiN film. A small sample target (10 mm in diameter and 2 mm in thickness) was analyzed by XPS. A different N/Ti ratio was observed on the poisoned target surface as a function of sputtering time. During reactive sputtering, the additional compound layer on the target surface modifies the height profile of the target surface. Therefore, if one can connect the target roughness with the degree of poisoning, it would provide a vast range of possibilities for real time information about the sputtering parameters. The aim of this thesis is to develop a model for in-situ assessment of the roughness of a uniformly eroded cylindrical magnetron target and to link the roughness evolution with target poisoning.

The reactive sputtering of Al and Ti in the presence of Nitrogen (N_2) is widely used to deposit AlN and TiN films, respectively. These nitride coatings have been extensively used in a variety of applications due to their excellent properties. AlN, a wide band gap ceramic exhibits high thermal conductivity [20] and is used in many applications due to its electroacoustic properties [21], excellent piezoelectricity [22] and optical properties [23]. On the other hand, TiN is a conductive ceramic with high thermal and chemical stability. It is extensively used for diffusion barrier [24], wear resistance [25], decorative coatings [26] and biocompatible implants [27].

The properties of these nitrides can be tailored by changing the sputtering conditions such as reactive gas partial pressure [28], Ar/N_2 ratio [29], substrate temperature [30], substrate bias voltage [31] and sputtering power [32]. The variation in flow rate of the reactive gases also gives a good control over stoichiometry of the deposited films. However, at a certain flow rate of the reactive gas, the target is poisoned by the compound formation on the target surface as mentioned before. Due to different electronic properties of the compounds, the discharge voltage is significantly changed (increased or decreased) in the poisoning mode. As a consequence, the sputter yield and the corresponding deposition rates are decreased [33]. Target poisoning is a complex mechanism and the reactive gas molecules are not only chemisorbed on the target surface but also get implanted into the target surface [34, 35]. After a certain poisoning time, the target surface may contain non-reacted target material, compound formed by chemisorption and chemically reacted compound. The target surface elements with different composition

exhibit different surface binding energies and the energy of the sputtered particles is influenced by their origin [36]. The increased content of the compound on the target surface influences the energy distribution function of the sputtered particles. Although particle fluxes and energy distribution of the sputtered atoms have been investigated in metallic and poisoning mode [37, 38], the effect of short and long-term poisoning on the sputter deposited films has not yet been addressed.

In this work, we present an experimental approach to monitor the surface roughness of an eroded cylindrical sputtering target by reflection of a laser beam. The surface of the eroded region is modeled as a random arrangement of microfacets. Our model is based on ray tracing optics as we assume that the size of facets is much larger than the incident wavelength. A laser beam hits the surface and the specular and diffuse reflection is captured on a screen. This technique for the surface analysis of the target is based on assessing the specular and diffuse patterns of the reflected laser beam from the tilted microfacets of a rough surface. In addition to the information of total radiance, which helps to investigate the relationship with the surface roughness, the generation of surface replica directly from the reflected pattern could be a new approach for in-situ surface analysis. Under certain conditions, the intensity and direction of the reflected beam can be attributed to the orientation and area of the facets. The surface profiles were generated directly from the reflected pattern of the laser beam. The different roughness parameters, root mean square (RMS) roughness, correlation length, skewness and kurtosis of the generated surface profiles were calculated for Al, Copper (Cu) and Ti sputtering targets. These roughness parameters were compared with those obtained from mechanical profilometer measurements and were found to be in good agreement.

As a proof of concept, we utilized this technique for the in-situ monitoring of target poisoning through roughness evolution during reactive sputtering. Although the discharge voltage is linked with the level of target poisoning it does not give much information about the target surface morphology which consequently alters the sputtering yield. Al and Ti targets were reactively sputtered and from their hysteresis curves, the critical flow rates of reactive gases were determined for partial and complete poisoning. After a certain sputtering time, a laser beam reflected form the target surface was again utilized for the surface roughness evaluation. The mean tilt angles of target surface facets were calculated from the reflected intensity profiles. A change in surface roughness was observed after reactive sputtering at different flow rates of reactive gases. With decreasing roughness, a

decrease in deposition rate was also observed. These lower deposition rates after prolonged sputtering in poisoning mode can be attributed to the degree of poisoning on the target surface. At different poisoning levels, the targets were sputter cleaned in the absence of reactive gases and de-poisoning time was also measured. A good correlation was observed among the roughness evolution, deposition rate and de-poisoning time.

Target poisoning not only affects the sputtering yields, it also alters the composition of the deposited layers [39, 40]. Therefore, finally, the effect of prolonged poisoning on the properties of the deposited films was investigated. Al and Ti targets were reactively sputtered with N_2 as reactive gas in the poisoning mode, so the target surfaces were covered with a nitride layer. After stabilization of the sputtering parameters (e.g. discharge voltage), the AlN and TiN films were deposited on a natively oxidized Si wafer during the first 10 min of sputtering in the poisoned mode and after 60 min of poisoning, respectively. The influence of short and long-term poisoning was investigated by measuring the surface morphology and structural properties of the films by Atomic Force Microscopy (AFM), Scanning Electron Microscopy (SEM), X-ray diffraction (XRD), and X-ray photoelectron spectroscopy (XPS). A change in microstructure, preferred crystallographic orientations and elemental composition of the deposited films prepared at different poisoning levels was observed. It was found that, the different levels of target poisoning could control the properties of the sputter deposited films.

It can be concluded that the in-situ method of laser reflectometry can be used to monitor the target poisoning through roughness evolution which can influence the sputtering parameters, like sputtering yield, the film structure and the chemical composition of the thin films. Additionally, by monitoring the target surface, periodically modulated structures on the target surface, variation of target poisoning across the target surface and dangerous events like target melting can presumably be observed.

The present thesis is structured as follows; in chapter 2, fundamental concepts of sputtering and the surface characterization of sputtering targets are discussed. Chapter 3 describes the experimental set up for the in-vacuo assessment of surface of the cylindrical magnetron target. In chapter 4, I will discuss a technique for in-situ assessment of target roughness during magnetron sputtering. Chapter 5 describes the estimation of target poisoning during reactive sputtering. In chapter 6, I will explain the effect of poisoning on the properties of the sputter deposited films. Finally, chapter 7 presents the conclusions and outlook.

2. Fundamentals

2.1 Sputtering

The surface of any material is the most important part determining its interaction with the environment. In many cases, although the bulk properties are excellent for a specific application, the surface may still require to be modified for a desired set of properties. The surface properties of a material can be changed by coating an additional thin film on it. The properties of the thin film depend on its composition, thickness and structure. Basically, there are two methods of film deposition from the gas phase, chemical and physical. The Chemical Vapor Deposition (CVD) method involves chemical reactions for the formation of thin films. In the presence of a precursor gas, the chemical reactions occur on the hot substrate surface, resulting in thin film deposition.

The process of depositing a material directly from the vapor phase is called Physical Vapor Deposition (PVD). In PVD, first the material is vaporized from a solid or liquid source, transported towards the substrate in vacuum and finally condenses on the substrate to form a thin film. PVD is a family of vacuum deposition processes working at comparatively low substrate temperatures. Typical examples are: evaporation, sputtering, ion plating and pulsed laser deposition. Among different PVD techniques, sputtering is one of the important coating techniques with many advantages like, variety of coating materials, large area coatings, easy tuning of coating parameters and environmental friendliness.

Figure 1 shows the schematic of a dc magnetron sputtering process. In an inert gas atmosphere (mostly Argon (Ar) at pressure 0.1 to 2.0 Pa), an electric discharge produces electrons, which on collision with Ar, generate Ar ions and finally a quasi-neutral plasma. When the positively charged ions hit the cathode/target material, neutral atoms, clusters, molecules or ions are ejected from the surface of the target. The ejected metal particles (m) condense on the substrate and eventually form a thin film on the substrate surface. In magnetron sputtering, a magnetic field close to the target confines the motion of secondary electrons near the target surface to enhance the ionization process which makes it possible to start sputtering at lower pressures, lower discharge voltage and higher ion currents.

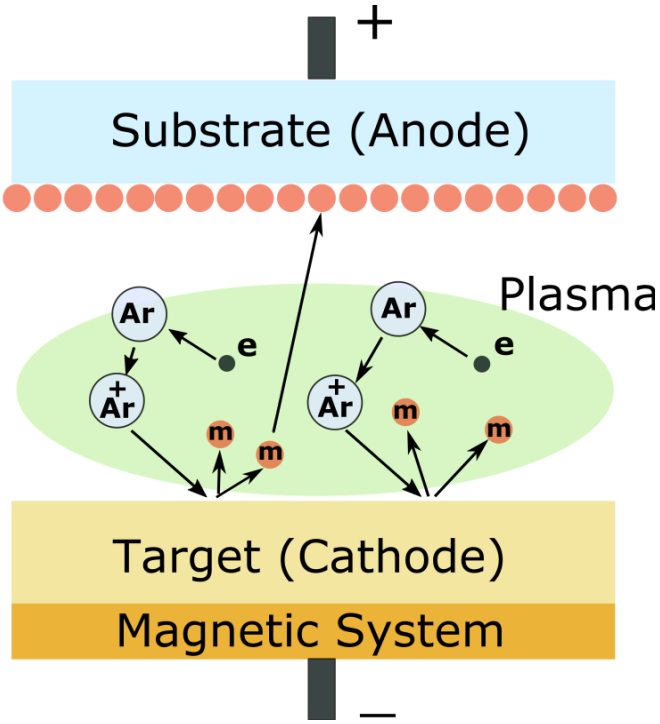

Figure 1: Schematics of a dc magnetron sputtering process.

Magnetron sputtering targets, either for a planar or for a cylindrical geometry, are shown in figure 2. In planar targets, the permanent magnets are statically located behind the target. With a static magnetic field, the regions of different plasma densities lead to a non-uniform utilization of the target surface. Due to higher erosion from a certain region of the target, a racetrack erosion profile appears on the target which results in low utilization of target material (40 %). Figure 2(a) shows the non-uniform utilization of a typical planar Al target. However, cylindrical targets have many advantages due to rotating magnets. They exhibit large material inventory and are suitable for large area coatings and higher sputtering power density. Generally, for cylindrical targets, the target utilization is up to 85 %. With a rotating magnetic field (rotating magnets or target), however, a certain part of the target may not be exposed to the plasma for a long time but, as a big advantage, the target surface is uniformly eroded as shown in figure 2(b).

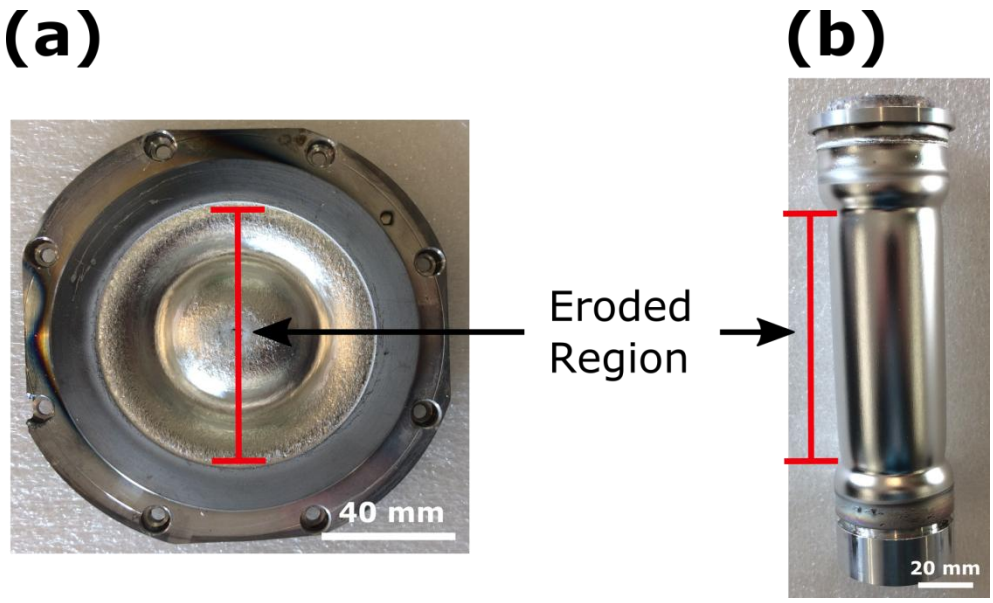

Figure 2: Eroded magnetron sputtering targets. (a) A non-uniformly eroded planar Al target with a static magnetic field. (b) A uniformly eroded cylindrical Al target with a rotating magnetic field

In sputtering, the fundamental mechanism of particle release involves the interaction between the impinging ions and the lattice atoms of the target. These interacting energetic ions can knock out atoms from the target surface. The ratio of the average number of emitted particles over the number of impinging ions is called sputter yield. The sputter yield depends on target material (surface binding energy of target atoms), mass, energy and impingement angle of the ions. The interaction between the ions and the target atoms can be distinguished into three regimes: single-knock-on, linear collision cascade and thermal spike regime.

- In the single-knock-on regime, low energy ions (10–100 eV energy) or light ions recoil after transferring their energy to target atoms and after a few one-to-one collisions, the ions eject target atoms from the surface.
- Ions with higher energy (0.1–10 keV), hit target atoms and generate a recoil cascade. This linear cascade ejects more atoms from the surface.
- In the thermal spike regime, for heavy ions with higher energies (>10 keV), the density of recoils is so high that a local high temperature is generated which increases the collision probability between atoms in a certain volume. Target material is partially evaporated.

The ion bombardment also releases secondary electrons from the target, which are responsible to sustain the discharge. The effective electron emission yield is basically a product of ion-induced secondary electron emission (ISEE) and the gas ionization

probability [41]. In magnetron sputtering, the discharge voltage is proportional to the ion-induced electron emission yield and with similar experimental conditions it is related to the sputter yield. Therefore, the current-voltage (I-V) characteristics becomes a valuable tool to study the sputtering behavior.

Figure 3 shows the I-V characteristics of the sputtering process for Al, Cu and Ti target materials at varying Ar pressures. Cylindrical targets (44 mm diameter and 100 mm erosion zone length) with rotating magnetic field were used for these measurements. At a fixed Ar pressure, the sputtering power was gradually increased from 500 W to 3.5 kW and the respective sputtering current and discharge voltage were measured. A rapid increase in current is observed with increasing voltage as expected from the well known empirical power law relation [1]:

$$I \propto V^n \tag{1}$$

$$\log(I) \propto n \log(V)$$

Where n is a constant whose value can vary from less than 1 to 10 depending on the working gas pressure, magnetic field and the target material [42].

While interacting with different species in the magnetron discharge, the secondary electrons also interact with the target surface and can be captured by the target [41]. The recapture probability depends upon the mean free path of the secondary electrons. The increase in Ar pressure affects the gas ionization probability due to the decrease in electron recapture probability. By interactions of electrons with the discharge gas, they lose their energy and they cannot reach the cathode. As a result, the coefficient of secondary electron emission increases and lowers the discharge voltage. Therefore, a decreasing trend in the discharge voltage is observed with increasing pressure of the Ar gas as figure 3 shows for Al, Cu and Ti targets for different Ar pressures. With similar sputtering conditions, the different values of discharge voltage relate to different sputtering yields. At 1000 eV Ar ion energy, Al, Cu and Ti exhibit sputter yields of 1.53, 2.82 and 0.73 (atoms/ion), respectively [43]. The different discharge voltage for Cu, Al and Ti as shown in figure 3(b) points to a higher sputtering yield of Cu as compared to that of Al in figure 3(a) and Ti in figure 3(c).

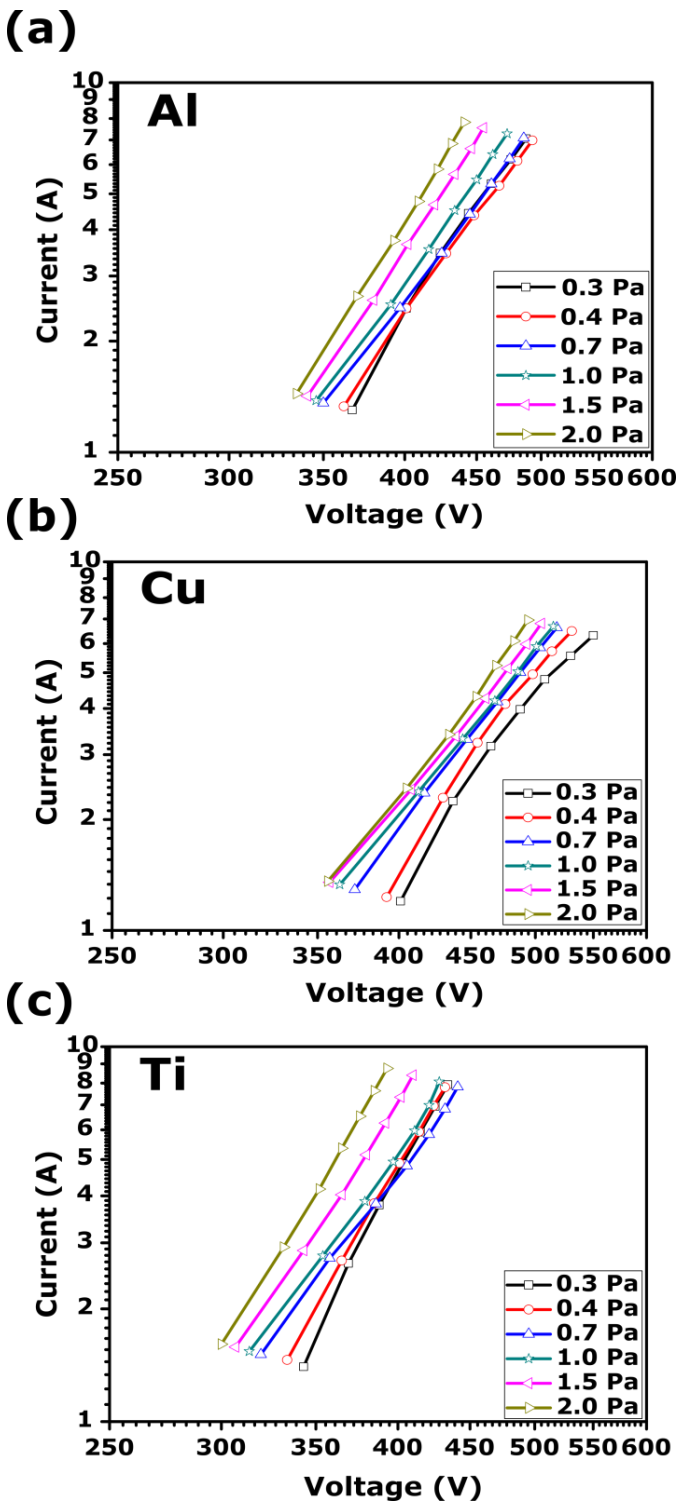

Figure 3: Current – Voltage characterization of the sputtering process assessed for virgin targets for different target materials at different Ar pressures. (a) The I-V characteristics of Al with slightly higher voltage showing medium level of sputtering yield. (b) Cu with very high discharge voltage shows higher sputtering yield at respective Ar pressures. (c) I-V characteristics of Ti shows low sputtering yield as compared to those of Al and Cu.

2.2 Reactive sputtering

Magnetron sputtering is not only confined to elemental pure single material deposition. During the sputtering process, an additional reactive gas can be used to form coatings of different chemical compositions. Generally, N_2, O_2, Carbon dioxide (CO_2), Acetylene (C_2H_2) and Methane (CH_4) are used as reactive gases. These reactive gases react with the sputtered material to form a coating of a compound on the substrate. The reactive gases are generally used to form oxides, nitrides, borides and carbides. Once a reactive gas is introduced during the sputtering process, it not only interacts with the substrate as desired to form compounds, but also forms a compound layer on the target modifying the target surface, which influences the sputtering parameters. This process is commonly termed as 'target poisoning' or 'poisoning'. The compound layer on the target significantly decreases the sputter yield and changes the chemical composition of the deposited coatings.

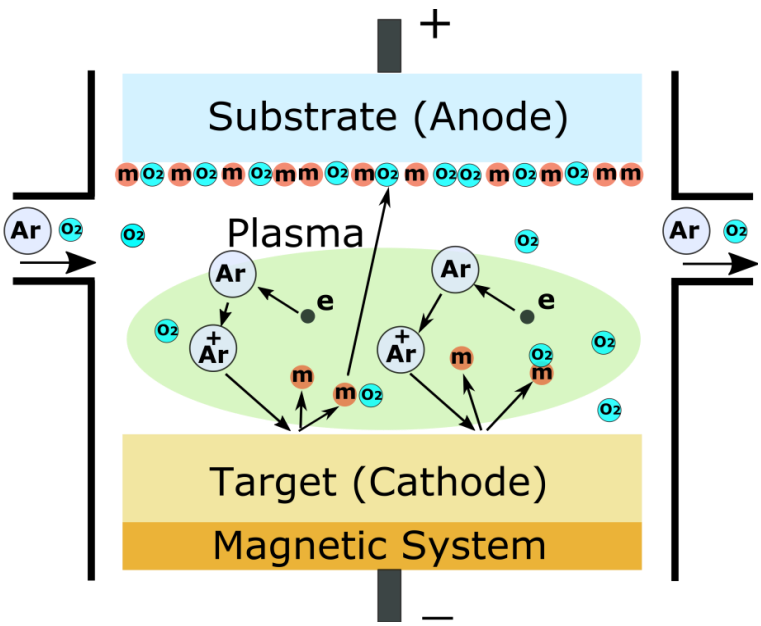

Figure 4: Schematics of a reactive dc magnetron sputtering process

Figure 4 shows the schematic diagram of a typical reactive sputtering process. In addition to Ar, which is the main gas to produce the plasma, an additional reactive gas (O_2 in figure 4) is used to react with the sputtered atoms to form a compound. By controlling the amount of the reactive gas, coatings of different chemical compositions can be obtained.

Theoretically, reactive sputtering can be described by Berg's model [14, 44]. This model allows to explain the experimentally observed hysteresis effect of process pressure, voltage or erosion rate by a simple mathematical treatment. Figure 5 shows the schematic of the particle flux during a reactive sputtering process. The incoming gas flow is the sum of Ar and reactive gas (*Rg*) flows, which are collectively represented by Q_{in}. A certain portion of the gas is consumed during the reactive process and the vacuum pump removes the rest (Q_p). During the sputtering process, the reactive gas reacts with the sputtered atoms and compound is formed at the substrate (including chamber walls) and the target surface.

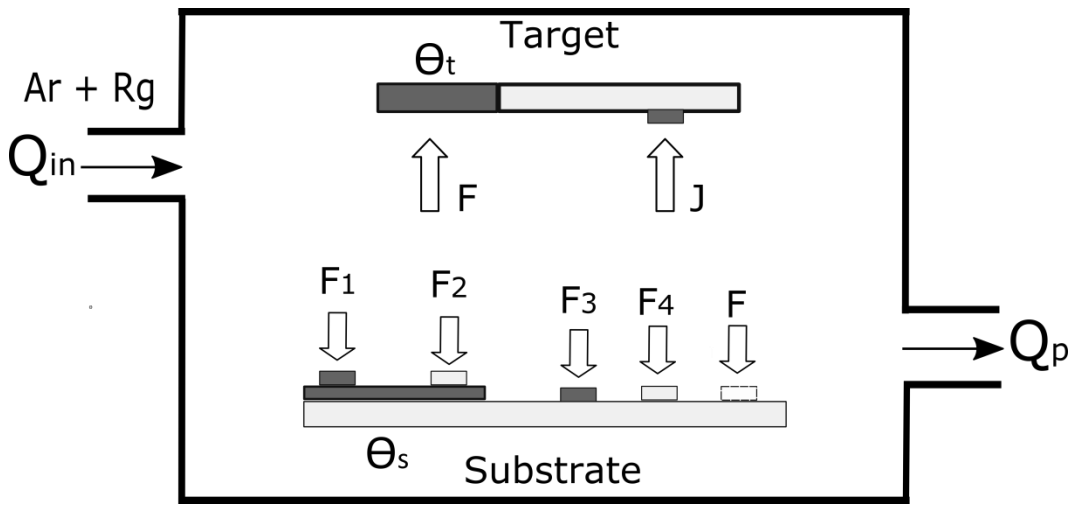

Figure 5: Schematic of particle fluxes to the substrate and target area during reactive sputtering. The dark grey portion represents the compound and light grey part represents the metallic segment of the target

Suppose a certain target area θ_t is covered by the compound layer. Similarly, the fraction (θ_s) of the substrate area is covered by the deposited compound layer. The fluxes of gas and ions are represented by *F* and *J*, respectively. Once a compound layer is formed on the target surface, both intrinsic and compound materials are supposed to be sputtered from the target surface. The sputtering from θ_t will generate a flux of compound materials (F_c), while from the rest of the target the flux consists of metal atoms (F_m). For simplicity, it is assumed that there is no time-dependent variation in sputtering parameters and sputtering is only due to Ar ions.

Form the above schematic illustration, the mathematical description of the different gas fluxes can be written as:

$$F_1 = F_c\theta_s$$

$$F_2 = F_m\theta_s$$

$$F_3 = F_c(1-\theta_s) \tag{2}$$

$$F_4 = F_m(1-\theta_s)$$

F_1 represents the flux of sputtered compound from the target on to the compound coated portion of the substrate. The metallic part of the sputtered target, deposited on the compound portion of the substrate is represented by F_2. Some fraction of the substrate is still free from the compound coating and F_3 denotes the flux of compound element from the target towards the metallic part of the substrate. The metallic part of the sputtered material on the metallic part of the substrate is symbolized by F_4. As the reactive gas molecules move randomly in the process chamber, the entire surface may be exposed to these gas molecules. The flux of the reactive gas molecules hitting the substrate is represented by F.

The input gas flux, Q_{in}, during the reactive sputtering process can be separated into three parts Q_t, Q_s and Q_p. They represent the consumption of gas molecules at the target, gas flow towards the substrate and throughput of the vacuum pump, respectively.

At steady state conditions the mathematical expression for reactive gas consumptions can be written as [45]:

$$Q_t = \alpha F(1-\theta_s)A_t$$

$$Q_s = \alpha F(1-\theta_s)A_s \tag{3}$$

$$Q_p = SP$$

Where α, A_t, A_s, S and P represent the sticking coefficient for target and substrate, area of the target, area of the substrate, pumping speed of the vacuum pump and partial pressure of the reactive gas, respectively. For simplicity, the same value of α is assumed for both target and substrate. In addition to the reactivity of different target materials, the partial pressure P becomes a significant parameter in the reactive sputtering process. Assuming that each compound element is composed of one metal atom and one reactive gas atom, the total number of metal atoms sputtered from the target surface, R_m, can be written as [45]

$$R_m = \frac{J}{q}\left[Y_m\left(1-\theta_t\right)+Y_c\theta_t\right]A_t \tag{4}$$

Where q, Y_m and Y_c represent the charge of electron, sputter yield of metal atoms and sputter yield of compound, respectively. A typical result from the solution of equation (4) is shown in figure 6.

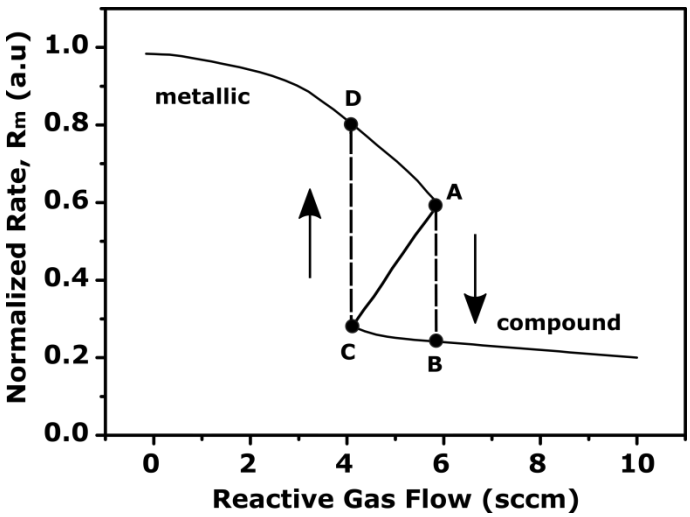

Figure 6: Schematic curve for the sputtering rate at different flow rates of reactive gas.

Considering these sputtered atoms to be uniformly distributed over the substrate (A_s), the deposition rate D can be written as

$$D = R_m\left[C_1\left(1-\theta_s\right)+C_2\theta_s\right] \tag{5}$$

Where R_m represents the total number of metal particles sputtered from the target surface and C_1 and C_2 are material specific constants. The S-shaped curve in figure 6 shows the theoretically predicted sputter rate in dependence on the partial pressure of the reactive gas [40]. The portion of the curve AC represents an unstable region and practically the sputter rate follows the dashed lines from A to B during increasing and from C to D during decreasing flow rate of reactive gas. The processing region between points D and A is called metallic region. In this region, the deposition rate is rather high and the composition of the deposited films is sub- stoichiometric. Between points C and B, in the compound region, the deposition rate decreases and the film composition is stoichiometric. The width of curve between dotted lines (AB and CD) represents the hysteresis width. The practical optimum operation point lies within the hysteresis region with possible high deposition rate

and a stoichiometric composition. However, a small increase in reactive gas flow rate will cause a remarkable decrease in deposition rate. Therefore, by controlling the partial pressure of the reactive gas, it is possible to operate at the optimum point.

From the above considerations, it follows that reactive sputtering is not a linear process and at different flow rates of reactive gases it exhibits hysteresis effects. To understand the reactive sputtering process, figure 7 shows a typical hysteresis curve for pressure and discharge voltage at different flow rate of N_2 for an Al target. The pressure and discharge voltage do not show the same behavior during increasing and decreasing flow rate of reactive gas. Initially, all the reactive gas is consumed by reacting with the metal particles to form a compound. There is not any significant increase in the chamber pressure and the target operates in metallic mode as shown in figure 7(a). The increase in the reactive gas flow not only increases the compound formation on the substrate, it also increases the area of the compound layer on the target. With decreasing erosion rate due to compound formation, the reactive gas molecules find less metal atoms to react and eventually there is a change in pressure as shown in figure 7(a). The further increase results in a dramatic increase in the chamber pressure and a corresponding decrease in discharge voltage at 8 sccm of the N_2 flow as shown in figure 7(b). As a result, the target is shifted to the poisoned mode. Different parameters influence the hysteresis effect, like target material, type of reactive gas, pumping speed, target to substrate distance, ion current and size of the target [33]. The target materials with higher sputter yield as compared to that of the corresponding compound exhibit a more pronounced hysteresis effect. Reactive gases with higher sticking coefficient are more reactive to the target material, and show higher hysteresis width [46]. The partial pressure of the reactive gas in the sputtering chamber is a key parameter for the hysteresis effect. So, this effect can be minimized by increasing the pumping speed [47]. A smaller distance between the target and substrate also decreases the hysteresis width due to different spread of the sputtered material. For cylindrical magnetrons with rotating magnetic field, the hysteresis width is also influenced by the rotational speed. At higher rotational speed, the compound layer poisons the target surface at a comparatively low flow rate of the reactive gas, because for fast rotating magnetic field there is less time to sputter clean the compound layer from the target surface [48].

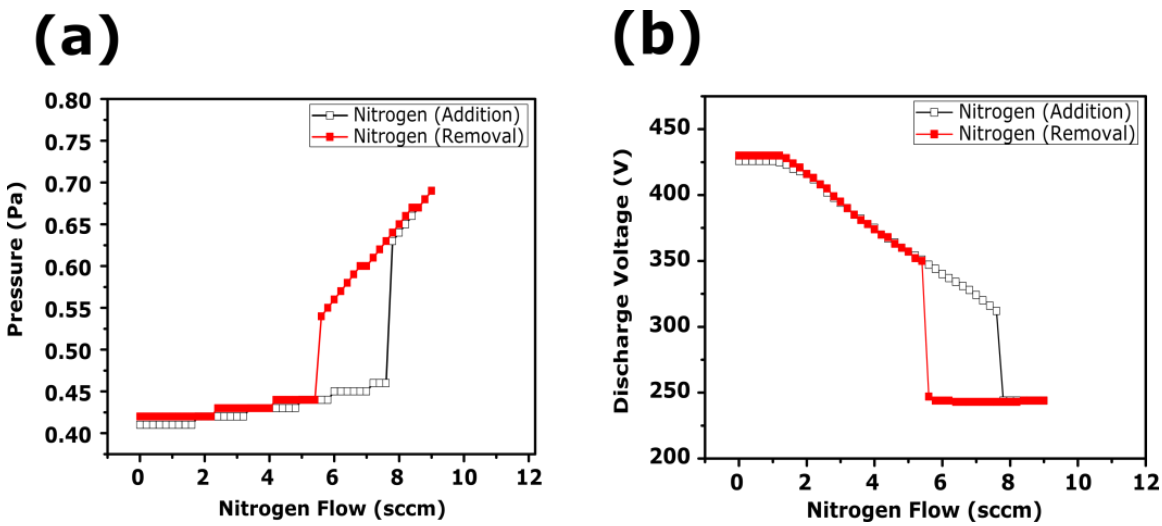

Figure 7: Typical hysteresis curves for an Al target during reactive sputtering at 5 A sputtering current. (a) Hysteresis curve for reactive gas pressure vs. flow rate of N_2 gas for an Al target. (b) Hysteresis curve for discharge voltage vs. flow rate of N_2 gas for an Al target.

Higher sputter current increases the erosion rate, and reactive gas finds more metal atoms for reaction. Therefore, the higher reactive current magnifies the hysteresis curve and the width of the hysteresis increases with increasing sputtering currents. Figure 8 shows the hysteresis curves for an Al target during reactive sputtering at different sputtering currents ranging from 5–7 A. In the case of reactive gas pressure, the hysteresis width also gradually increases with increasing sputtering current. The flux of sputtered atoms is greatly influenced by the effective target area. Generally, a small target area reduces the hysteresis effect unless the overall sputtering power is not very high.

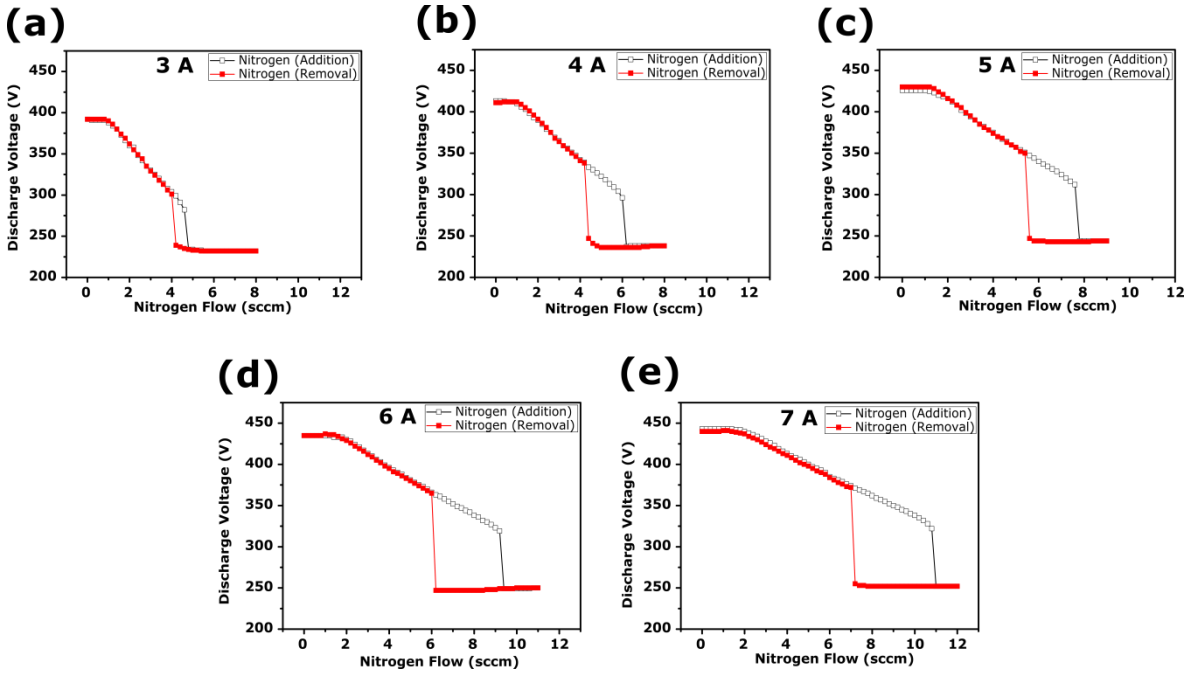

Figure 8: Hysteresis curves for an Al target during reactive sputtering with N_2 at different sputtering currents, (a) 3 A, (b) 4 A, (c) 5 A, (d) 6 A and (e) 7 A sputtering current

The secondary electron emission from the target surface is a key parameter in understanding the reactive sputtering process. The formation of the compound layer on the target surface significantly changes the secondary electron emission yield from the target. The compound formation influences the sputtering process in two ways: chemisorption of the reactive gas on the target surface and implantation of reactive gas ions into the target surface [34, 35, 49]. Chemisorption is described as the chemical reaction between the sputtered target material and reactive gas molecules. This reaction occurs in the whole sputtering chamber including the substrate and the target surface. Implanted ions, however, either react chemically with the target material to form a compound or remain adsorbed without chemical reaction or can diffuse within the target after combining with other ions. Therefore, the variation of target voltage during reactive sputtering is attributed to chemisorption and ion implantation. By considering the hysteresis curves, the suitable operating points can be marked for reactive sputtering in both metallic and poisoned modes with required stoichiometric composition and higher sputter yields.

2.3 Surface characterization

As the surface morphology of the target has a strong influence on the deposition flux, the assessment of target roughness can be useful in many aspects of magnetron sputtering.

Roughness measurement techniques are either contact type or non-contact type. Conventionally, for contact type, stylus instruments are used for easy roughness measurement. The stylus tip moves over the surface with constant velocity, converts the vertical motion of the tip to an electrical signal and records the surface profile. In spite of their accuracy, the direct contact techniques have many disadvantages like exerting mechanical loads, which can lead to scratches on the surface, long measuring time, wear of the tip and being not applicable for in-situ measurements. Non-contact methods however, have many advantages due to their non-abrasive nature. As the sputtering process works under vacuum conditions with inert gas at low pressure of about 0.4 Pa and at high voltage, the physical contact with the target is at least cumbersome. During the last few decades, different optical techniques have been developed for non-contact surface roughness measurement; optical profilers [50], confocal microscopy [51], optical sectioning [52], focus detection [53], Fourier transformation [54], angular distribution of light scattering [55] and speckle methods [56]. In previous works, the scattering of light from a rough surface is also extensively used for roughness measurement [57-60].

As the surface profile of the sputtering target influences the sputtering yields [4-6], by observing the surface roughness, the state of the target can be monitored and the target condition can be determined. Due to different surface structures, different materials after sputtering exhibit different surface profiles. The angular distribution of ejected atoms from a target is influenced by the orientation of the surface facets and the sputtering yield decreases with increasing roughness due to the re-deposition of the sputtered atoms or molecules [3]. In this work, the target surfaces were examined after a fixed sputtering time up to 4 hours at a constant sputtering current of 5 A. Figure 9 shows the optical images of a Cu target after different durations of sputtering. A significant change in target roughness was observed up to a certain sputtering time.

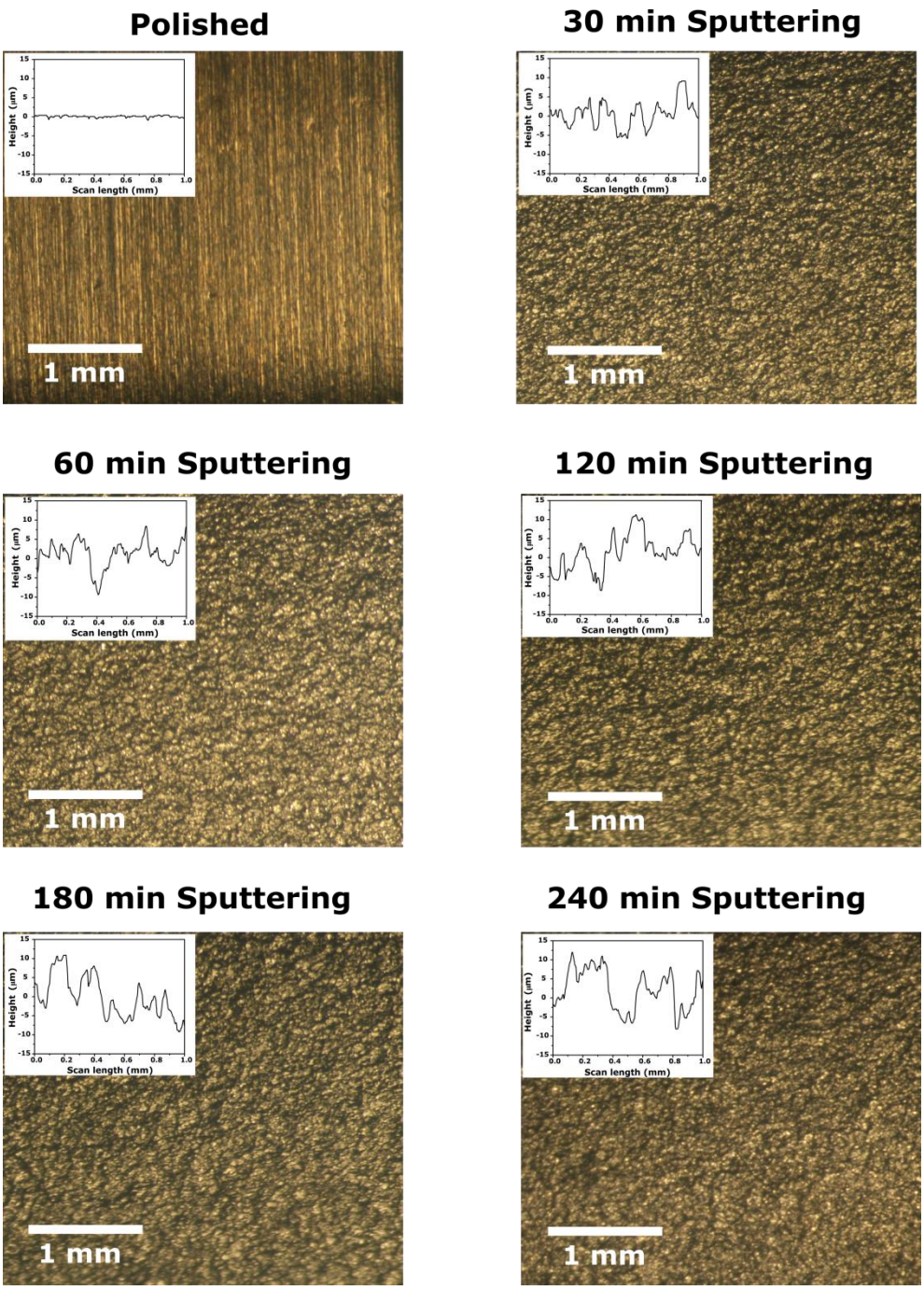

Figure 9: Optical images of Cu target, the polished surface of the Cu target was sputtered up to four hrs at constant sputtering current of 5 A. The optical images show the target surface after particular sputtering times. The inset figures show the roughness profile measured by a profilometer after each sputtering time.

Generally, the surface features of the eroded targets are much larger than the laser wavelength, so using geometrical optics, the laser reflection pattern of the eroded surface could be a suitable choice for target surface monitoring. When a laser beam incidents on a

rough surface, the reflected pattern bears the information of the surface morphology. The details of the surface roughness may be derived by further processing of both the specular and the diffuse part of the reflected beam. For rough surfaces, the purely specular part of the reflection disappears, and the diffuse part of the intensity directly relates to the surface morphology.

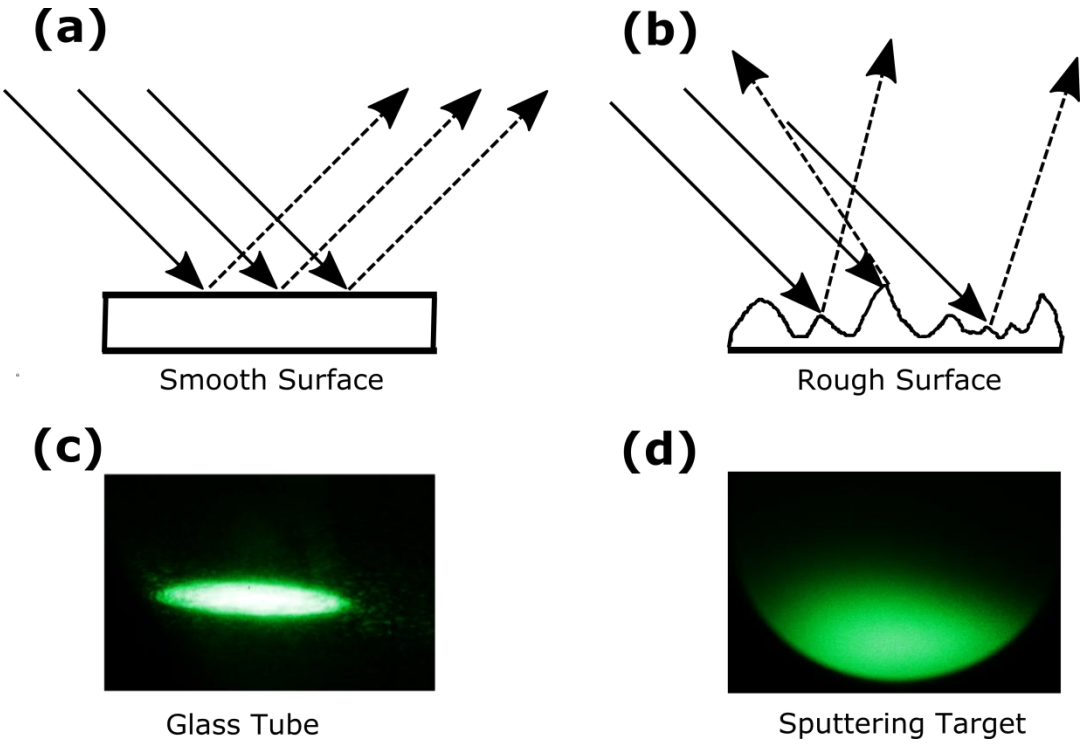

Figure 10: The typical reflection of light from a smooth and rough surface (a) Specular reflection of light from a smooth surface. (b) Diffuse reflection of light from a rough surface. (c) Reflection of a laser beam from a glass tube coated with Cu. (d) Reflection of a laser beam from an eroded Cu target surface.

Figure 10 shows the typical reflection of light from a smooth and a rough surface. For a smooth surface, the reflected light travels in the same direction and reflection is specular as shown in figure 10(a). If the reflecting surface is not smooth, if reflects the rays in different directions resulting in a diffuse reflection as shown in figure 10(b). Figure 10(c) shows the reflection of a laser beam from a glass tube sputter coated with Cu. The specular part of the reflected beam is prominent due to the mirror-like smooth surface. The same laser beam was also incident on an eroded Cu target surface with higher surface roughness. The reflected image with diffuse reflection is shown in figure 10(d).

We assume the surface of sputtering targets to be composed of several V-shaped tilted plane facets as shown in figure 11. The incident wavelength is considerably smaller than the lateral extension of the facet (*dA*).

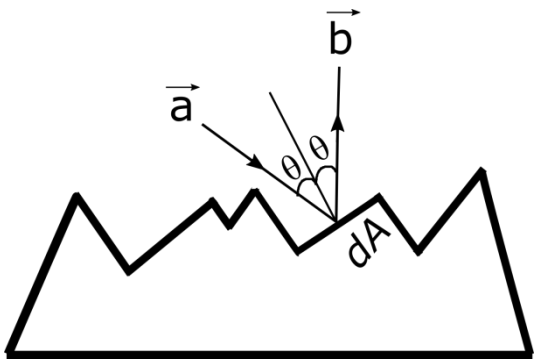

Figure 11: Model surface of a sputtered target

For a parallel laser beam with constant cross sectional intensity the reflected light can be considered as the reflection of partial beams from these facts. If the incidence direction $\vec{a}$ of the beam is constant, the intensity of reflected beams $\vec{b}$ becomes proportional to the area of each facet. The inclination of theses facets will change the lateral position of reflected beams. Experimentally the reflected images of a laser beam were captured on a screen. From the reflected intensity profiles, the intensity values were plotted as a function of distance from the centre point of the incident beam. The lateral distribution of the intensity corresponds to the tilt angle of the surface facets. The mean slope of these facets is associated to the roughness of the exposed target surface. In the following sections, the intensity profiles of reflected laser beams from different target materials are evaluated. By determining the intensity at each pixel level, the surface roughness parameters are determined and finally, based on these roughness parameters the degree of target poisoning is evaluated.

3. Experimental setup

The experimental setup is shown in figure 12. The sputter deposition plant consists of a cubic stainless steel chamber (volume approximately 11 liters), evacuated to a base pressure of 10^{-4} Pa by a turbomolecular pump (Adixen ATP-150) backed by a rotary pump. A manual valve was located between the vacuum chamber and the pumping system to regulate the pumping speed. A cylindrical target/cathode of 44 mm diameter and 100 mm length, cooled by running water was fixed inside the chamber. A magnet assembly rotating at a speed of 13 revolutions per minute was positioned inside the cathode tube. The magnetic system consists of six parallel bars of magnets, which create six plasma pipes parallel to the target axis. During rotation, each surface element was periodically exposed to a plasma pipe after every 0.769 s. High purity (99.999 %) Argon (Ar) was used as working gas while N_2 and O_2 were used as reactive gases. A capacitance gauge (MKS Instruments, Type 627B, 1 Torr), which is a gas independent pressure gauge was used to measure the total gas pressure during the sputtering process. The flow rates of working and reactive gases were separately attuned by mass flow controllers (MKS, Mass-Flo, 50 standard cm^3/min (sccm)). A laser source (Laser Fuchs, LFD532, Class-3R) with 532 nm wavelength and 3 mm beam diameter was used. This laser beam was incident on the target surface through a quartz window. A circular screen (PET film, Kimto 100-PBU) of 100 mm diameter, as shown in figure 12(b), was fixed inside the chamber. The reflected laser beam was then projected onto the screen. A rotatable cylindrical shutter was developed to protect the screen from exposure to sputtered material as shown in figure 12(c). A small hole in the shutter of 1 cm diameter was used as entry port of the laser beam to the sputtering target. Another circular hole of 10 cm in the shutter was used to expose the screen to the laser beam reflected from the target surface. During sputtering, the screen was protected from exposure to sputtered material by the shutter. A transparent window of poly methyl methacrylate (PMMA) was fixed to see the laser scattered image on the screen from outside the vacuum chamber. A digital camera (Canon EOS, 1200D) was also fixed outside the vacuum chamber to capture the images of the screen through this window as shown in figure 12(d). The path between the PMMA window and the camera was covered with a black sheet to avoid the exposure of the screen to external light. With this setup, we were able to photograph the images of the reflected beam from an eroded target surface under high vacuum conditions.

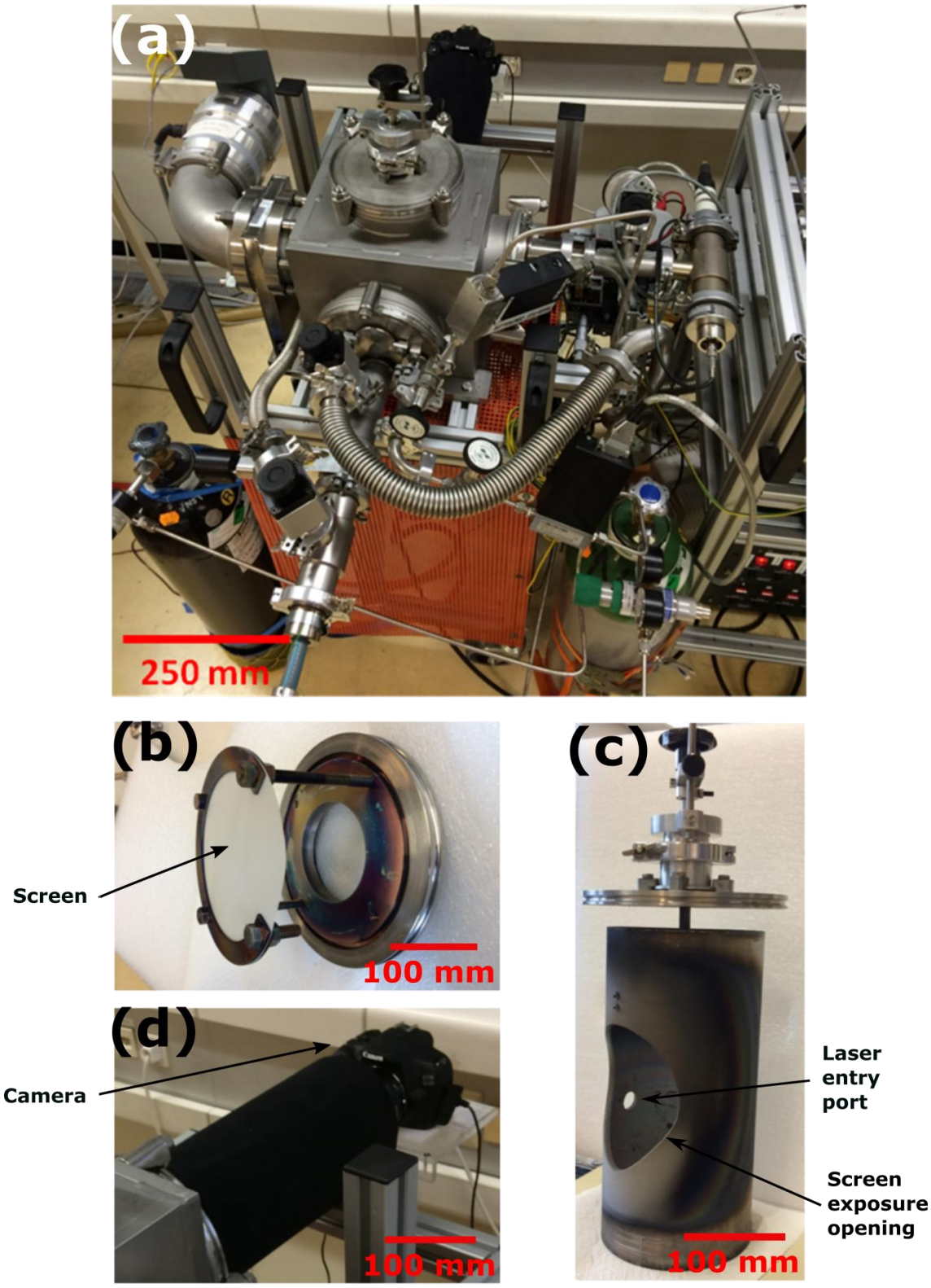

Figure 12: Experimental setup of sputtering system. (a) Complete system with the accessories. (b) Circular screen for imaging of the reflected light. (c) Rotatable cylindrical shutter to protect the screen from the sputtered material. (d) Digital camera to capture the photo of the screen.

3.1 Roughness measurement

Figure 13 shows a schematic diagram depicting our experimental setup for recording the reflected images of different target materials. With reference to the cylindrical target, the screen and laser beam were placed in such a way that the reflected image of the laser from the target surface can be captured on the screen. Ideally, if the beam is considered to have negligible diameter, the laser was reflected on the cylindrical surface under an angle of 90° (Fig. 13). The distance between the screen and the target surface was set as 75 mm. First of all the sputtering chamber was evacuated to a pressure of 10^{-4} Pa using a high vacuum pumping system. Argon (Ar) was used as working gas during magnetron sputtering. The Ar gas was inserted into the chamber at a flow rate of 8 sccm. By adjusting the manual valve between sputtering chamber and the pumping system, the Ar pressure was set at 0.4 Pa in the sputtering chamber. Al, Cu and Ti targets were separately used for the investigation of roughness. Each target was sputtered at a constant 5 A dc discharge current for different durations up to 4 hrs. For each sputtering interval, the laser beam hit the eroded target surface and the reflected images were captured on the screen. During the sputtering process, the cylindrical shutter was rotated in such a position that the screen and the laser entry port were not exposed to the sputtered material. After the sputtering cycle, the cylindrical shutter was again rotated to get the reflected beam on the screen. Using this arrangement the screen was completely safe from the sputtered material as was shown by checking for deposits on the screen after several hours of cathode operation.

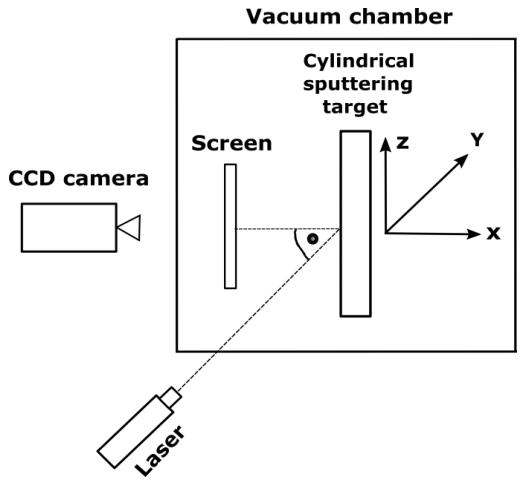

Figure 13: Schematic diagram depicting the experimental setup to capture the specular and diffuse reflection pattern of a laser beam reflected from the eroded cylindrical sputtering target on the screen. Arrangement of cylindrical sputtering target, screen, laser and camera to photograph the reflected image from outside the chamber under vacuum conditions.

Before each sputtering cycle, the targets were removed from the vacuum chamber and the eroded surface was polished to get the same initial target surface roughness. The erosion rate of the target was considered as constant over the entire cylindrical surface due to the rotation of the magnetic system. Digital images of reflected light from these targets were photographed using the digital camera, after each sputtering run.

The digital camera (Canon EOS, 1200D) is equipped with an 18-Mpix CMOS sensor with ISO sensitivity option equivalent of ISO12800. With an active-pixel sensor (APS), where each pixel contains a photo detector and an active amplifier, it provides a linear response of the light to the generated current. The images were taken at lower ISO values (200) for less noise. Additionally, before recording the reflected images, the optical settings were adjusted to avoid the intensity saturation of the reflected images. For this purpose, glass tubes with a diameter similar to the sputter target were sputter coated with Ti, Al and Cu, separately. Figure 14 shows the optical images of glass tubes sputter coated with Ti, Al and Cu. These glass tubes were fixed in place of the metallic target and reflected images were captured on the screen. The camera settings were adjusted in such a way that maximum measured intensity in the reflected images must be lower than the saturation limit of 255 (Shutter speed: 1/250 sec, Aperture Value: 5.0 and ISO speed: 200). These camera settings were used throughout the experiment for all target materials.

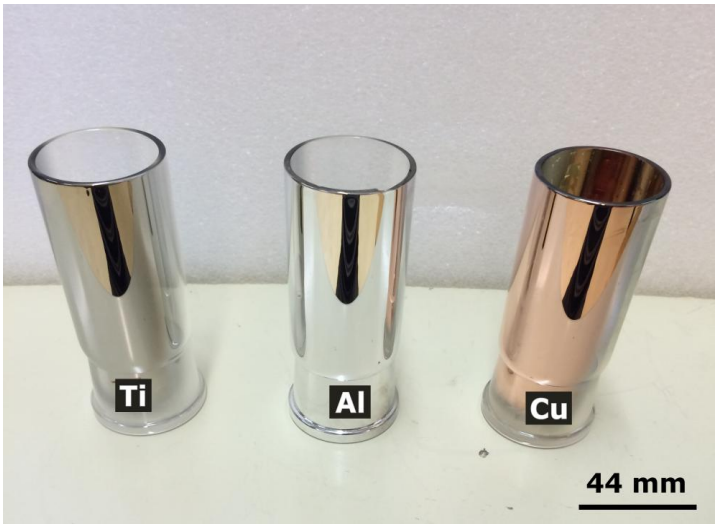

Figure 14: Optical images of glass tubes sputter coated with Ti, Al and Cu.

The images of the target surface were analyzed by using the MATLAB (R2013a) computer software. The reflected intensity distribution was utilized for the target surface analysis. Using a custom written algorithm (for details, see section 4.2), the roughness

profiles were reconstructed from the reflected patterns of the laser. The roughness variables, RMS roughness, skewness, kurtosis and correlation length were calculated for the constructed/generated roughness profiles. The same roughness parameters were also measured by a mechanical profilometer after each sputtering cycle by removing the target from the sputtering chamber.

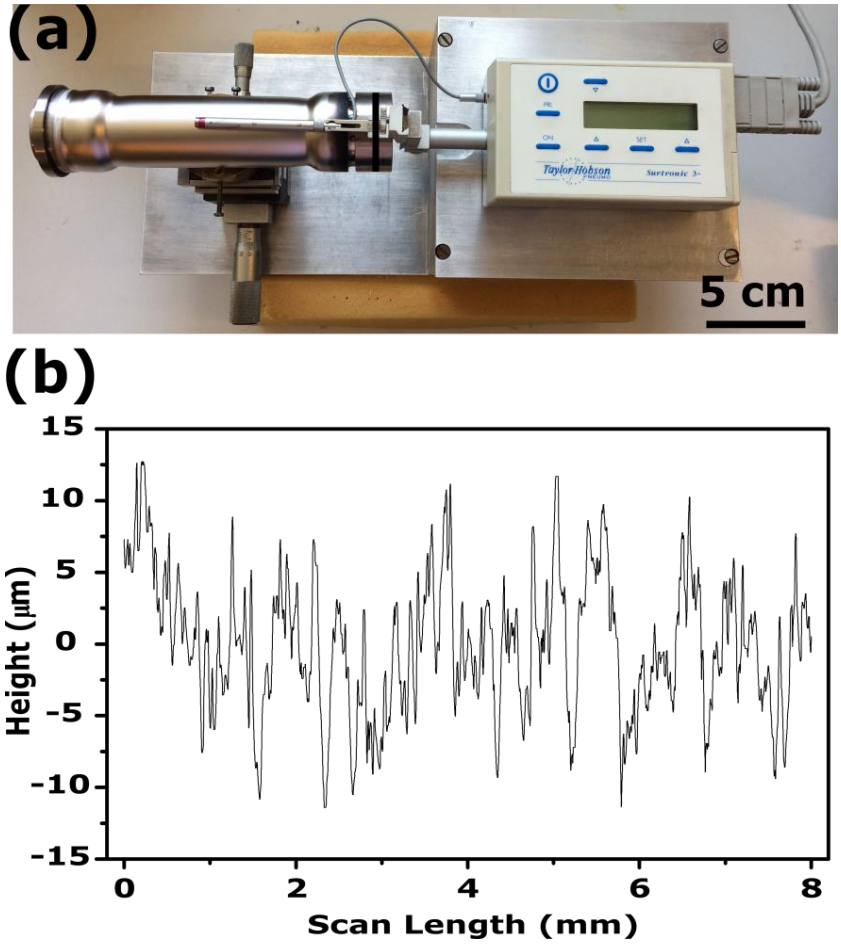

Figure 15: Experimental set up for roughness measurement by a profilometer. (a) Placement of a target for roughness measurement. (b) A typical height profile measured by the profilometer.

A mechanical profilometer (Taylor-Hobson, Surtronic3+) was used to measure the roughness of the target surface as shown in figure 15. In this mechanical profilometer, a sapphire tip physically moves along the surface following its morphology. A transducer converts the tip movements into a proportional electrical signal and finally the surface profiles are produced. The target surface was scanned along the cylindrical axis of the target as shown in figure 15(a). Figure 15(b) shows the typical height profile of a Cu target examined for a scan length of 8 mm. The results obtained from the in-situ technique were

in good agreement with those measured outside the sputtering system. Moreover, the experimental in-situ arrangement allows us to monitor the eroded surface under high vacuum conditions without removing the target from the sputtering chamber. Nonetheless, it has to be noted that the discharge has to be switched off to allow the assessment of the reflection without disturbance of light emitted from the plasma.

3.2 Assessment of poisoning

For the assessment of the target poisoning, sputtering was again started at constant current (5 A) mode and a constant Ar pressure was set at 0.4 Pa in the sputtering chamber. Then, in addition to this constant Ar flow, the flow of reactive gas was introduced. Al and Ti targets were sputtered in reactive modes in the presence of O_2 and N_2 to form oxides and nitrides, respectively. During this reactive sputtering process, the reactive gases not only interact with the substrate as desired to form compounds, but also poison the target surface with a compound layer. At a certain flow rate of the reactive gas, the sputtering parameters are substantially changed. For determination of the critical flow rate of reactive gas the flow of reactive gas was stepwise increased and process parameters like total pressure and discharge voltage were recorded. The flow rates of the reactive gases were optimized for complete target poisoning due to the compound formation on the target surface by recording the respective discharge voltage. The critical flow rates of reactive gases were determined for the transition of the target surface from metallic to the poisoned state.

Each target was first sputter cleaned for 10 minutes at a constant current (5 A) and constant Ar pressure of 0.4 Pa without reactive gas flow. Sputtering power was then switched off and the images of the reflected beam were captured on the screen. To measure the effect of poisoning on the target surface, the sputtering was again started at the same constant current and Ar pressure. The target was non-reactively sputtered until the process parameters were in steady state. Then the reactive gas was introduced at different constant flow rates: 7 sccm transition region metallic mode, 7 sccm transition region poisoned mode, 9 sccm for complete poisoned mode for N_2 and 16 sccm for complete poisoned mode for O_2, as indicated in the hysteresis curves in figure 30 by the points b, c and d, respectively. After 5 minutes of reactive sputtering, the sputtering power was again switched off. The reflected image of the laser beam from the poisoned target surface was again captured on the screen.

Figure 16 shows optical images of the targets in metallic and poisoned states. Figure

16(a) shows the optical image of an Al target after sputtering both in metallic and poisoned state. In poisoned conditions the target surface looks smooth and shiny. Similarly, for Ti, as shown in figure 16(b), an apparent decrease in surface roughness indicated by the shiny appearance can be observed between metallic and poisoned mode. For surface evaluation of the targets, the same procedure was repeated: non-reactive sputtering until steady state, and then continuous reactive sputtering with increasing time up to 60 minutes. For each time interval, the reflected images were recorded for both metallic and poisoned modes of the targets. Form these reflected images, the intensity values were scanned to the length of 1500 pixels from the origin (corresponds to 30 mm on the screen, see figure 32 (a)). It was assumed that the facets only tilted along the tangential plane of the cylinder mainly influence the intensity profile in the vertical direction. The mean tilt angles were calculated from these intensity profiles for both Al and Ti target surfaces with different reactive sputtering time using equation (5). The mean tilt angle values correspond to the target roughness. A roughness evolution was observed after different poisoning levels of the target surface. The target surface roughness was also measured by a mechanical profilometer after poisoning with oxides and nitrides. Again, this change in roughness of target surface was found in good agreement with ex-situ measurement taken from a mechanical profilometer.

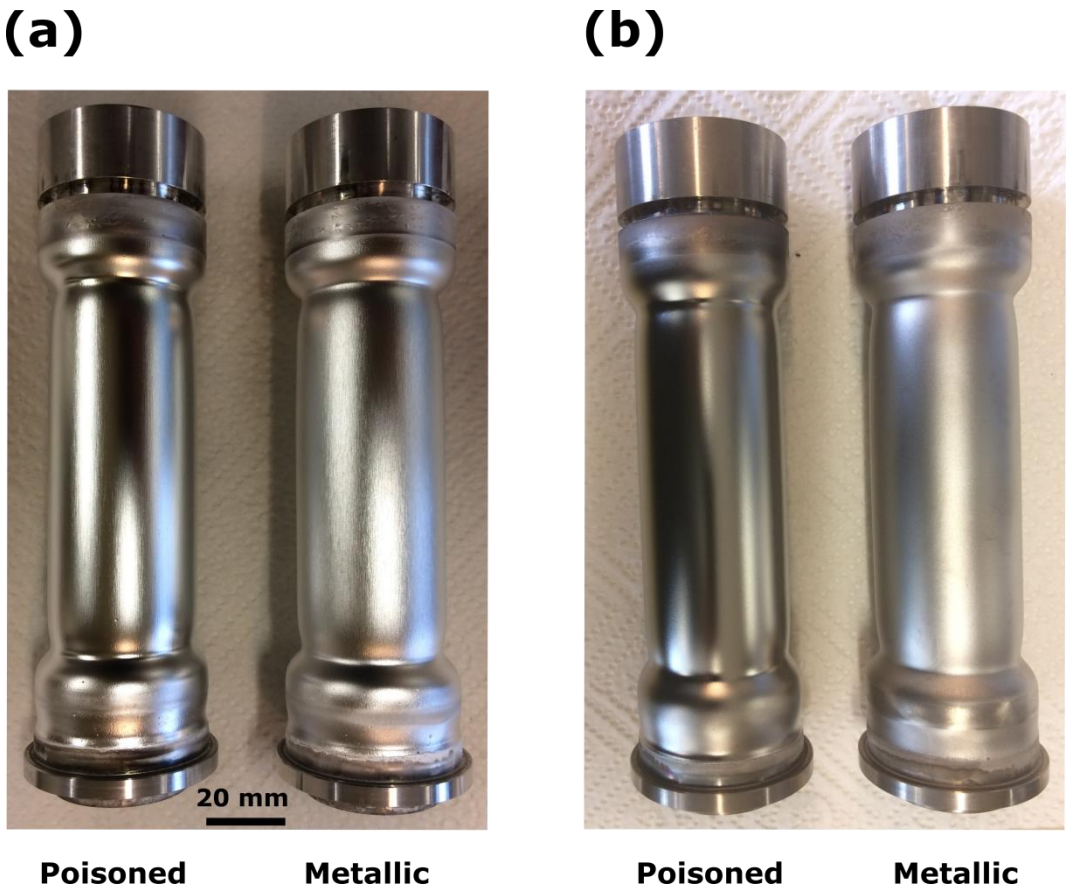

Figure 16: Optical image of the targets in poisoned and metallic state. (a) Optical images of Al target after sputtering in metallic and poisoned mode. (b) Optical images of Ti target after sputtering in metallic and poisoned mode.

To study the influence of long-term poisoning, after different poisoning times, the sputtered material was deposited on natively oxidized Si wafers for a fixed sputtering time. Before each deposition cycle, the target was sputter cleaned in non-reactive mode for 10 min. At this point, the target was considered in a purely metallic condition. Then, the reactive gas was introduced at the specified flow rates. After stabilization of the discharge voltage, the substrate was exposed using the rotatable shutter for 10 min, then the shutter was closed and the substrate was removed via a load lock. The reactive gas flow was switched off and the target was cleaned in non-reactive mode. Again, the reactive gas was introduced and reactive sputtering was performed for 60 minutes. After one hour of reactive sputtering, a film was deposited on another substrate for 10 min. Similarly, two samples (after 10 and 60 minutes of poisoning) with the same deposition time of 10 minutes were manufactured for each flow rate corresponding to points *b*, *c* and *d* of reactive gas as shown in figure 30. The film thickness was measured after two different

sputtering times, in transition region metallic (point *b*), transition region poisoned (point *c*) and complete poisoned mode (point *d*). The step heights of the films deposited on a Si substrate partially covered by holding clamps (Fig. 17(b)) were measured by a mechanical profilometer. For each case, from these measured height values, the deposition rate in nm per minute are determined.

Finally, for the assessment of the compound layer, the poisoned targets were sputter cleaned in the absence of reactive gas. After a certain period of reactive sputtering, the sputtering current was switched off and the flow of reactive gas was stopped. After removal of the reactive gas, the magnetron discharge was started at 0.5 A constant sputtering current at an Ar pressure of 0.40 Pa. A sudden change in discharge voltage is observed when the target is subsequently shifted to the metallic mode. This transition from poisoned to metallic mode was monitored by the rate of change of the discharge voltage. The discharge voltage was recorded until it became constant in the metallic mode.

3.3 Characterization of deposited films

To study the influence of long-term poisoning on the composition of the deposited films, Al and Ti targets were reactively sputtered in the presence of N_2 at 5 A constant sputtering current. The experimental setup for the preparation of nitride films is shown in figure 17. Initially, the flow rate of reactive gas was increased to 9 sccm for a quick transit to the poisoning mode. After shifting to the poisoning mode, the flow rate of reactive gas was reduced to 7 sccm. Once the target is fully poisoned, it remains in the poisoning mode even at a comparatively lower flow rate of the reactive gas, as shown by the hysteresis curves in figure 37(a & b). At a particular flow rate of N_2 (7 sccm in the poisoning branch of the hysteresis loop as shown in figure 37(c & d) and marked by an arrow sign), the sputtered material was deposited on a natively oxidized Si wafer. The arrangement of the target, substrate and rotatable shutter in the sputtering chamber is shown in figure 17(a). After stabilization of discharge voltage (60 s stabilization time), first of all the nitride film was deposited on the substrate during the first 10 min of reactive sputtering in the poisoned mode. The sputtering power was switched off and the substrate was removed via a load lock. The target was then sputter cleaned in the absence of reactive gas for 10 min. Again, after 60 min of reactive sputtering in the same poisoning mode, the sputtered material was deposited on another natively oxidized Si wafer for 10 min duration. The rotatable cylindrical shutter was used to expose the substrate only during the required interval of

sputter deposition. For both Al and Ti, the nitride films were deposited on natively oxidized Si wafers during the first 10 min of target poisoning and after 60 min of target poisoning at 7 sccm of N_2 flow rate in the poisoning mode, respectively. During 60 min of reactive sputtering in poisoning mode, the discharge voltage and chamber pressure remained stable. In the following, these two poisoning modes will be denoted by “short-term poisoning” and “long-term poisoning”. The temperature of the substrate was also measured during the 10 min deposition process at different poisoning conditions. The substrate was fixed on a Cu plate (30 mm in diameter and 3 mm in thickness) which was in contact with a temperature sensor as shown in figure 17(b). The temperature was measured using a platinum resistance (PT-100) temperature sensor. No active heating or cooling was employed and the substrate was kept at grounded potential to avoid the influence of substrate self biasing.

The surface morphology of the AlN and TiN films deposited at different poisoning conditions (short-term and long-term) was characterized by AFM (VEECO, diCaliber) in non-contact mode using a Si tip with 120 kHz resonance frequency. A field emission SEM (QUANTA, FEG 250) was used for micro structural analysis of the films. The crystallographic orientation of the films was determined by XRD using Cu Kα radiation (1.5406 Angstrom wavelength). The XRD measurement was done on an Empyrean Diffractometer equipped for thin film analyses with a parallel beam mirror on the primary side and a parallel plate collimator in the diffracted beam path. For detailed assessment of the composition of the films, a SPECS XPS-spectrometer equipped with a monochromatised Al-Kα x-ray source and a hemispherical WAL-150 analyzer with a 60° acceptance angle. Pass energies of 100 eV and 30 eV and energy resolutions of 1 eV and 100 meV were used for survey and detail spectra, respectively. For surface and bulk analysis, the samples were cleaned via Ar sputtering (3 kV Ar ions onto 2x2 mm^2 surface area, with a pressure of $2x10^{-7}$ mbar, resulting in about 5.5 μA current) for 20 and 600 s, which led to removal of about 12–15 nm and 40–50 nm on AlN and TiN samples, respectively. Data analysis was done using CASA XPS software employing transmission corrections, Shirly backgrounds and Scofield sensitivity factors. Charge correction was applied so the adventitious carbon peak (C-C peak) was shifted to 284.8 binding energy (BE). Curve fits using combined Gaussian-Lorentzian (GL(30)) peak shape were used to discern the components of detail spectra.

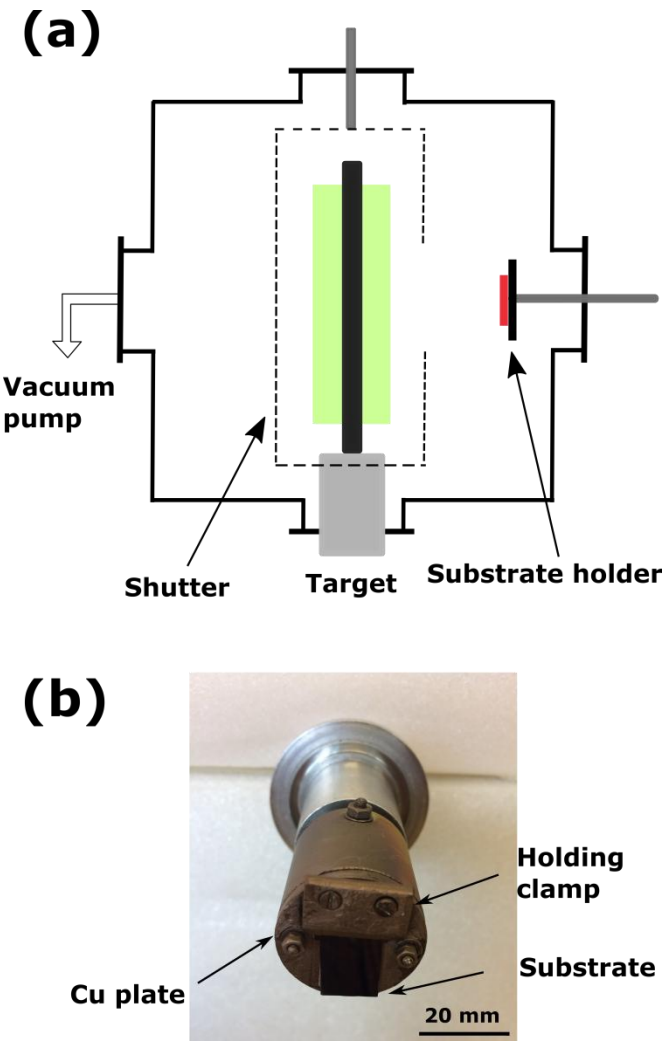

Figure 17: Schematic diagram showing experimental setup and substrate holder. (a) Arrangement of target, substrate and shutter in sputtering chamber. (b) Substrate holder, where the substrate is clamped on a Cu plate

4. In-situ assessment of target roughening[1]

As a first proof of concept for the in-situ roughness determination by laser reflectometry, the roughness evolution of non-reactively sputtered targets was investigated. The cylindrical magnetron targets were considered as uniformly eroded in a given region as shown by a grey zone in figure 18(a). As previously described, the target was hit by a laser beam in a way that the incident beam and its specular reflection enclose an angle of 90°. The specular and diffuse reflection of the laser is captured on a screen. If the beam has a finite diameter, for simplicities sake it can be assumed that the intensity of the beam is constant throughout the beam and zero otherwise. Therefore the beam can be decomposed into an array of parallel partial beams of equal intensity. If the surface of the target is not completely smooth then these partial beams will be reflected from the facets of the surface, if their linear extension is considerably larger than the wavelength of the laser. Due to large area surface facets the reflection of light can be employed for surface characterization.

The surface of the eroded region can be modelled as a random arrangement of tilted plane facets. Figure 18(b) illustrates the tilted facets of the eroded surface under investigation. For simplicity it was assumed that the intensity profile in the vertical direction is influenced by the facets only tilted along the tangential plane of the cylinder as shown in figure 18(b). For the reflection of light, it was also assumed that the size of the facets (1–4 µm, as independently measured by profilometry) is considerably larger than the wavelength (532 nm) of the incident light. If the tilt angle, α, is zero, the facet is parallel to the tangential plane as shown. The magnified section in figure 18(b) illustrates the portion of the target surface hit by the laser beam.

[1]The contents of this chapter are partially published in *Vacuum* **138** (2017) 205-212.

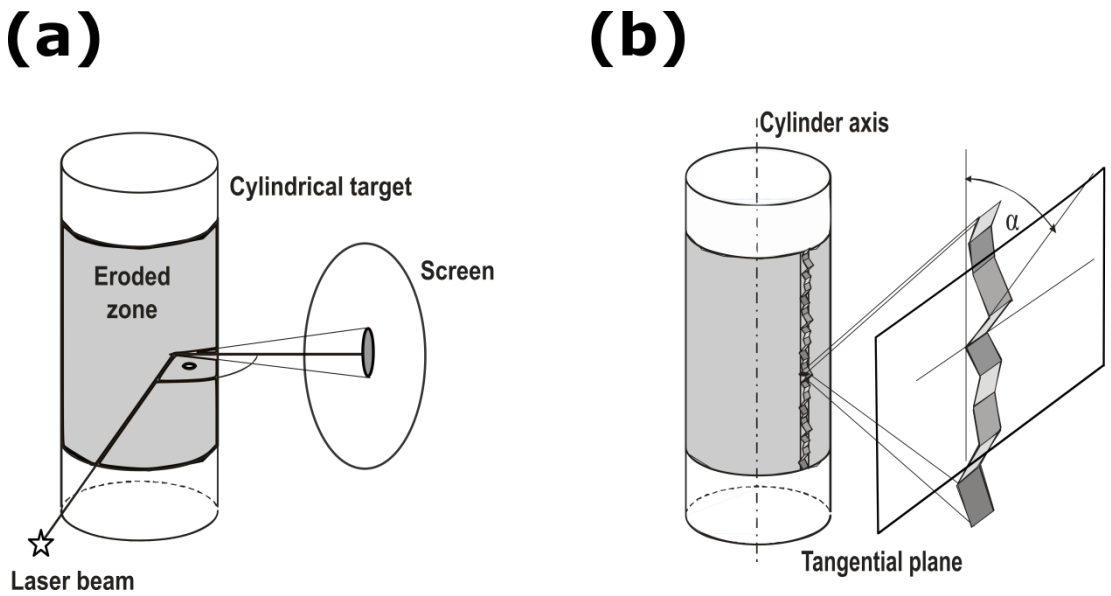

Figure 18: Schematic diagram for reflection of laser beam from the eroded region of a cylindrical target (a) A laser beam hits the surface of the target within the erosion zone and its reflection is captured on the screen. (b) Illustration of the tilted facets of the eroded surface under investigation.

4.1 Reflection of a beam of light from a tilted plane

First of all one has to investigate the reflection of a beam from a tilted plane in this special geometry. Analysing the situation according to figure 18(b), let us consider a beam impinging on a plane at an angle of 45°, the plane is the tangential plane to a cylinder with an axis perpendicular to the paper plane as shown in figure 19. If the beam is considered to consist of an array of parallel partial beams of equal intensity then the problem can be reduced to the reflection of one beam from a tilted plane. In the geometry of the experimental set-up, the incidence angle of the beam relative to the tangential plane is constant, thus making the intensity of the reflected partial beams proportional to the area of the facet. The direction of the reflected beam can be calculated by considering the reflection of a beam from a tilted plane. This will be done in the following for our given experimental geometry as shown in figure 19.

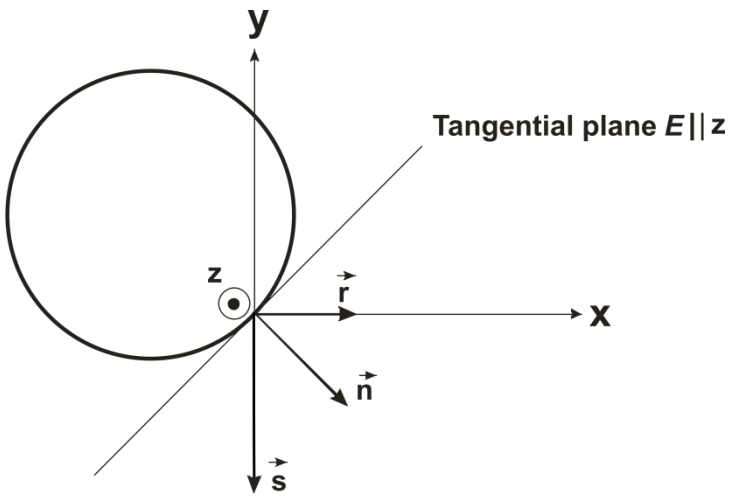

Figure 19: Reflection of a beam of light from a cylindrical target. A incident beam impinges on the tangential plane ***E*** and is reflected along the x-Axis.

In the coordinate system of figure 19, the vector $\vec{s}$ is given by

$$\vec{s} = \begin{pmatrix} 0 \\ -1 \\ 0 \end{pmatrix}$$

This vector representing the incident beam remains unchanged. Now let us consider the plane tilted by an angle α relative to the *z*-axis. The plane shall still intersect the cylinder in the origin of the coordinate system given in figure 19. The upper part of the plane moves towards the centre of the cylinder, the lower part away from it. Thus, the normal vector of ***E***, $\vec{n}$, is tilted out of the *xy*-plane also by the angle α and we obtain

$$\vec{n} = \begin{pmatrix} \frac{\cos\alpha}{\sqrt{2}} \\ -\frac{\cos\alpha}{\sqrt{2}} \\ \sin\alpha \end{pmatrix}$$

The angle θ between the surface normal of the tilted plane and the incident beam amounts to:

$$\cos\theta = \vec{s} \cdot \vec{n} = \frac{\cos\alpha}{\sqrt{2}} \tag{6}$$

The beam reflected from the tilted plane has to lie in the plane which is defined by $\vec{s}$ and

$\vec{n}$. The normal vector of this plane $\vec{u}$ is given by the outer product, $\vec{s} \times \vec{n}$.

$$\vec{u} = \vec{s} \times \vec{n} = \begin{pmatrix} -\sin\alpha \\ 0 \\ \frac{\cos\alpha}{\sqrt{2}} \end{pmatrix}$$

To calculate the direction of the beam reflected from the tilted plane one has to make use of the following relations:

(i) The reflected beam has to lie in the plane which is defined by $\vec{s}$ and $\vec{n}$ and therefore, the inner product of the vector $\vec{u} = \vec{s} \times \vec{n}$ which is the normal vector to this plane, $\vec{u} \cdot \vec{r} = 0$.

(ii) The vector $\vec{r}$, which represents the reflected beam, shall be normalized to one.

(iii) The angle between the reflected beam and $\vec{n}$ has to be equal to θ

Mathematically this means:

$$\begin{aligned} \vec{u} \cdot \vec{r} &= 0 \\ \vec{r} \cdot \vec{r} &= 1 \\ \vec{r} \cdot \vec{n} &= \cos\theta \end{aligned} \tag{7}$$

After some calculation the components (for details see Appendix) of the vector representing the reflected beam $\vec{r}$ are

$$\begin{aligned} r_x &= \frac{1}{1 + tan^2\,\alpha} \\ r_y &= \frac{tan^2\,\alpha}{1 + tan^2\,\alpha} \\ r_z &= \frac{\sqrt{2} \cdot tan\,\alpha}{1 + tan^2\,\alpha} \end{aligned} \tag{8}$$

What remains to be done is to intersect the line given by $\vec{r}$ with a plane, which represents the screen to get the position of the reflected beam on the screen. The screen is represented by a plane parallel to the *yz*-plane in a distance *d* from the origin, the equation of this plane is

$$x = d$$

Performing this intersection yields the coordinates of intersection point as:

$$
\begin{aligned}
x_i &= d \\
y_i &= d \cdot \tan^2 \alpha \\
z_i &= d \cdot \sqrt{2} \cdot \tan \alpha
\end{aligned}
\tag{9}
$$

This means that for small tilt angles α, the deflection in y-direction is negligible and the tilt angle α can directly be calculated to be

$$
\alpha = \arctan\left(\frac{z_i}{d \cdot \sqrt{2}} \right) \tag{10}
$$

For reconstructing a surface profile, i.e. to calculate the ensembles α_i of the tilted facets marked by the index *i* that make up the surface, one can first assume that the vertical deviation of a partial beam is only influenced by the tilt angle and not by the vertical position of the facet within the beam. As justified before, this corresponds to the assumption that all vertical deviations of the diffuse reflection pattern only result from the facet tilt and not from an eventual vertical displacement of a facet. This holds if the beam diameter is small when compared to the extension of the erosion zone. As the intensity value at each pixel, *I(z)*, corresponds to a certain tilt angle of a plane facet, the mean tilt angle can be calculated as

$$
\overline{\alpha} = \frac{I(z) \cdot \alpha(z)}{\sum_{0}^{1500} I(z)} \tag{11}
$$

According to our measurement geometry as shown in figure 20, the radius of the target was 22 mm and the distance between the screen and the incident point of laser was set as 75 mm. The laser diameter is 3 mm, which is significantly smaller than vertical and the lateral extension of the erosion zone.

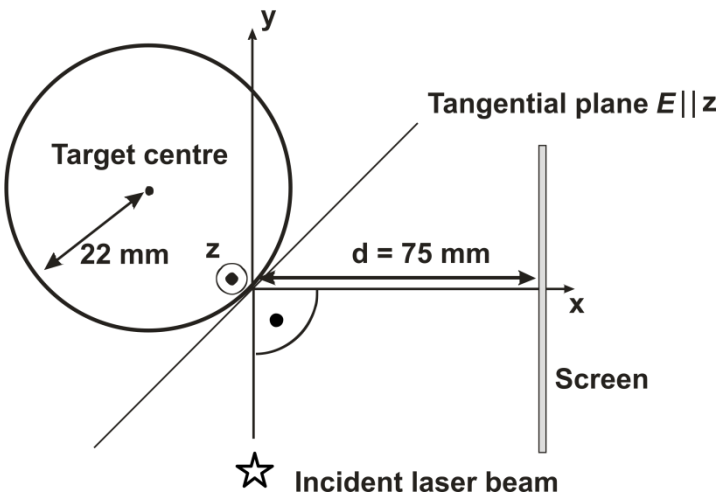

Figure 20: Geometry of the measurement system.

A typical image recorded on the screen, including the co-ordinate system given in figure 20, is displayed in figure 21(a).

In the image displayed in figure 21(a), first of all, all coordinates have to be converted into pixel-values: the origin is located at y_{p0} = 2800 pixel and z_{p0} = 3050 pixel. 1 pixel corresponds to 0.02 mm (20 µm). So the coordinates from the above calculation can be converted into pixel values as follows:

$$\begin{aligned} y_p &= y_{p0} + \left(\frac{1}{0.02}\right) \cdot d \cdot \tan^2 \alpha \\ z_p &= z_{p0} - \left(\frac{1}{0.02}\right) \cdot d \cdot \sqrt{2} \cdot \tan \alpha \end{aligned} \tag{12}$$

With d = 75 mm one obtains the yellow line displayed in figure 21(b), which ideally indicates the reflections from a facet with tilt angle α relative to the origin of the screen. Lateral and vertical offsets within the region where the beam hits the target are neglected. As it is visible from figure 21(b), up to tilt angles of α ≈ 10° the deviation from a vertical line is rather small. As also visible from equation (9), it is also visible that a big part of the diffuse reflection intensity is located in this region. So, for simplicities sake, sections through the reflection pattern will be vertical (i.e. in z-direction) and will have a length of 1500 pixels at the maximum (see green line in figure 21(b)).

Finally, a simple algorithm that attempts to reconstruct a surface profile from the diffuse reflection pattern is presented in the following.

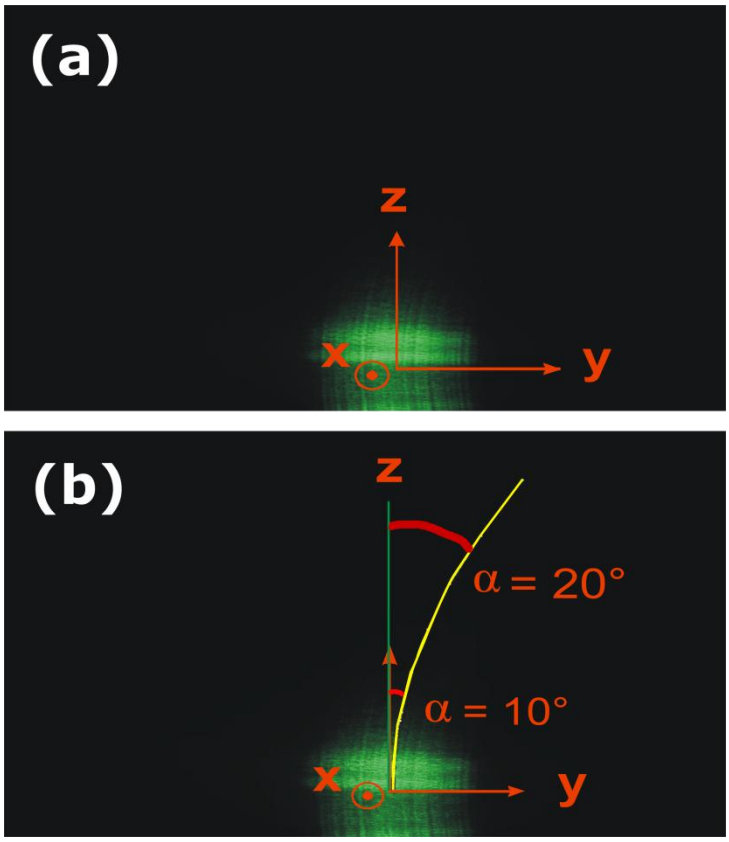

Figure 21: The reflected images captured on the screen. (a) Diffuse reflection for Al target captured on the screen with given co-ordinate system. (b) Position of the reflections from facets with given tilt angles α. If all these facets were located in the origin of the co-ordinate system, their reflection will be located along the yellow line. A vertical intensity scan with a length of 1500 pixel is represented by the green line.

4.2 Algorithm for the reconstruction of a linear surface profile from a diffuse reflection pattern

First, from an image of reflection patterns line scans with a length of 1500 pixels (corresponding to 30 mm on the screen) in the coordinate system given in figure 21(a) are extracted. 1500 pixel were chosen because scattered intensity is not observed any more for distances farther from the origin. The lateral offset given by the cylindrical geometry is neglected. Figure 22 shows average (10 values) line scans for Al, Cu and Ti for different sputter durations, respectively. The corresponding tilt angles calculated by using equation (10) are also shown along the upper x-axis. The reflected intensity distribution is applicable to the measurement of surface roughness [61]. From figure 22(b), it is immediately visible that the over-all intensity of the reflection for Cu is lower, which leads

to the expectation that the roughness of Cu is higher.

First of all, from the reflected intensity profile, the correlation length λ was measured. In general, the correlation length is inversely proportional to the diffuse peak width (FWHM) of the intensity profile. For an arbitrary surface exponent, the correlation length was estimated from the intensity profile using the following relation [62].

$$\lambda = \frac{2}{FWHM} \tag{13}$$

Now, the proposed model was used to generate the surface height profiles from the intensity profiles of Al, Cu and Ti for different sputtering durations and eventually use these generated profiles to extract the roughness parameters. It was assumed that the length of a facet tilted by a given angle is proportional to the intensity value in the reflected pattern. The total length of all these facets was added up to 3 mm (diameter of the laser beam). For each non-zero intensity value at a different pixel position, the tilt angle was calculated by equation (10). The measured tilt angles were then randomly multiplied by ±1, representing upwards/downwards tilt of a surface facet. Once these lengths and angles have been defined, the code constructs a surface profile by randomly selecting an element and stitching this element to the last height value of the profile existing so far. Then this element is deleted and the algorithm is repeated until no more elements are left. Once this is the case, this profile is converted to a profilometer-like data set containing 6000 equally spaced height values (distance: $\Delta s = 50\mu m$).

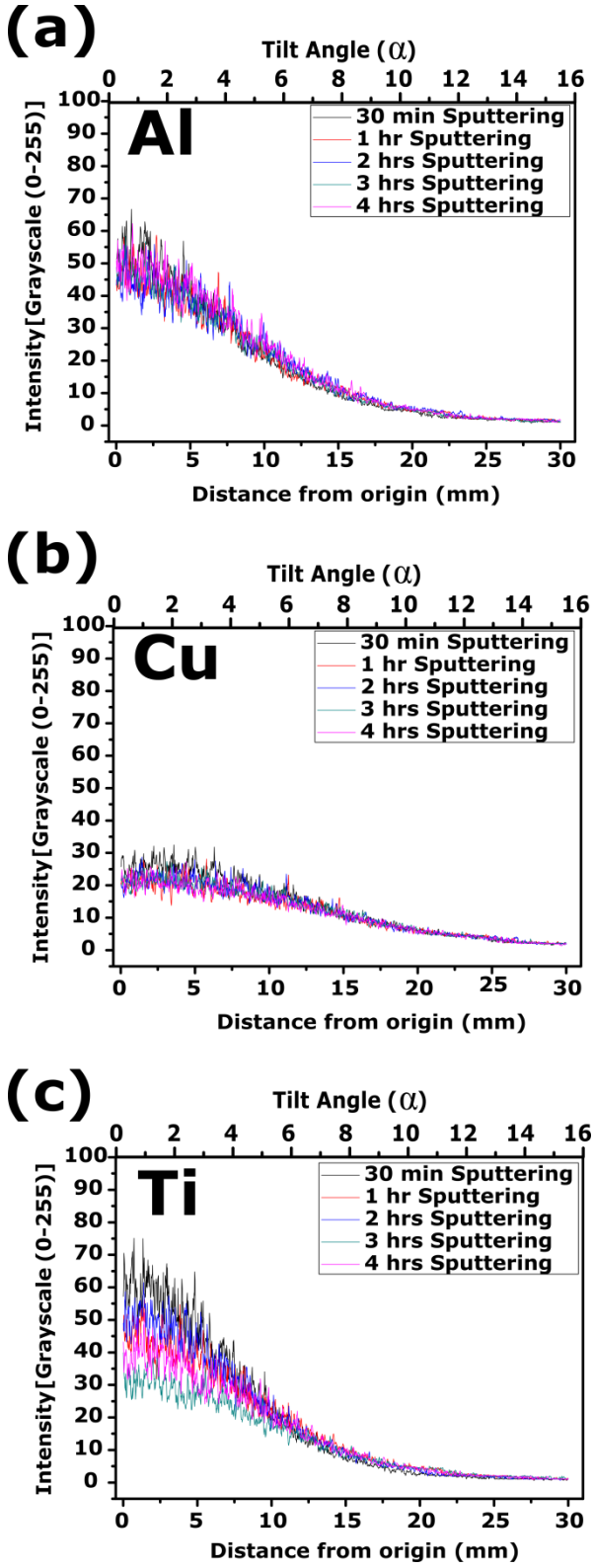

Figure 22: Reflected intensity scans with a length of 1500 pixel (30 mm on the screen) and the corresponding tilt angles after different sputtering time from Al (a), Cu (b) and Ti (c) targets, respectively. The lower over-all reflected intensity from the Cu target is clearly visible.

The correlation function *R(x)* of each generated profile was calculated as

$$R(x) = \frac{1}{N-n} \sum_{i=1}^{N-n} (h_i) \cdot (h_{i+1}) \tag{14}$$

Where N is the total number of data points and n can assume the values from 0–(N-1). The correlation function, *R(x)*, was drawn against the lateral positions x_i of the height values. The curve exponentially decays with increasing x values ($R(0)$=1). *R(x)* usually decays to zero and the shape of the curve depends on the type of the surface [63]. From this correlation function, the correlation length λ was calculated, which is the distance over which this function falls by 1/e of its maximum value as given below [64]

$$R(x) = \exp(-\frac{|x|}{\lambda}) \tag{15}$$

For each generated profile, the correlation length was calculated and compared with that estimated from that of the intensity profile. Only those generated profiles were selected whose correlation lengths lie in between ±10 percent of the values calculated from the intensity profile. Then from these 50 so generated profiles, the average values of global variables, RMS roughness, skewness, kurtosis and correlation length are calculated for 6000 measurement points (N = 6000) as follows (Equations 16,17, 18 and 19).

RMS-Value:

$$R_{RMS} = \sqrt{\frac{1}{N} \cdot \sum_{i=1}^{N} h_i^2} \tag{16}$$

Skewness-Value:

$$S = \frac{1}{R_{RMS}^3} \cdot \sum_{i=1}^{N} h_i^3 \tag{17}$$

Kurtosis-Value:

$$C = \frac{1}{R_{RMS}^4} \cdot \sum_{i=1}^{N} h_i^4 \tag{18}$$

Correlation-Length (λ obtained from): $R(x) = \exp(-\frac{|x|}{\lambda})$ (19)

4.3 Determination of roughness parameters

The RMS roughness and the correlation length are two essential aspects to describe the roughness of a surface [65]. The targets of different materials were sputtered for different sputtering durations. With the code described above an average of 50 profiles

extracted from the intensity patterns were constructed. Figure 23(a) shows the average RMS values for 50 generated height profiles and height profiles measured by profilometer during different sputtering durations for Al, Cu and Ti. The RMS values of generated profiles for Al and Ti are very close to those of the profilometer measurements. An under-estimated value was observed for Cu with the generated profiles. Although, figure 23(a) shows the underestimated RMS value for Cu as compared to the profilometer values, figure 23(b) shows the higher values for Cu in comparison to Al and Ti if generated profiles are considered only. This shows that our model predicts a similar trend in the roughness measurement. The plausible reason for the deviation to the values obtained from profilometry could be the different surface structure of the Cu surface.

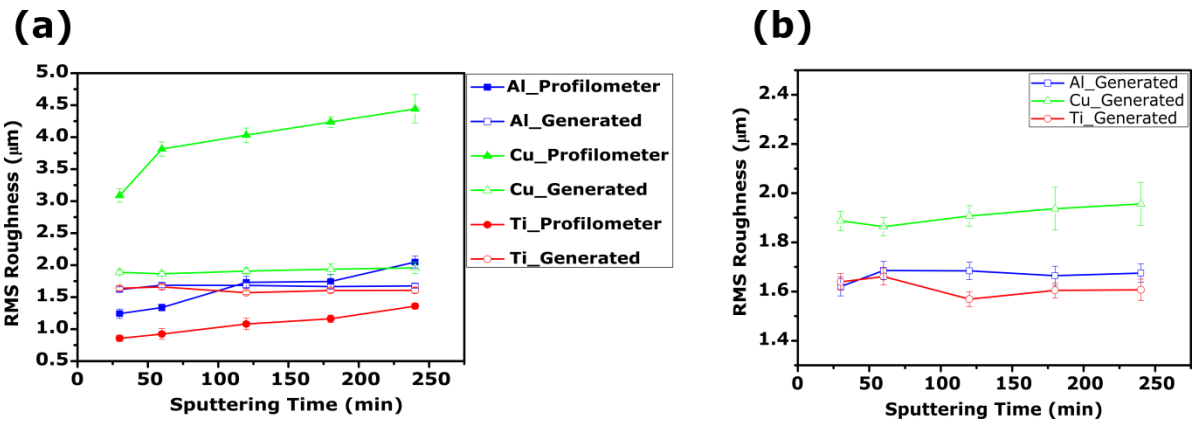

Figure 23: Average RMS values for 50 generated profiles during different sputtering durations. (a) Comparison of average RMS values of generated height profiles and height profiles measured by profilometer for Al, Cu and Ti targets. (b) Average roughness of the generated profiles for Al, Cu and Ti targets. It shows the similar trends of roughness as it was investigated from profilometer measurement.

To further investigate the RMS value of Cu, the mean tilt angles for Al, Cu and Ti target surfaces were determined from the measured profiles and also from the reflected intensity patterns. The slopes of the surface facets were calculated from the height profiles observed from the profilometer. The tilt angles were determined by taking the height values of the neighbouring points using the following equation.

$$\alpha' = \arctan\left(\frac{y_{j+1} - y_j}{x_{j+1} - x_j}\right) \tag{20}$$

where x_j and y_j represent the lateral and vertical positions of the respective facet. Finally, the mean tilt angle was calculated for the whole scan length (3 mm) of the profilometer measurements by taking the arithmetical mean of all α'.

Figure 24(a) shows the mean tilt angles for Al, Cu and Ti targets for different sputtering durations. The measurements represented with filled symbols (■, ▲, ●) were calculated from the height profiles measured by the profilometer. The target surfaces were scanned for the scan length of 3 mm and the tilt angles were calculated by using equation (20). Similarly, the mean tilt angles were also calculated from the patterns of reflected intensity profiles by using equation (10) (represented by empty symbols:□, △, ○). The mean tilt angles for Cu are significantly higher than those of Al and Ti, showing the higher roughness of the Cu target surface. For Al and Ti, the values of the mean tilt angles measured both from profilometer and reflectometry show the similar trend. However, for Cu, the mean tilt angle measured from the reflected intensity pattern shows a significantly lower value. This discrepancy in measurement is due to shadowing and masking effects of the tilted facets. Due to higher roughness, a significant portion of the incident laser beam was not reflected towards the screen due to these effects. The higher roughness resulted in a wider spread in diffuse components, with a longer tail in the intensity profile as evident for Cu in figure 22(b). This means that although the total intensity is decreased, no single components (for instance at high reflection angles) of the intensity profile are selectively suppressed. It can be concluded that the mean tilt angle measured form the intensity distribution of the reflected beam from the target surface can be utilized for the in-situ assessment of the target surface. However, for cylindrical targets with higher roughness (RMS value > 3 μm), due to shadowing and masking affects, under-estimated values of the mean tilt angles are obtained.

Figure 24(b) shows the optical images of sputtering targets of Cu and Ti after four hours of sputtering. The deep valleys on the surface, which are clearly visible from the optical image of the Cu target, are responsible for shadowing and masking. For the Cu surface with its large roughness, these valleys prevent the measurement of the true intensity profile.

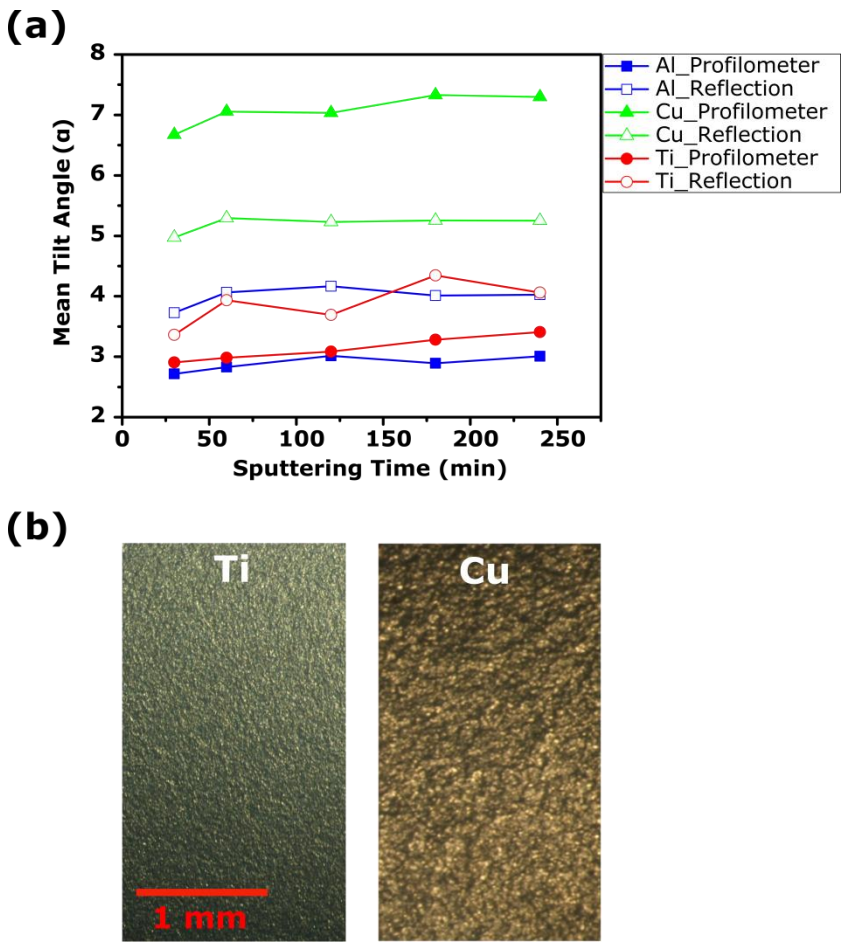

Figure 24: The mean tilt angles for Al, Cu and Ti targets and optical images of Cu and Ti Targets. (a) Mean tilt angles for Al, Cu and Ti targets at different sputtering durations determined from profilometry and reflectometry. (b) Optical images of Ti and Cu targets after four hours of sputtering.

The second essential parameter, the correlation function, which explains the variation of heights along the surface, was also measured. The correlation length λ was calculated for both, profiles measured by profilometry and the generated profiles. Figure 25(a) shows the correlation length of generated profiles for Al, Cu and Ti targets with different sputtering durations. The correlation lengths of measured profiles and that of generated profiles fit very well for Cu and Ti. However, the correlation length of measured Al profiles was overestimated and shows large error bars. This discrepancy can be explained from the optical image of the Al target as shown in figure 25(b) which illustrates elliptical mound formation. The profilometer measurements were performed horizontally along the axis of the cylindrical target (see figure 25(b)). The height profiles measured by the profilometer for both target surfaces are also shown in figure 25(b). As evident, the measured profiles show very long correlation lengths due to long axially extended features

in horizontal direction. They probably result from the target production which, for Al, may involve extrusion casting. However, as evident from the optical image the surface mounds are very short along the vertical direction. The high measured correlation length can therefore be attributed to this one-dimensional hilly surface structure. However, the overall correlation length seems much smaller than the measured one if only features resulting from sputtering are considered (circles in figure 25(b)).

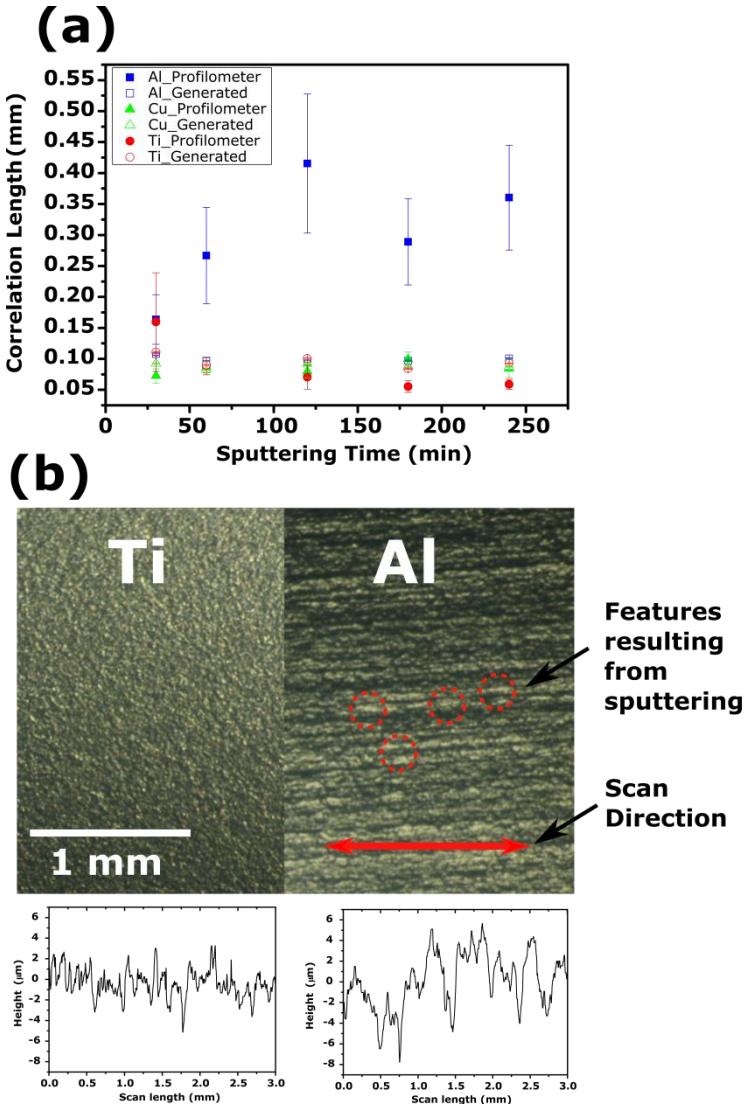

Figure 25: The correlation length of generated profiles for Al, Cu and Ti, and optical image of Al and Ti targets. (a) The correlation length of generated profiles for Al, Cu and Ti targets with different sputtering durations in comparison with λ assessed from profilometry. (b) The optical image of Al sputtering target after four hours of sputtering compared to a Ti surface sputtered for the same time with corresponding height profiles. Long horizontally extended mounds are clearly visible in the optical image and from the roughness morphology.

For completeness, the shape specific higher order statistical parameters, skewness and kurtosis were also determined for both measured and generated profiles. Figure 26(a), (b) and (c) shows the kurtosis and skewness values of Al, Cu and Ti, respectively. The measured and generated values coincide extremely well for all three sputtering targets. As visible from figure 26, skewness values indicate that there is no asymmetry of the profiles, which can be expected. The skewness values for Al (measured: – 0.20 ± 0.11, generated: 0.01 ± 0.05), Cu (measured: 0.14 ± 0.07, generated: 0.02 ± 0.06) and Ti (measured: 0.07 ± 0.09, generated: – 0.01 ± 0.06) are all around zero. In the case of kurtosis, Al (measured: 2.97 ± 0.18, generated: 2.80 ± 0.08), Cu (measured: 2.82 ± 0.11, generated: 2.87 ± .09) and Ti (measured: 2.97 ± 0.16, generated: 2.79 ± 0.08) target exhibit values close to 3. For all, Al, Cu and Ti the generated and the measured values are systematically close to the fully Gaussian kurtosis value of 3.

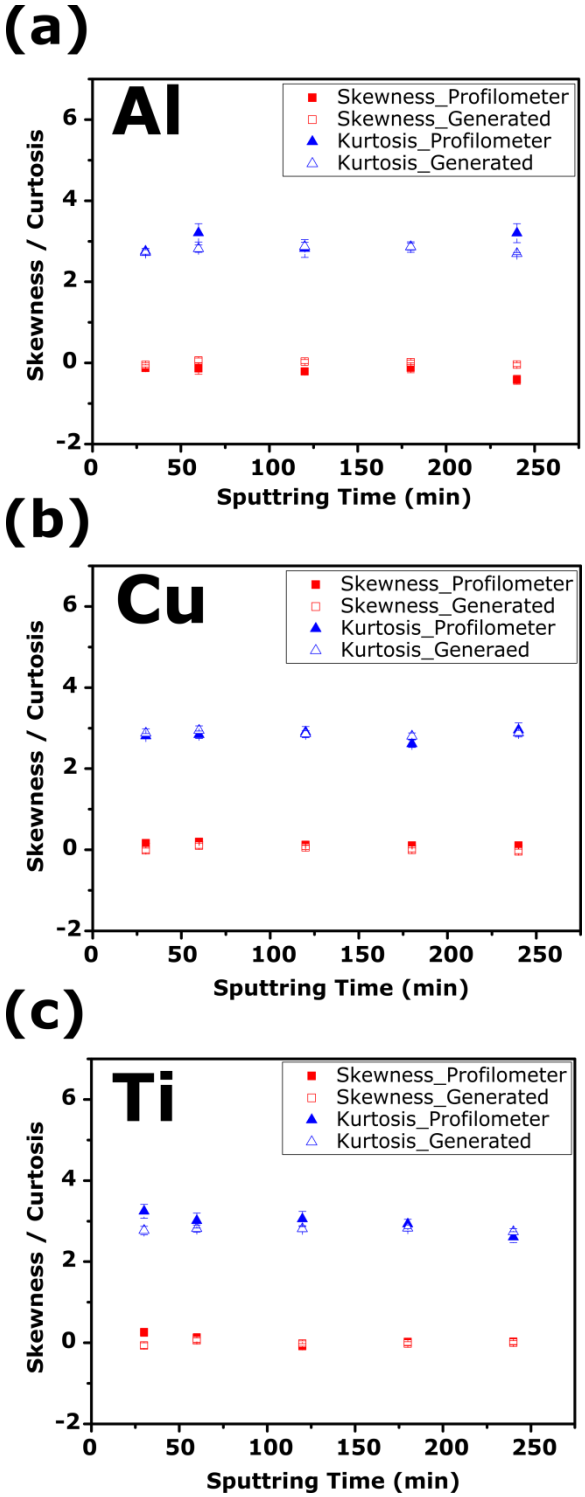

Figure 26: Average skewness and kurtosis values for 50 generated profiles and measured profilometer scans for (a) Al, (b) Cu and (c) Ti targets.

Finally, in figures 27, 28 and 29 a direct comparison between measured and generated profiles is given for Al, Cu and Ti for different sputtering durations, respectively. It can also be seen from these figures that there is a lower probability that the profile

changes its direction at a small lateral length scale for the experimentally determined profiles. This is due to the fact that the algorithm joins the facets of the generated profile with complete randomness (tilts are positive or negative with equal probabilities). Although the algorithm cannot reproduce the exactly same surfaces, the profile's peak-to-peak values lie well within those of the measured profiles thus resulting in good agreement of the RMS and correlation length values.

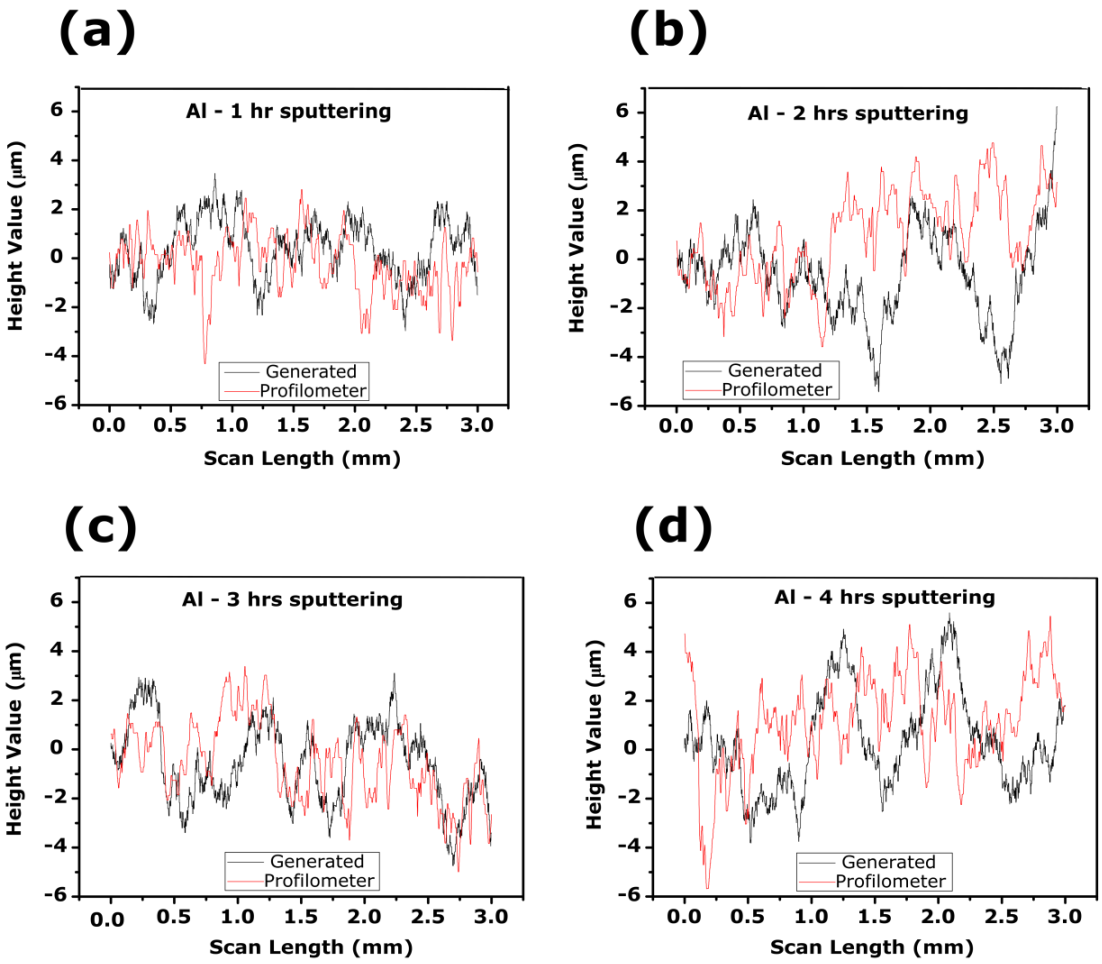

Figure 27: Direct comparison of measured and generated surface profiles for an Al target. (a) Measured and generated surface profiles for an Al target after one hour of sputtering, (b) two hours of sputtering, (c) three hours of sputtering and (d) four hours of sputtering.

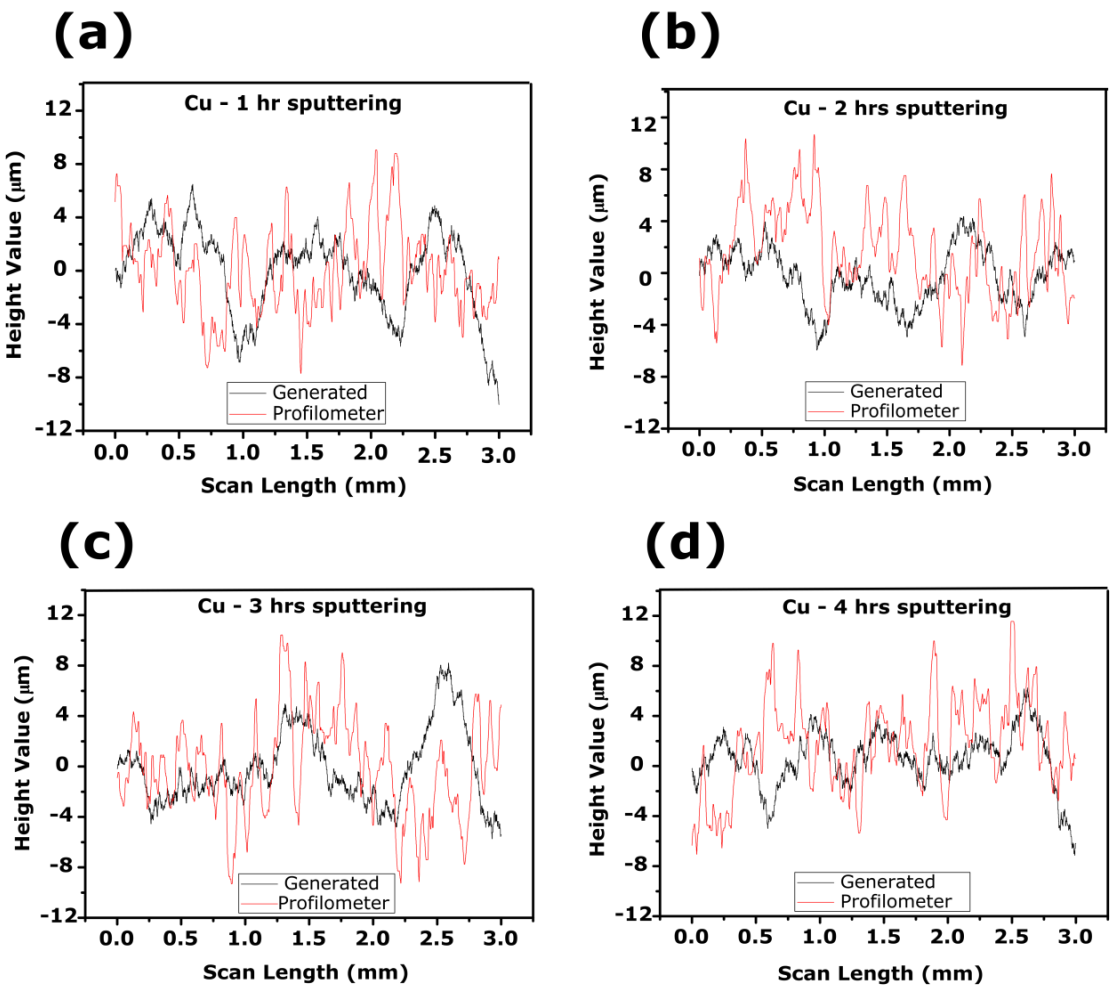

Figure 28: Direct comparison of measured and generated surface profiles for Cu target. (a) Measured and generated surface profiles for Cu target after one hour of sputtering, (b) two hours of sputtering, (c) three hours of sputtering and (d) four hours of sputtering.

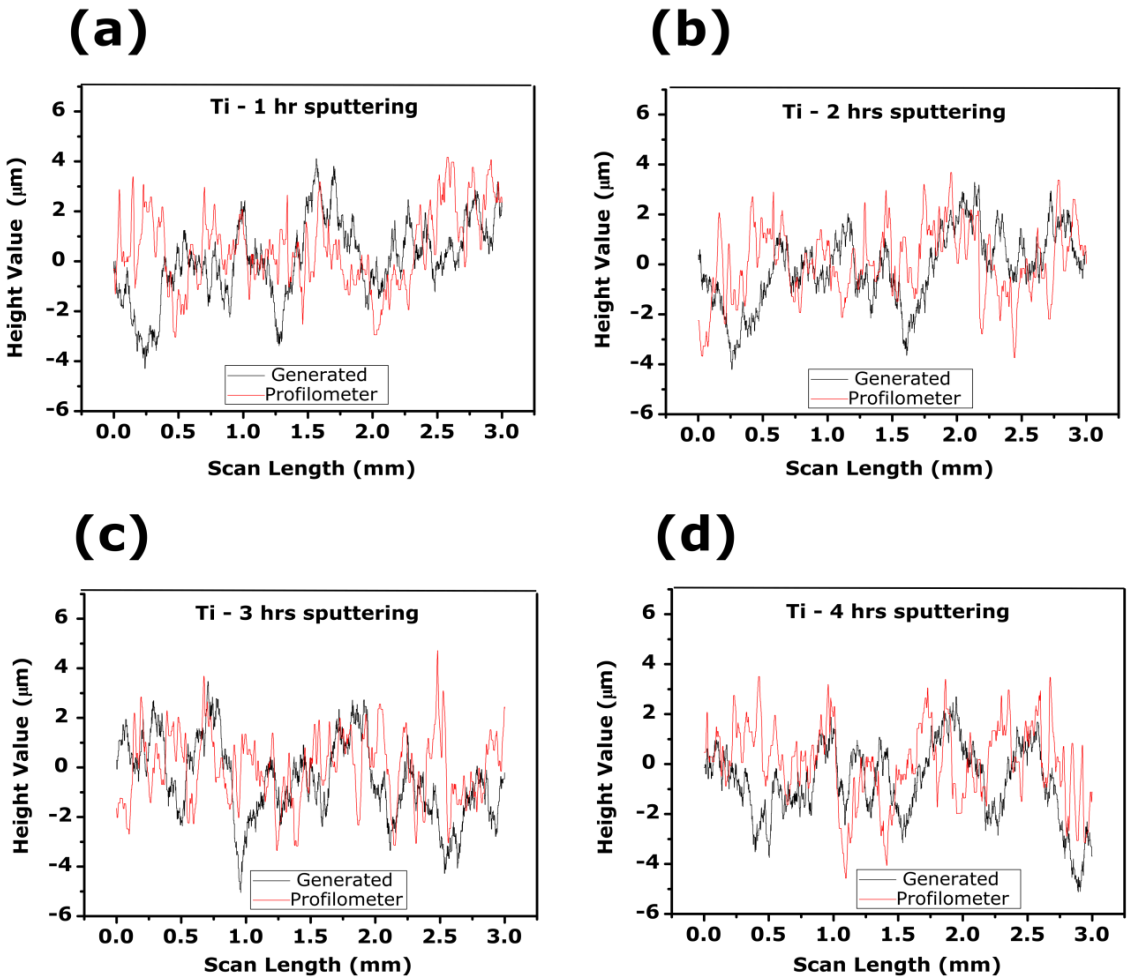

Figure 29: Direct comparison of measured and generated surface profiles for Ti target. (a) Measured and generated surface profiles for Ti target after one hour of sputtering, (b) two hours of sputtering, (c) three hours of sputtering and (d) four hours of sputtering.

To summarize, with the described in-situ surface analysis of a sputtering target, it is possible to use the reflectometry tool to access a profile shape when combined with the software based profile reconstruction. This allows for monitoring the onset of target roughening and to examine the temporal behaviour of roughness evolution upon erosion. An option not yet explored would also be the possibility to predict the onset of target failure/melting by unusual behaviour of the reflection pattern (e.g. large deviation of the reflected laser beam position).

5. Assessment of target poisoning in reactive sputtering by laser reflectometry[2]

In the previous section, it was shown that laser reflection is a useful tool for the assessment of the surface roughness. As it was noticed that poisoned targets have a different, shinier appearance when comparing them to targets sputtered in metallic mode (see figure 16), this section shall clarify, if reflectometry can be used to monitor target poisoning. During reactive sputtering, the target uptake of reactive gas varies with reactive gas flow rates. When the flow rate of reactive gas is low, the sputtering process balances the compound formation on the target surface and the target is considered to be in metallic mode. At higher reactive gas flow rates, the target surface is significantly covered by the compound layer. As a result, the sputtering parameters are significantly changed and the target transforms to poisoned mode. In addition to the chemical composition of the target surface, the compound layer alters the surface morphology of the target surface. The non-uniform plasma surface interactions also vary the poisoning mechanism across the target surface. Consequently, at different sputtering conditions, the target poisoning state could be reflected in the state of the target surface.

For the assessment of target poisoning, the poisoned surface of the target was again assumed as a random arrangement of mirror-like facets [11, 12]. A laser beam reflected from these facets was utilized for surface roughness evaluation. From the reflected intensity profile, the mean tilt angle of the target surface, which was found to be a very sensitive quantity, was evaluated. A change in mean tilt angle reflects the change in surface roughness at different poisoning levels. Deposition rates were also measured at different poisoning time. Finally, the poisoned surfaces of targets were sputter cleaned in non-reactive mode. Longer de-poisoning time were observed after long-term poisoning. The roughness evolution due to surface poisoning was correlated with the de-poisoning time. It was found that in reactive sputtering, the target poisoning can be monitored by measuring the target roughness evolution.

[2]The contents of this chapter are partially published in *Surf. Coat. Technol*., **324** (2017) 345–352

5.1 Hysteresis behaviour during reactive sputtering

In reactive sputtering, the compound formation on the target surface is balanced by the sputtering process. With increasing reactive gas flow, the compound formation becomes significant and the erosion rate decreases. With low erosion rate, the reactive gas molecules find less metal atoms to form a compound which results in higher reactive gas pressure. Consequently, there is an abrupt decrease in erosion rate at a certain level of reactive gas pressure. This transition of the target surface from metal to compound state is defined as poisoning. The discharge voltage and reactive gas partial pressure are significantly changed at this point. By decreasing the reactive gas flow, the target surface can again switch from poisoned to metallic state. However, if the reactive gas flow is decreased at the same rate, the transition from poisoned to metallic state is observed at a lower flow rate than its transition to the poisoned mode during the increasing cycle of the reactive gas. So, there is a well-known hysteresis effect during the increasing and decreasing cycle of the reactive gas flow [66]. To study the poisoning of the targets, such threshold flow rates of reactive gas were established from hysteresis curves. At the starting point of the poisoning state an avalanche like change was observed in both system pressure and discharge voltage values. At complete poisoning of the target surface, the flow rate of reactive gas was stepwise decreased. Again at a certain level of reactive gas flow, the system parameters go back to those of the metallic mode. Figure 30 shows the hysteresis loops between the rise and fall of reactive gas flow rate and discharge voltage for Al and Ti targets during reactive sputtering. A corresponding hysteresis effect is also observed in the partial pressure of the reactive gas [33]. Figure 31 shows the hysteresis curve for system pressure at different flow rate of reactive gases for Al and Ti targets. The variation of discharge voltage is related to the ion-induced secondary electron emission from the target surface. The secondary electron emission yields from different compounds (oxides and nitrides) depend on their electronic properties [67].

Within the hysteresis loops, four points *a*, *b*, *c* and *d* are marked for zero flow rate of reactive gas (metallic mode), centre point of the hysteresis width in metallic mode (transition region metallic mode), centre point of the hysteresis width in poisoned mode (transition region poisoned mode) and complete poisoning mode (poisoned mode), respectively. Later, the poisoning evolution was observed at these four points with varied sputtering time. The hysteresis behavior for the four different combinations of reactive gas and sputtered material is discussed in detail in the following:

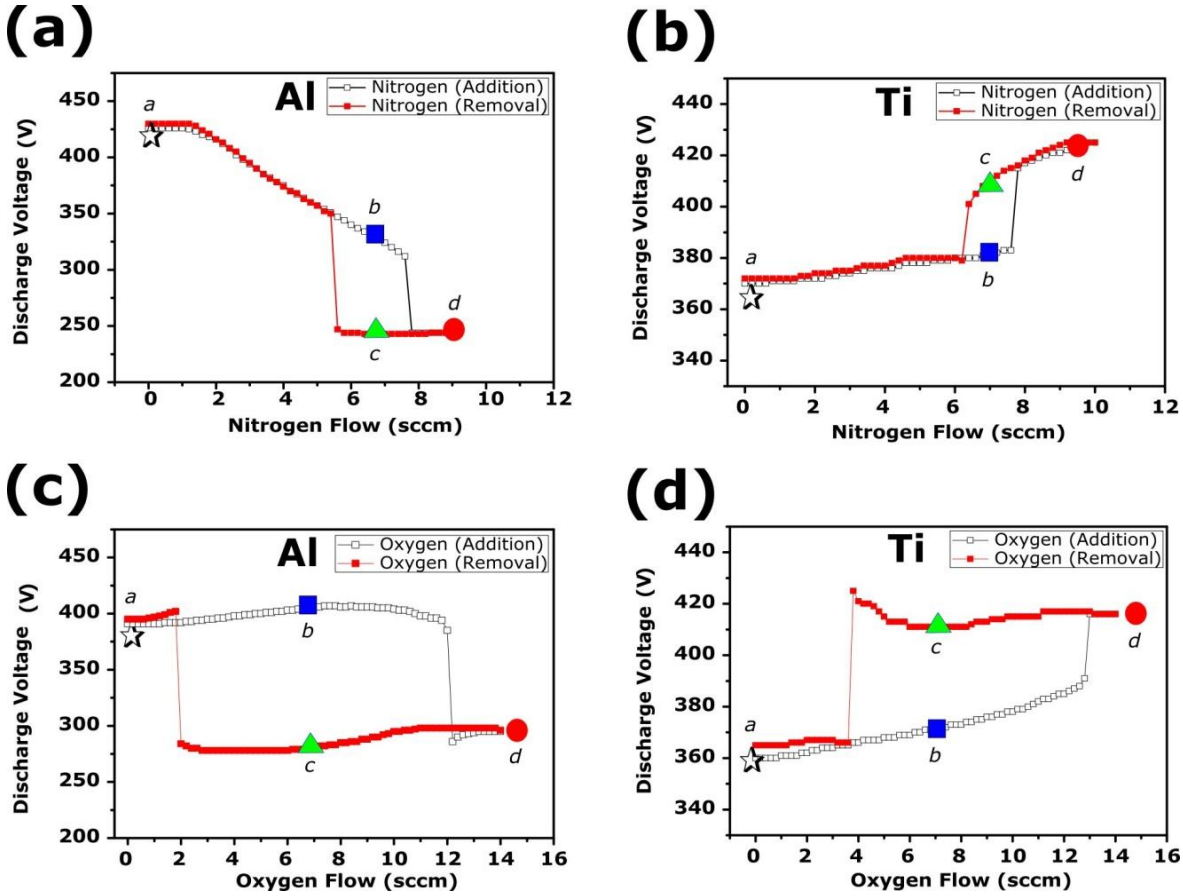

Figure 30: Hysteresis curves of reactive gas flow rate and discharge voltage for Al and Ti targets during reactive sputtering. (a) For Al+N_2, the discharge voltage drops due to the higher secondary electron emission from AlN compound. (b) For Ti+N_2, the discharge voltage increases with increasing nitrogen flow due to a lower yield of secondary electrons from the target surface. (c) For Al+O_2, the discharge voltage decreases as the oxide layer on target surfaces increase the secondary electron yield. (d) For Ti+O_2, the discharge voltage increases with increasing oxygen content due to a decrease in secondary electron emission.

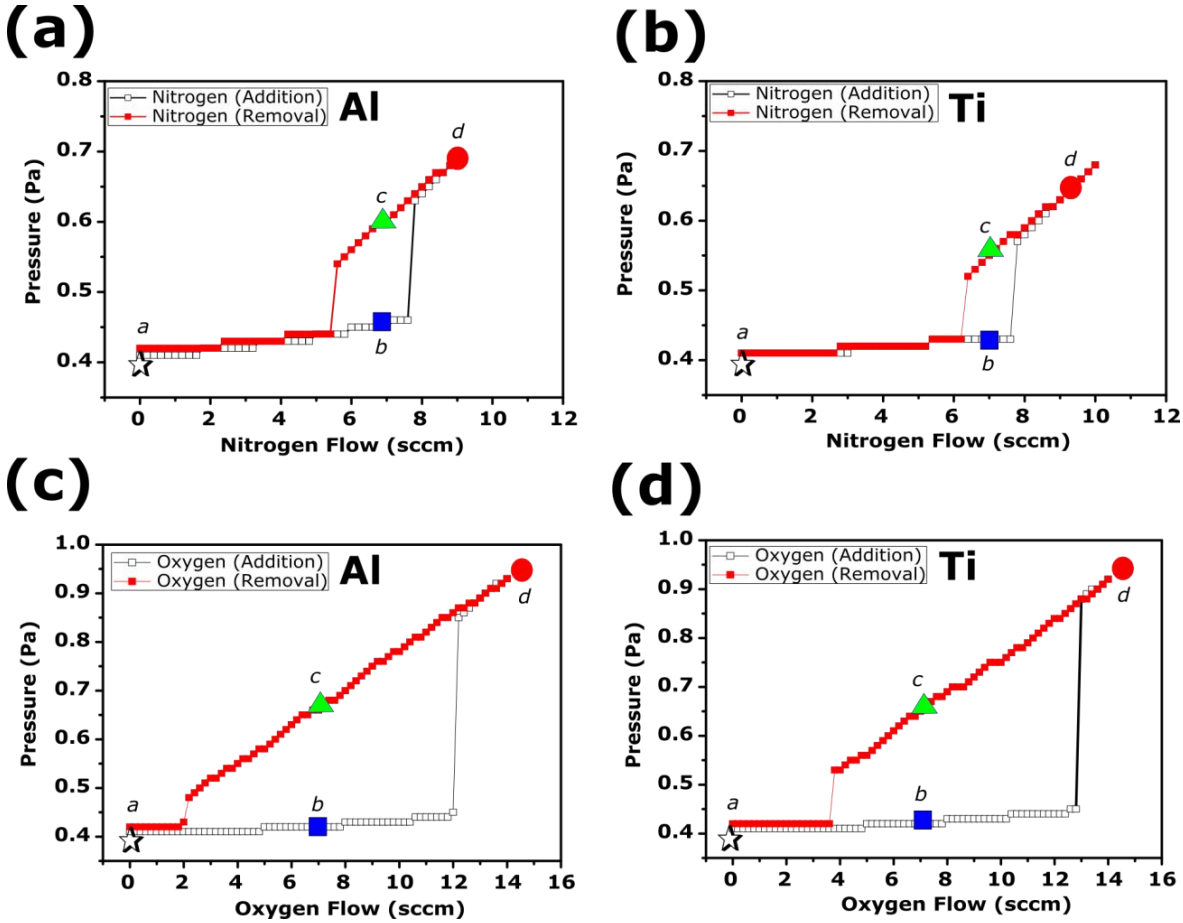

Figure 31: Hysteresis curves of reactive gas flow rate and chamber pressure for Al and Ti targets during reactive sputtering. (a) For Al target reactively sputtered in the presence of N_2 (Al+N_2), the chamber pressure increases in the poisoning mode. (b) For Ti+N_2, the chamber pressure increases after poisoning of the target surface. (c) For Al target reactively sputtered in the presence of O_2 (Al+O_2), no significant change in pressure in the metallic mode due to higher reactivity of O_2 with Al. However, the chamber pressure increases in the poisoning mode. (d) For Ti+O_2, the chamber pressure remains constant in the metallic mode and increases in the poisoning mode.

Nitrogen and Aluminum: For Al, the discharge voltage drops with increasing flow of N_2 as shown in figure 30(a). The AlN compound formation on the target surface gradually decreases the voltage due to higher secondary electron emission from the target surface [68]. AlN with a large band gap (6.2 eV) has a higher secondary electron emission yield as compared to that of pure Al. At complete poisoning, there is a sudden decrease in the discharge voltage. With increasing N_2 flow, the target surface was shifted to the poisoned mode at 7.8 sccm, and was shifted back to the metallic mode at 5.6 sccm of N_2 flow during the decreasing flow cycle of reactive gas. Figure 31(a) shows the chamber pressure at different flow rate of N_2. In the metallic mode, the reactive gas is consumed to form AlN and there is no significant change in the chamber pressure. However, in the poisoning mode, sputter voltage decreases and the chamber pressure increases. As shown by figure 31(a), the chamber pressure was 0.41, 0.45, 0.60 and 0.69 Pa at points *a*, *b*, *c* and *d*, respectively.

Nitrogen and Titanium: In figure 30(b), for a TiN layer on a Ti target, the discharge voltage increases with increasing nitrogen flow. Like other transition metal nitrides, TiN exhibits dominant metal-metal interactions with higher electrical conductivity. With an intermediate band gap (3.4 eV), TiN can be considered as a conductive ceramic. This property causes a lower yield of secondary electrons from the target surface. The transition between metallic and poisoned mode of sputtering was observed at 7.8 and 6.2 sccm during increasing and decreasing N_2 flow. As shown by figure 31(b), the corresponding chamber pressures at points *a*, *b*, *c* and *d* were observed to be 0.41, 0.43, 0.55 and 0.63 Pa, respectively. A small hysteresis width for nitrides shows that there is a rather low reactivity of Al and Ti with N_2 compared to O_2. As the nitrides do not lose nitrogen with ion bombardment, the secondary electron emission yield mainly depends on their electronic properties.

Oxygen and Aluminum: Generally, for metal oxides, the ion-induced secondary electron yield is higher than that of the pure metals. For Aluminum Oxide (Al_2O_3), initially, the O_2 is chemisorbed on the target surface and there is not any significant change in discharge voltage as shown in figure 30(c). However, after a certain critical point, the target surface is oxidized. After oxidation of the Al surface, the secondary electron emission yield from the oxide layer increases strongly and the discharge voltage drops in the order of 100 volts in complete poisoning state [69]. The oxide layer does not reduce by the ion bombardment and the electronic properties are not affected. The change in

sputtering mode was observed at 12.2 and 2.0 sccm of O_2 during the increasing and decreasing flow cycles, respectively. Figure 31(c) shows the hysteresis curve for chamber pressure at different flow rate of O_2. In the metallic mode, until 12 sccm of O_2 flow rate there is no significant change in the chamber pressure. However, in the poisoning mode the chamber pressure significantly increases. The chamber pressure at points *a*, *b*, *c* and *d* were measured as 0.41, 0.42, 0.66 and 0.93 Pa, respectively, as shown by figure 31(c).

Oxygen and Titanium: For certain materials, the oxidized target surfaces exhibit lower electron emission yields [70]. For such metals, like Ti, the oxides are reduced by the ion bombardment and their electronic properties are affected. The oxide layer loses oxygen due to the Ar ion bombardment and a sub-oxide layer is formed on the target surface. The formation of sub-oxide layer reduces the ion-induced secondary electron emission yield [67]. For Titanium Oxide (TiO_2) in figure 30(d), the secondary electron yield decreases and there is an increase in discharge voltage with higher O_2 content. With increasing O_2 flow, the target surface was shifted to poisoned mode at 13.0 sccm and shifted back to metallic mode at 3.8 sccm of O_2 flow. In the pressure hysteresis curve as shown by figure 31(d), the corresponding pressures at points *a*, *b*, *c* and *d* were measured as 0.41, 0.42, 0.65 and 0.93 Pa, respectively. The hysteresis width for both Al_2O_3 and TiO_2 is more pronounced and the oxidation layer was removed at a lower oxygen flow rate during the decreasing cycle. For oxides, due to the removal of oxygen and formation of sub-oxides, the secondary electron yield can be understood by the properties of the oxide layers (oxide or a sub-oxide).

5.2 Reflection of a laser beam from the poisoned target surface

According to our assumption, the deviation of the reflected beam along z-axis is only influenced by the tilt angles of a facet but not by the vertical position of the facet. For the characterization of the target surface in the poisoning mode, the targets were sputtered at four different flow rates of reactive gas as 0 sccm (metallic mode), 7 sccm in metallic mode (transition region metallic mode), 7 sccm in poisoned mode (transition region poisoned mode) and at complete poisoning mode (poisoned mode, 9 sccm for N_2 and 16 sccm for O_2) as previously mentioned. The respective hysteresis curves are shown in figure 30, and the different poisoning states are marked by four points *a*, *b*, *c* and *d*, respectively.

Figure 32 shows the reflected intensity distribution from a poisoned target surface.

Figure 32(a) shows the optical image of the reflected laser beam on the screen for an Al target in the poisoned mode. The intensity profile was measured along the z-axis starting from zero to 1500 pixels (one pixel corresponds to 20 µm). The maximum intensity is observed at the centre of the image represented by 0. At the scan length of 1500 pixels (30 mm), the reflected intensity decreases to a minimum value around zero. Figure 32(b) shows the grey scale intensity values profile (average over 10 line scans) for 1500 pixels along the z-axis for metallic and poisoning modes for Al. Higher values of the reflected intensity beam were observed from the poisoned target surfaces of the Al target after poisoning with both oxide and nitride compound as compared to that of a non-poisoned surface. A plausible explanation for this high intensity could be a lower surface roughness of the poisoned target. In the poisoned condition the surface became smooth due to deposition of the compound layers (see also figure 16).

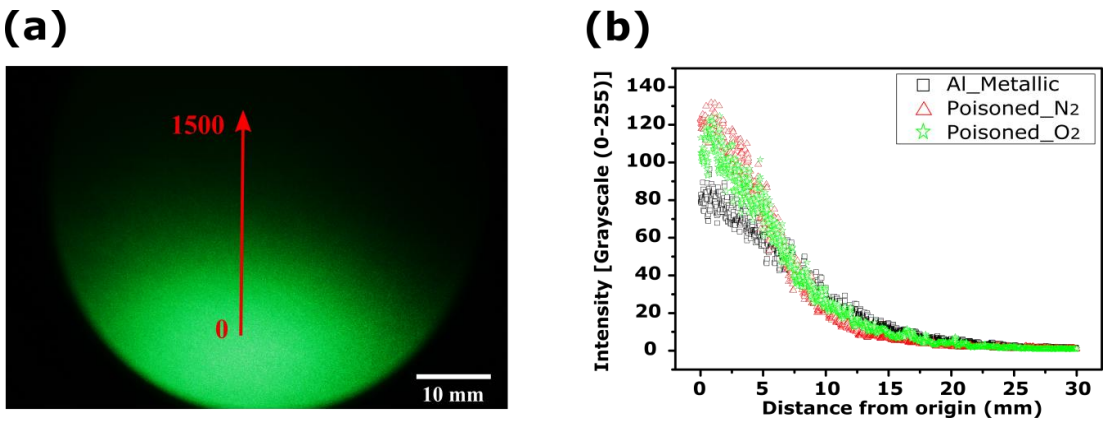

Figure 32: Reflected intensity distribution from a target surface (a) Optical image of reflected laser beam on the screen for Al target in the poisoned mode. (b) Intensity profile, measured from the images, for a scan length of 30 mm (red line in (a)) for Al target in metallic and poisoned modes.

The roughness of the target surface was also measured by a profilometer in both metallic and poisoned modes after sputtering. Figure 33 shows the profilometer scans for Al and Ti target surfaces. Figure 33(a) shows the height profile of an Al target after sputtering in the metallic mode. After poisoning with a nitride layer (60 min sputtering in poisoned mode), the height profile of the Al target is shown in figure 33(b). Figure 33(c) and 33(d), shows the height profiles of the Ti target surface after 60 min sputtering in metallic and poisoned mode, respectively. A similar trend in target roughness was observed. Form these results it was concluded that reflectivity can be considered as an indicator for roughness and, consequently for the degree of poisoning.

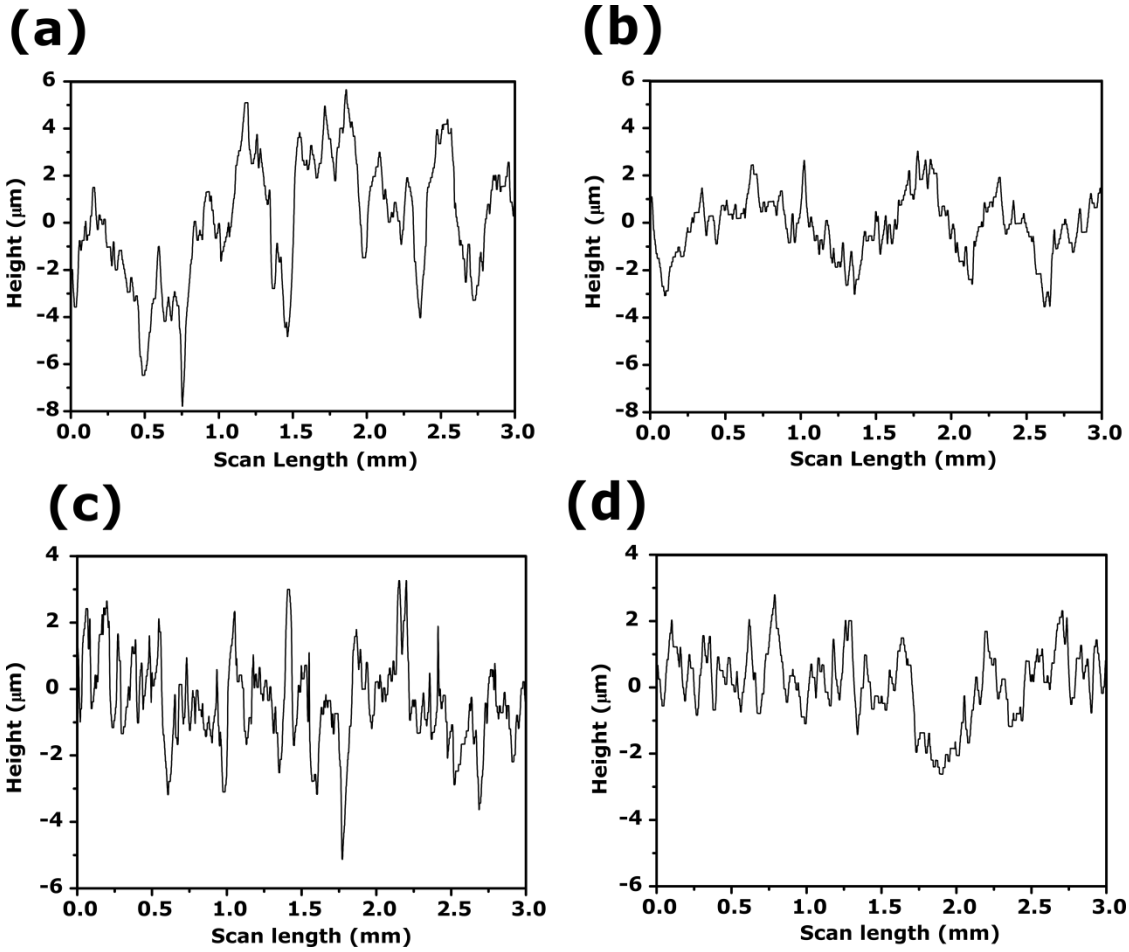

Figure 33: Profilometer scans for a typical metallic and poisoned target surface. (a) Height profile of an Al target surface after sputtering in non-reactive mode for 60 min. (b) Height profile of the Al target surface after poisoning with a nitride layer (60 min poisoning time in poisoned mode). (c) Height profile of a Ti target surface after 60 min of sputtering in non-reactive mode. (d) Height profile of the Ti target surface after 60 min sputtering in poisoned mode.

5.3 Roughness evolution

As previously mentioned, the roughness evolution during sputtering is a well-known phenomenon[71]. During sputtering the formation of different surface structures (ridges, facets and edges) alters the target surface roughness. The non-uniform discharge across the target surface leads to variations in erosion rate [72]. The preferential sputtering from differently oriented grains also increases the roughness [73]. In polycrystalline materials, however, the role of grain boundaries may become more prominent for the roughness evolution. In reactive sputtering, after the formation of compound, the grain boundary etching may slow down. In certain cases, if grain boundaries are earlier chemically saturated than the facets, this chemical effect could even make the grain boundary etching

slower than the etching of the crystalline facets. Regardless of the detailed erosion mechanism, as indicated above, the change in surface roughness will be attributed to the degree of poisoning on the target surface.

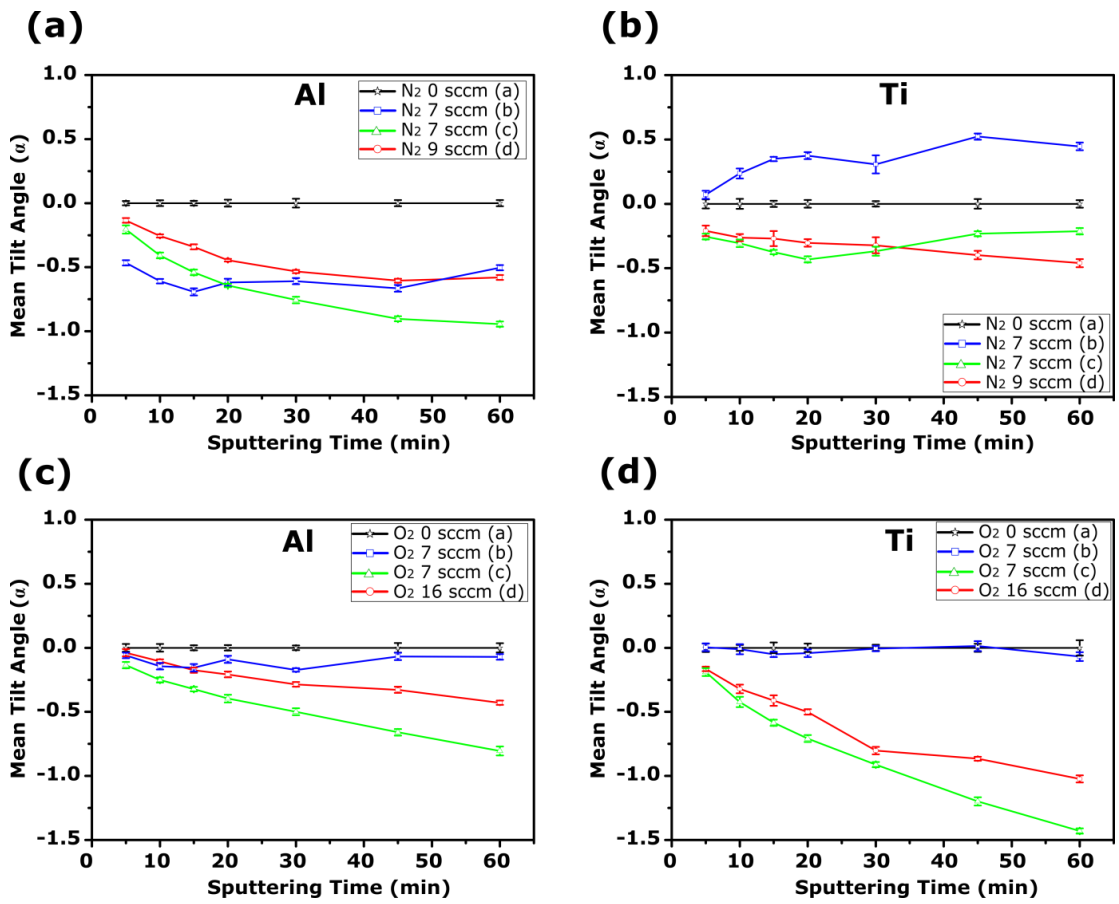

Figure 34: Mean tilt angles calculated from the reflected intensity distribution of a laser beam form a target (a) Mean tilt angle for the Al target surface before and after poisoned with a nitride layer. (b) The mean tilt angle of Ti target surface at different poisoning levels. (c) Mean tilt angle for the Al target surface before and after poisoned with an oxide layer. A deceasing trend in mean tilt angle for poisoned modes both at 7 and 16 sccm of O_2 flow rate is observed with formation of an oxide layer on the Al target surface. (d) The mean tilt angle of the Ti Target surface is constant at transition region metallic mode. A gradual decrease is observed in mean tilt angle after poisoned with an oxide layer both at 7 and 16 sccm of O_2 flow rates.

Figure 34 shows the mean tilt angles calculated from the reflected intensity distribution (using eq. 10 as described in section 4.1) between zero and higher flow rates of the reactive gas in both metallic and poisoned modes up to 60 minutes of sputtering. These mean tilt angles correspond to the roughness of the target surface under certain sputtering

conditions. The mean tilt angles measured in the non-reactive (metallic) mode were taken as a reference and the variation in mean tilt angle after sputtering was calculated. In the metallic mode, generally there is no significant formation of compound layer on the target surface, so the mean tilt angle either remains constant or increases after prolonged sputtering. However in poisoned mode, the mean tilt angles are decreased due to the formation of the compound layer. Overall the lowest values of mean tilt angles are obtained at 7 sccm in the transition region poisoned mode, as represented by point *c* in the figure 30. In the following the different combinations of reactive gas and metal are discussed in detail.

Nitrogen and Aluminum: Figure 34(a) shows the mean tilt angles of the Al target surface at 0 sccm (metallic mode), 7 sccm (transition region metallic mode), 7 sccm (transition region poisoned mode) and 9 sccm (poisoned mode) of N_2 flow rates. In transition region metallic mode at 7 sccm of N_2, there is not any significant change in the mean tilt angle. However, in poisoned modes, a gradual decrease in the mean tilt angle was observed with longer sputtering time.

Nitrogen and Titanium: For a Ti target poisoned with nitride, as shown in figure 34(b), an increase in roughness was observed at 7 sccm of N_2 in transition region metallic mode. No significant change was observed in the mean tilt angle at transition region poisoning mode at 7 sccm of N_2 flow rate. In this case, during sputter cleaning, an increase in mean tilt angle was observed, which consequently leads to the observed slight increase in mean tilt angle after 45 min of poisoning (Fig. 32b, green line). On the other hand, a decreasing trend in roughness was found in poisoned mode at 9 sccm of N_2. Longer sputtering in poisoning mode might increase the thickness of the nitride layer, which ultimately decreases the roughness of the target surface. All tilt angles in poisoned modes (in transition region poisoned and poisoned) are smaller than in metallic mode even right after starting reactive deposition (see figure 34 (b) red and green line).

Oxygen and Aluminum: Similarly, the mean tilt angles were measured for both Al and Ti target surfaces after reactive sputtering with O_2. Figure 34(c) shows the mean tilt angle of the Al target surface calculated from reflected intensity patterns for both in metallic and poisoned modes after reactive sputtering up to 60 min. In transition region metallic mode, the mean tilt angle remains constant with increasing sputtering time. However, after poisoning with the oxide layer on the target surface the roughness of the sputtering target surface decreases. The decrease in mean tilt angle of the target surface

was more prominent at 7 sccm of O_2 in the transition region poisoned mode.

Oxygen and Titanium: A similar behavior was observed for the Ti target after poisoning with an oxide layer. Figure 34(d) shows the mean tilt angle of the reflected intensity from the Ti target after poisoning with an oxide layer. A decreasing trend in mean tilt angle was observed in poisoning modes (in transition region poisoned and poisoned mode) both at 7 and 16 sccm of O_2 flow rates. The distinct surface morphologies of Al and Ti show different values of the mean tilt angle. However, for both cases the poisoning layer decreases the mean tilt angle of the target surface.

The target surface was also examined by the scanning electron microscope (SEM). Figure 35 shows the SEM images of the Al and Ti targets before and after the formation of nitride and oxide on the target surface at complete poisoning mode (at point d in figure 30). Comparatively, a smooth target surface was observed after poisoning. As validated by reflectometry and profilometry (see figure 33), figure 35(a) shows the morphological image of an Al target surface in metallic mode. A rough and porous-like structure was observed after sputtering in metallic mode. Figure 35(b) shows the morphological image of an Al target surface poisoned with AlN. After the formation of the AlN layer, the surface became smooth with fewer holes. Figure 35(c) shows the morphological image of the Al target surface after formation of an oxide (Al_2O_3) layer on the surface. Small particles were observed on the surface and the porous structure was filled by compound layer. Figure 35(d) shows the morphological image of the Ti target surface in metallic mode having a rough, rocky looking, structure. After poisoning with nitride layer (TiN), it became comparatively smother as shown in figure 35(e). Figure 35(f) shows the morphological image of a Ti target poisoned with oxide layer (TiO_2). After the formation of a thick oxide layer the target surface looks flat and relatively featureless.

Energy dispersive spectroscopy (EDS) was also used to determine the elemental composition of the poisoned target surface. However, the EDS analysis does not show any prominent difference in the composition of the target surface before and after the poisoning due to very thin compound layers. The roughness profile of the target surface was also determined by a mechanical profilometer. This roughness evolution was in good agreement with analogous measurements taken from the profilometer. The RMS roughness of the Al in metallic state was measured as 1.39 ±0.04 µm. After poisoning with nitrogen (AlN) and oxygen (Al_2O_3), the RMS roughness values were reduced to 1.26 ± 0.08 µm and 1.06 ± 0.06 µm, respectively. A similar trend of decreasing roughness was observed for Ti

where the metallic mode RMS roughness, 1.45 ± 0.07 µm, was decreased to the value of 1.30 ± 0.04 µm and 0.97 ± 0.03 µm after the formation of a nitride (TiN) and oxide (TiO_2) layers on the target surface, respectively. The RMS roughness values of typical virgin (polished) Al and Ti targets were also measured as 0.56 ± 0.03 µm and 0.38 ± 0.02 µm, respectively.

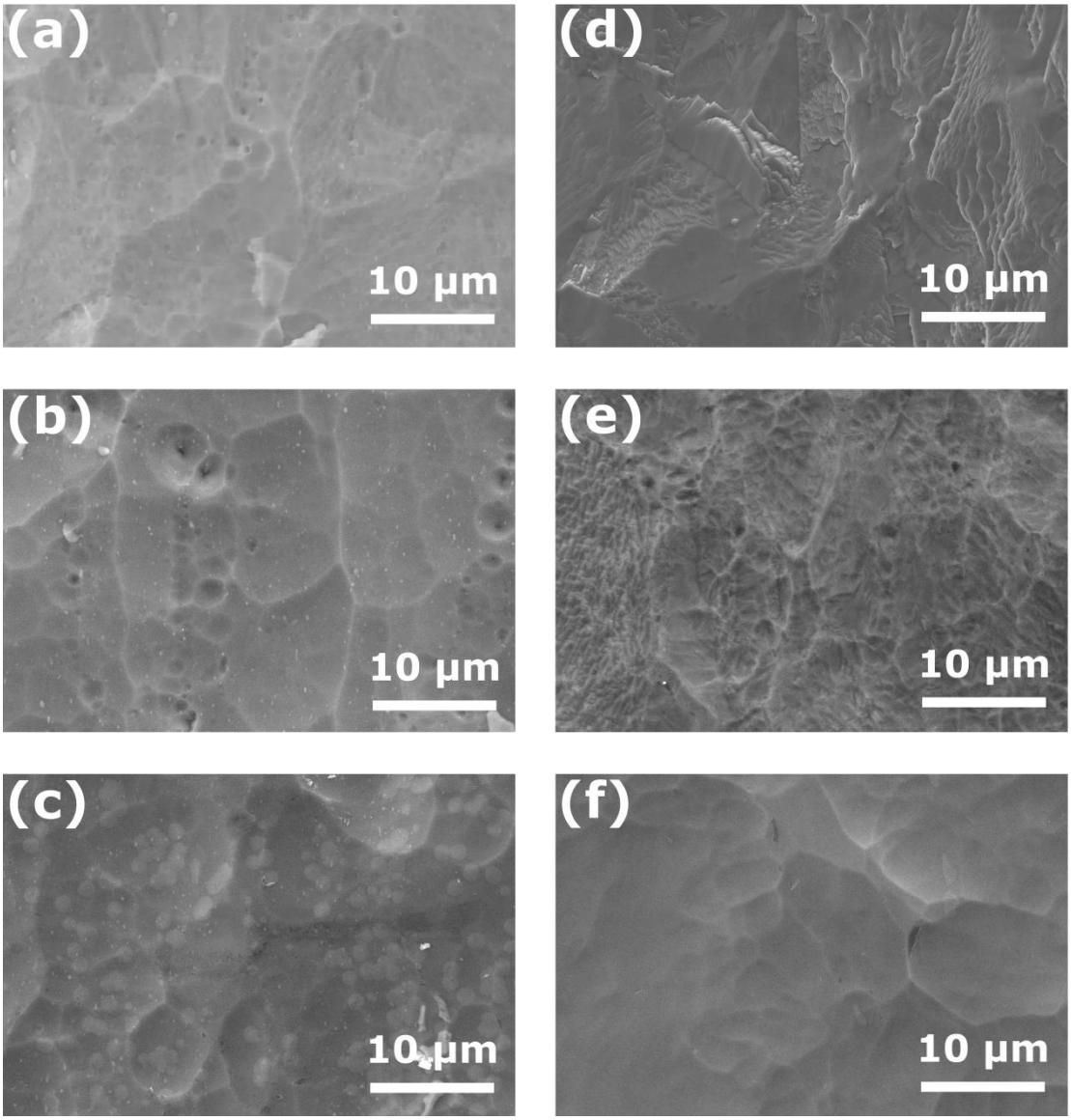

Figure 35: SEM images of target surface. (a) Morphological image of Al target surface in metallic mode. (b) Morphological image of Al target surface poisoned with AlN. (c) Morphological image of Al target surface after formation of oxide (Al_2O_3) layer. (d) Morphological image of Ti target surface in metallic mode. (e) Morphological image of Ti target poisoned with nitride layer (TiN). (f) Morphological image of Ti target surface poisoned with oxide layer (TiO_2).

To conclude this section on roughness evolution it can be stated that in reactive sputtering, the reactive gas can interact with the target surface in different ways [48, 74]. The reactive gas molecules are chemisorbed on the target surface and also get implanted into the target surface [34, 35]. Initially, at low reactive gas pressure, chemisorption is more prominent. However, in the poisoning mode at decreased sputter yield and higher flow rate of reactive gas, the fraction of implanted reactive ions increases. Finally, these implanted ions chemically react with the target surface to form the compound. Although, this compound formation considerably reduces the sputter yield and the erosion of the target changes the surface composition, probably some ions are implanted more deeply into the target and erosion of the target can move some of the underlying compound layers to the target surface. Therefore the composition of the target surface becomes more complex. After a certain poisoning time, the target surface may contain non-reacted target material, compound formed by chemisorption and chemically reacted compound. The further erosion and re-deposition of these materials could change the morphology of the target surface. In addition, these processes are highly dynamic which is reflected by the fact that the target surface is still changing even after 60 min of reactive sputtering as visible in figure 34.

5.4 Poisoning and deposition rate

As considering deposition rate, the ongoing growth of the compound layer thickness may lead to a reduction in deposition rate as the following paragraph shows. Al and Ti targets were reactively sputtered with different flow rates of N_2 and O_2 as represented by points a, *b*, *c* and *d* in figure 30. Table 1 shows the deposition rate at two different poisoning levels (after 10 and 60 min of poisoning, for details of deposition procedure, see section 3.2). In transition region metallic mode, at point *b*, there is not any significant change in deposition rate as also suggested by the mean tilt angles in the metallic modes. However, in poisoning modes, at points *c* (transition region poisoned mode) and *d* (poisoned mode), an overall decrease in deposition rate was observed at longer sputtering time. For AlN, at 7 sccm and 9 sccm of N_2 flow rate (point c, d), the deposition rate was decreased by 9 %, and 8 %, respectively. No change was observed for point *b*. For TiN, no significant change was observed in deposition rate at all poisoning modes. For Al_2O_3, the deposition rate was decreased by 20 and 16 % at 7 and 16 sccm of O_2 flow rate (points *c* and *d*), respectively. No change was observed for point *b*. For TiO_2, the deposition rate was

decreased by 4 and 15 % after poisoning at 7 and 16 sccm of O_2 flow rate (points *c* and *d*), respectively. Again no change was observed for point *b*. As shown in figure 30(c & d), there is not any significant difference in discharge voltage at point *a* and *b*, so in non-reactive mode, for both Al and Ti, the deposition rates were very close to those for Al_2O_3 and TiO_2, at 7 sccm in the metallic mode, respectively.

In the poisoning modes, the formation of compound layer changes the collision cascades produced by the impinging ions. Atoms emerging from the metal have to go through the compound layer and deposition rate decreases. As this compound layer is formed even after short poisoning time it may influence the deposition rate immediately. In addition to the thickness of the compound layer, the deposition rates are also influenced by many interconnected parameters like target material, surface morphology and composition of the compound layer. During the roughness evolution, the effect of roughness on the material flux towards the substrate is also material-dependent and different composition of the compound layer exhibits different erosion rates [3]. Nevertheless, the thickness of the compound layer and the deposition rate do not have to be directly proportional because of the complex transport mechanism involved in the ejection of atoms from the poisoned target surface.

Table 1.

The deposition rates after 10 and 60 minutes of sputtering in transition region metallic, transition region poisoned and fully poisoned modes for Al and Ti targets

Compound material	**Flow rate of reactive gas (sccm)**	**Deposition rate (nm/min)**	
		after 10 min of poisoning	**after 60 min of poisoning**
Al	0 sccm of reactive gas (at point a)	203	
Ti	0 sccm of reactive gas (at point a)	106	
AlN	7 sccm of N_2 (at point *b*)	97	96
AlN	7 sccm of N_2 (at point *c*)	12.9	11.8
AlN	9 sccm of N_2 (at point *d*)	10.4	9.6
TiN	7 sccm of N_2 (at point *b*)	97	96
TiN	7 sccm of N_2 (at point *c*)	36	37
TiN	9 sccm of N_2 (at point *d*)	37	36
Al_2O_3	7 sccm of O_2 (at point *b*)	211	216
Al_2O_3	7 sccm of O_2 (at point *c*)	11.9	9.5
Al_2O_3	16 sccm of O_2 (at point *d*)	10.7	8.9
TiO_2	7 sccm of O_2 (at point *b*)	98	99
TiO_2	7 sccm of O_2 (at point *c*)	9.2	8.9
TiO_2	16 sccm of O_2 (at point *d*)	9.4	8.0

5.5 De-poisoning measurement

The sputter cleaning method can be utilized for the assessment of the properties of the poisoned layer on the target surface [15, 70, 75]. As a proof of concept, the de-poisoning time was measured for both Al and Ti targets at different poisoning levels. At a current of 0.5 A, the voltage measurements at different flow rates of reactive gas after different poisoning time are shown in figure 36. The targets surfaces were poisoned at 5 A

sputtering current but the de-poisoning time was measured at 0.5 A current. Actually, at 5 A de-poisoning current, the target surface instantly transited to the metallic mode and it was not possible to measure the de-poisoning time. So, for the measurement of de-poisoning time, the targets were sputter cleaned in the absence of reactive gas at 0.5 A sputtering current (a discharge current density of 0.004 Acm^{-2}). The de-poisoning time is measured after 10 and 60 minutes of reactive sputtering in transition metallic, transition poisoned and fully poisoning modes at points *b*, *c* and *d* of the hysteresis curves (for measurement procedure, see section 3.2).

For nitrides: Figure 36(a) shows the rate of change from poisoned to the metallic mode after poisoning with a nitride layer on the Al target surface. An abrupt change in voltage is observed at transition region metallic mode (point *b*) after 10 and 60 min minutes of poisoning. For all other poisoning modes, the change in discharge voltage is rather slow and it took about 15 s to reach the metallic state. In all cases, there is not any significant difference in de-poisoning time between 10 and 60 minutes of poisoning at both, 7 and 9 sccm of N_2 flow rates, in poisoning modes. The de-poisoning time for a Ti target poisoned with nitride layer is shown in figure 36(b). No significant change in de-poisoning time is observed for both transition region metallic and poisoning modes at 7 sccm of N_2 (points *b* and *c*). The target surface was shifted to metallic state in less than 10 s. However, at 9 sccm in poisoning mode (point *d*), a longer de-poisoning time after 60 min of poisoning is observed. Similar trends can be observed in mean tilt angle and change in deposition rates for TiN.

For oxides: In figure 36(c), the de-poisoning time of an Al target with oxide layer is shown. Similarly, at transition region metallic mode (point *b*), the same behavior in discharge voltage is observed after 10 and 60 minutes of poisoning. Nevertheless, an apparent difference is observed in de-poisoning time for poisoned modes (point *c* and *d*) after different poisoning times of 10 and 60 min. The identical tendency can be seen in both, mean tilt angle measurements and deposition rates at different poisoning levels. The de-poisoning time for a Ti target, poisoned with oxide layer is shown in figure 36(d). In transition region metallic mode (point *b*), no significant difference is observed in de-poisoning time at 10 and 60 minutes of poisoning as expected.

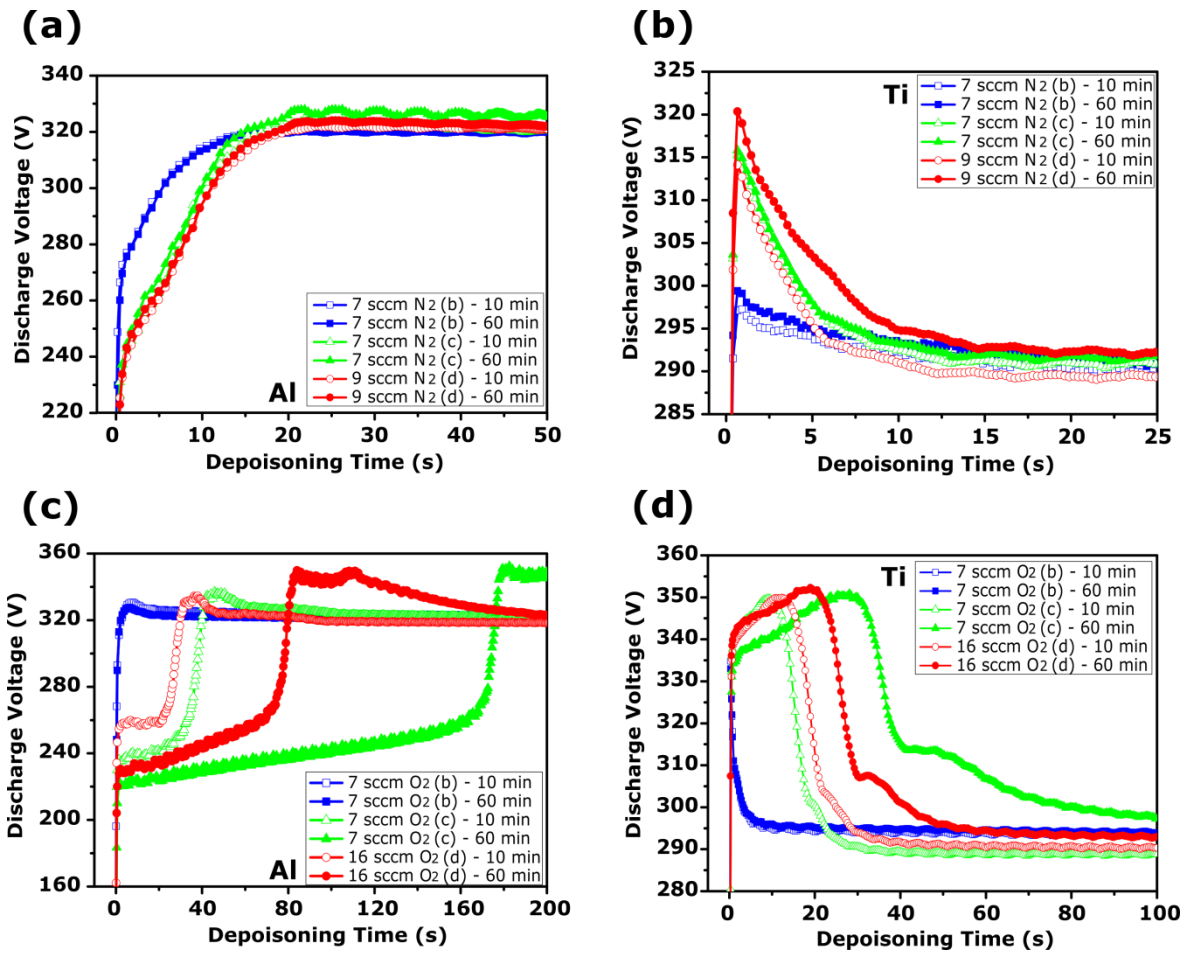

Figure 36: The de-poisoning time after 10 and 60 minutes of poisoning at different flow rates of reactive gases for Al and Ti targets. (a) Change of discharge voltage from poisoned to the metallic mode of Al target surface after poisoning with a nitride layer. No significant difference in de-poisoning time at both metallic (point b) and poisoned modes (point c & d) between 10 and 60 minutes of poisoning. (b) The de-poisoning time for Ti target poisoned with nitride layer at different flow rate of N_2. A difference in de-poisoning time is observed at 9 sccm (point d) of N_2 after different poisoning times. (c) De-poisoning time of Al target poisoned with an oxide layer. In poisoning modes (point c & d), the longer poisoning time accumulates a thicker oxide layer on the target surface. (d) The de-poisoning of an oxide layer from a poisoned Ti target surface. The de-poisoning time increases with increasing sputtering time in poisoning modes (point c & d) as expected.

In transition region poisoning mode, at 7 sccm of O_2 flow rate (point *c*), the difference in de-poisoning time is more prominent between 10 and 60 minutes of poisoning. Also, at 16 sccm of O_2 (point *d*), the target surface is more poisoned after 60 minutes of poisoning as predicted by the mean tilt angle measurements. The chemisorption of the reactive gases could also influence the cleaning time. As Ti getters oxygen more efficiently, an overall shorter cleaning time is observed for TiO_2 as compared to Al_2O_3, as for instance the chamber walls help in the removal of reactive gas.

For nitrides, it generally takes shorter time to remove the poisoning layer from the target surface. However, for oxides a comparatively longer time is required for the transition to the metallic mode. In addition, there is a significant dependence of the de-poisoning time for oxides on the length of sputtering in poisoned modes at point *c* and *d*. It takes significantly longer to de-poison a target operated under O_2 containing atmosphere for 60 min than for one operated for 10 min. Also the re-deposition of sputtered material on the eroded surface may influence de-poisoning time. In the present case, however, the largest part of the cylindrical target was eroded during sputtering and the roughness was always measured within the uniformly eroded region of the target. The surface of the eroded target was also examined by an optical microscope, and no significant racetracks were observed. Coatings on the non-eroded zone of the target (a few mm in length) may influence the cleaning time of the poisoned target but this zone amounts only to approximately 10 % of the total target surface, so this effect is likely to be minor. Although poisoning involves many interconnected mechanisms at the target surface and subsurface, the results presented here finally suggest that there is a direct correlation between target roughness and the state of poisoning.

6. Characterization of Aluminium and Titanium nitride films prepared by sputtering under different target poisoning conditions[3]

The previous section has shown that target poisoning is a highly dynamic process which is not finished at all even after sputtering times of up to 1 hour. Therefore, it has to be expected that the ongoing changes of the target surface will influence the properties of the films deposited after different poisoning time. Section 5.4 has shown that the surface morphology due to varied thickness and composition of the compound layer is influenced by poisoning. In this section the influence of poisoning on morphological and structural properties of the sputter deposited nitride films will be addressed. Magnetron sputtering is a well-established industrial technique for deposition of metallic films and compounds. For deposition of compounds, often an additional reactive gas is introduced and the sputtering process transforms to reactive sputtering. The reactive sputtering of Al and Ti in the presence of N_2 is a widely used technique to deposit AlN and TiN films, respectively. These nitride coatings have been extensively used in a variety of applications due to their excellent properties. AlN, a wide band gap ceramic exhibits high thermal conductivity[20] and is used in many applications due to its electro acoustic properties [21], excellent piezoelectricity [22] and optical properties [23]. On the other hand, TiN is a conductive ceramic with high thermal and chemical stability. It is extensively used for diffusion barriers [24], wear-resistant coatings [25], decorative coatings [26] and biocompatible implants [27].

The properties of these nitrides can be tailored by changing the sputtering conditions such as reactive gas partial pressure [28], Ar/N_2 ratio [29], substrate temperature[30], substrate bias voltage [31] and sputtering power [32]. The variation in flow rate of the reactive gases also gives a good control over stoichiometry of the deposited films. However, at a certain flow rate of the reactive gas, the target is poisoned by the compound formation on the target surface. Due to different electronic properties of the compounds, the discharge voltage is significantly changed (increased or decreased) in the poisoning mode. As a consequence, the sputter yield and the corresponding deposition rates are decreased [33]. Target poisoning is a complex mechanism and the reactive gas molecules are not only chemisorbed on the target surface but also get implanted into the target surface [34, 35].

[3]The contents of this chapter are partially submitted to *J. Vac. Sci. Technol. A* (under review)

After a certain poisoning time, the target surface may contain non-reacted target material, compound formed by chemisorption and chemically reacted compound. The target surface elements with different composition exhibit different surface binding energies and so the energy of the sputtered particles are influenced by their origin[36]. The increased content of the compound on the target surface influences the energy distribution function of the sputtered particles. Although particle fluxes and energy distribution of the sputtered atoms have been investigated in metallic and poisoning mode [37, 38], the effect of short and long-term poisoning on the deposited films has not been addressed.

Herein, we present an experimental approach to study the effect of prolonged poisoning on the properties of the deposited films. Al and Ti targets were reactively sputtered in poisoning mode and the target surfaces were poisoned with nitride. The sputtering current was kept constant at 5 A, and the substrate holder was grounded to avoid self-biasing effects. The AlN and TiN films were deposited on natively oxidized Si wafers during the first 10 min of sputtering in the poisoned mode and after 60 min of poisoning, respectively. The influence of short and long-term poisoning was investigated by measuring the surface morphology and structural properties of the films by AFM, SEM, XRD, and XPS. A change in micro structure, preferred crystallographic orientations and elemental composition of the deposited films was observed between short and prolonged poisoning time. Therefore, the different levels of target poisoning could control the properties of the sputtered deposited films.

6.1 Poisoning and hysteresis behaviour

During the sputtering process, the reactive gas reacts with the sputtered atoms and compound is formed at the substrate (including chamber walls) and the target surface. Reactive sputtering is not a linear process and at different flow rates of reactive gases it exhibits hysteresis effects. The partial pressure of reactive gas is a key parameter in describing the sputtering behavior. To understand the reactive sputtering process, figure 37 shows a typical pressure and discharge voltage curve at different flow rate of N_2 for Al and Ti targets. When the discharge power is off, the chamber pressure gradually increases with increasing flow rate of the reactive gas. However, in the presence of discharge power, initially, all the reactive gas is consumed by reacting with the metal particles to form a compound.

There is not any significant increase in the chamber pressure and the target operates in metallic mode as shown in figure 37(a) and 37(b). The increase in the reactive gas flow not only increases the compound formation on the substrate, it also increases the area of the compound layer on the target. With decreasing erosion rate due to compound formation, the reactive gas molecules find less metal atoms to react and eventually there is a change in chamber pressure as shown in figure 37(a) and 37(b) for AlN and TiN, respectively. The further increase results in a dramatic increase in the chamber pressure and a corresponding change in discharge voltage at 8 sccm of the N_2 flow as shown in figure 37. Consequently, there is a transition of the target surface from metallic to poisoned state. The variation of voltage (decrease or increase) in the transition mode depends on the properties of the compound layer.

For Al, as shown in figure 37(c), the formation of AlN compound on the target surface gradually decreases the voltage due to higher secondary electron emission from the poisoned target surface[68]. AlN, a wide band gap (6.2 eV) ceramic has a higher secondary electron emission yield as compared to that of pure metallic Al. In figure 37(d), for a Ti target, the discharge voltage increases in the poisoning mode with decreased emission of secondary electrons from the TiN compound. TiN, a transition metal nitride with an intermediate band gap (3.4 eV), exhibits a lower yield of secondary electrons from the target surface.

Different target materials getter different amounts of reactive gas during the sputtering process as shown by the change in reactive gas pressure ($\triangle P$) in figure 37(a & b). Ti is a well-known gettering material for oxygen, nitrogen, carbon dioxide and hydrogen [76]. The higher value of $\triangle P$ for Ti corresponds to the more effective utilization of reactive gas to form a compound. Al getters less reactive gas and a smaller value of $\triangle P$ is observed. The target surface can again be switched to the metallic state by decreasing the flow rate of reactive gas. However, during the decrease of reactive gas flow rate, transition is not observed at the same flow rate and the well-known hysteresis effect is observed [66]. Pressure and discharge voltage do not show the same behavior during increasing and decreasing flow rate of the reactive gas. Different parameters influence the hysteresis effect, like target material, type of reactive gas, pumping speed, target to substrate distance, ion current and size of the target [33]. In the region from A to B as shown in figure 37(c & d), the deposition rate is very high and the composition of the deposited film is sub-stoichiometric. Increasing N_2 flow leads towards more stoichiometric coatings. However,

the reactive gas flow region close to point B is unstable and could shift to the poisoning mode. In the poisoned region, between points C and D, sputter yield decreases and the film composition becomes stoichiometric. The target poisoning also affects the angular distribution of sputtered atoms, as well as structural, electrical and optical properties of the deposited layers.

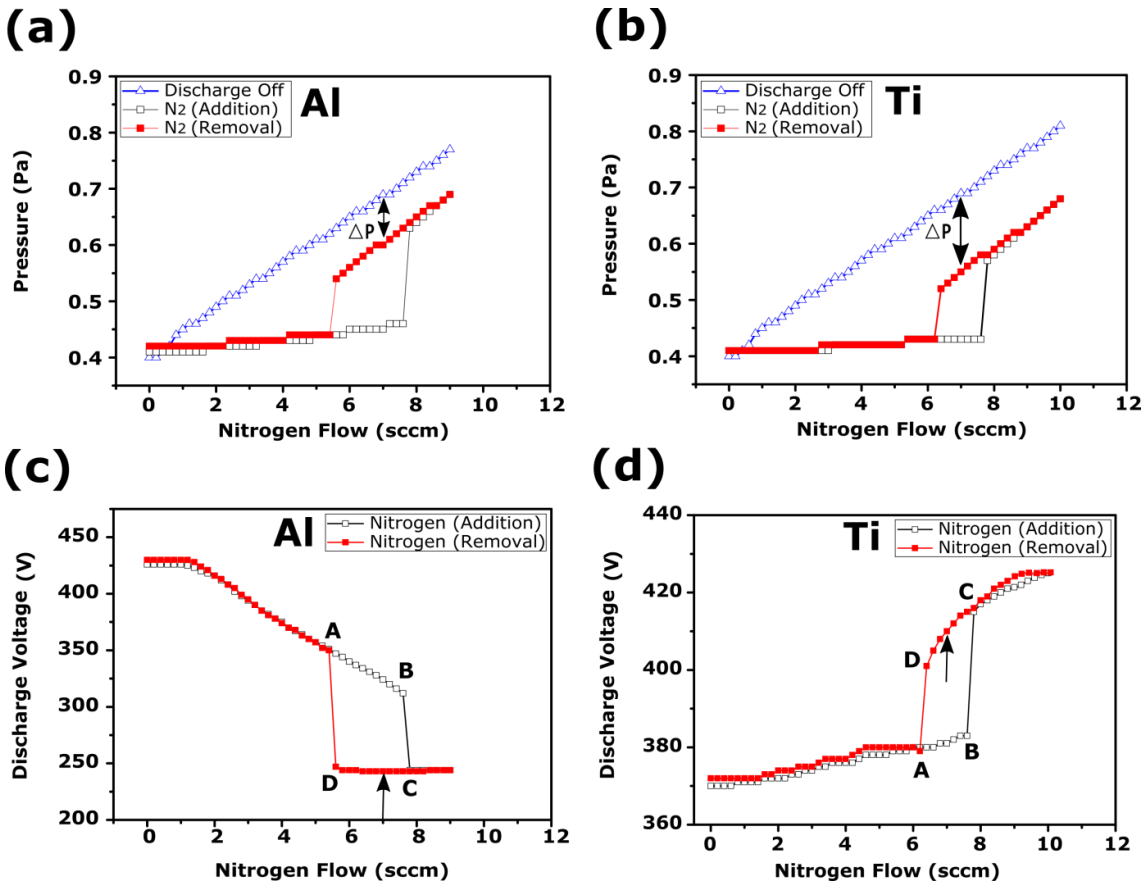

Figure 37: Hysteresis curves of reactive gas flow rate for pressure and discharge voltage for Al and Ti targets during reactive sputtering. (a) For Al, in metallic mode, until 7.8 sccm of N_2 flow, the reactive gas is gettered by the sputtered particles and in the poisoning mode the pressure increases due to the formation of compound layer on the target surface. (b) For Ti, there is not any significant rise in the pressure in the metallic mode, and it transits to the poisoned mode at 7.8 sccm of reactive gas flow. (c) For Al, the discharge voltage drops due to the higher secondary electron emission from the poisoned surface. (d) For Ti, the discharge voltage increases due to lower yield of secondary electrons from the target surface. In *CD* region, at poisoning mode, a specific flow rate of 7 sccm of reactive gas is marked by an arrow sign.

To investigate the effect of long-term poisoning, the centre point of region CD was specified (marked by an arrow sign). Reactive sputtering was started at 7 sccm of N_2 flow rate in the poisoning mode. For both Al and Ti, the nitride films were deposited on natively oxidized Si wafers during first the 10 min of target poisoning and after 60 min of target poisoning (the detailed procedure is given in section 3.3). It is worth mentioning that the discharge voltage and chamber pressure remained stable during 60 min of reactive sputtering in the poisoning mode.

6.2 Microstructure of the deposited films

Nucleation and structure of films grown by physical vapour deposition are influenced by different deposition parameters such as substrate temperature, deposition rate [77], energy of the bombarding particles and impurities [78]. Under different poisoning conditions, the variation in thickness of the compound layer on the target, different composition and binding energies of the sputterd species and impurities could influence the final film structure. Figure 38 shows SEM micrographs for cross-sectional view for TiN and AlN films deposited at different poisoning conditions. Also, their surfaces can be qualitatively assessed due to the slight tilt of the samples in the SEM.

Figure 38(a) shows the SEM image and surface morphology of the AlN film deposited after short-term poisoning. It shows a polysrystalline structure with short columns and void spaces. The cross-sectional view and surface morphology of the AlN film deposited after long-term poisoning is is shown in figure 38(b). A non columnar structure (towards amorphization) with small paricles dispersed on the entire surface was observed.

Figure 38(c) shows the SEM image and surface topograpghy of a TiN film deposited after short-term poisoning. A columnar structure was observed in the whole film. The columns are not vertically aligned and point in different directions. The cross-sectional view and surface morphology of the TiN film deposited after long-term poisoning is shown in figure 38(d). A comparatively more uniform columnar structure with a smooth top surface was observed.

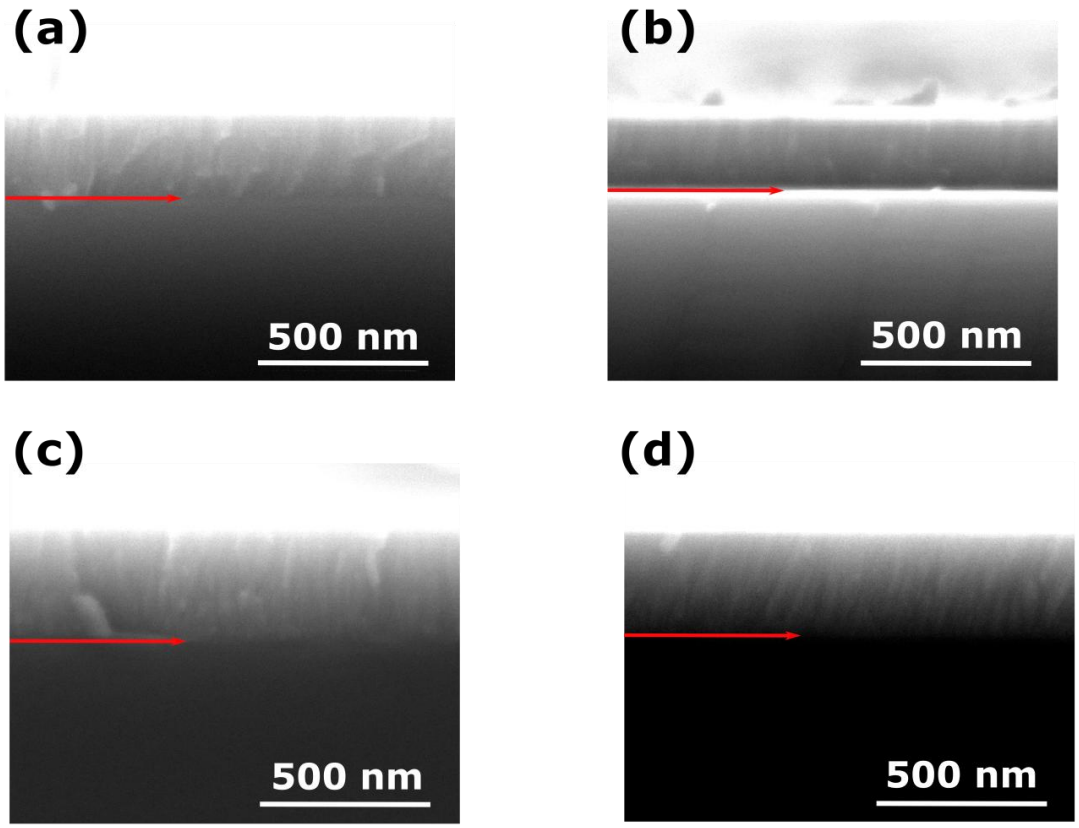

Figure 38: Cross-sectional view SEM photographs for AlN and TiN films deposited at different poisoning levels of the targets. (a) Cross-sectional view of AlN film deposited during short-term poisoning. (b) SEM image for AlN film deposited after long-term poisoning. (c) Cross-sectional view of TiN film deposited after short-term poisoning. (d) SEM image for TiN film deposited after long-term poisoning. Arrows indicate the position of the interface coatings/substrate.

The surface morphology of the deposited films was measured by AFM in non contact mode. RMS roughness was also measured for a surface area of 1μm^2 for each sample. Figure 39 shows the AFM images for surface morphology (plan view) of AlN and TiN films deposited at short-term and long-term poisoning of the respective targets. The images were analyzed using the *Nano Scope Analysis* (version 1.5) software. First of all the images were flattened with the flattening tool implemented in the software to remove tilt and bow. 2D images of the AlN and TiN films are shown in figure 39.

Figure 39(a) shows the AFM image of the AlN film deposited after short-term poisoning. The scan shows separated regions with porosity in between. The RMS roughness value was measured as 2.4 nm. For the AlN film deposited after long-term poisoning as shown in figure 39(b), a dense structure covered by small particles was

observed. An increase in surface roughness was observed due to small particles dispersed on the entire surface. RMS roughness for a surface area of 1μm^2 was measured as 11.0 nm. However, for certain surface areas without small particles (shown by dotted line circle in 39(b)), a RMS roughness value of 2.6 nm was observed after long-term poisoning.

Figure 39(c) shows the surface topography of a TiN film deposited after short-term poisoning. A ripple like surface was observed which shows that the top facets of the columns are sharp edged. The RMS roughness value was measured as 1.1 nm. The surface morphology of a TiN film deposited after long-term poisoning is shown in figure 39(d). The AFM scan shows a rather smooth surface with less ripples. The columns are not faceted and the RMS roughness was decreased to 0.9 nm.

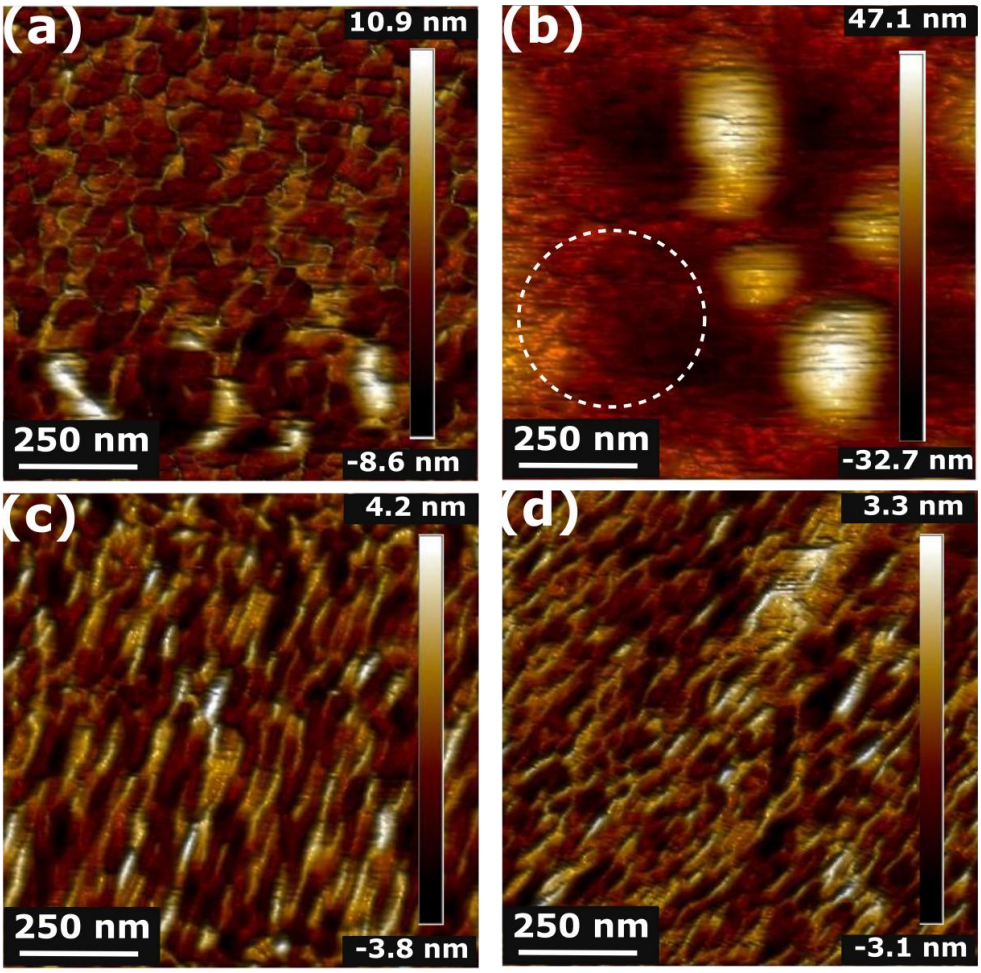

Figure 39: Plan view AFM scans for AlN and TiN films deposited at different poisoning levels of the targets. (a) AFM image of the AlN film deposited after short-term poisoning. (b) Topographic image of AlN film deposited after long-term poisoning. (c) Surface morphology of TiN film deposited after short-term poisoning. (d) Topographic image of TiN film deposited after long-term poisoning.

6.3 Crystallographic orientation

The crystal structure and preferred orientation of the AlN and TiN films, sputter deposited at different poisoning conditions, were characterized by XRD using the copper Kα radiation. Figure 40 shows the relative intensities of the XRD peaks for both AlN and TiN films deposited at short-term and long-term poisoning and the corresponding temperature rise of the substrates during the 10 min of the deposition process.

Figure 40(a) shows the diffraction pattern for an AlN film deposited during the first 10 min of poisoning. The pattern was compared with the standard corresponding diffraction file for AlN (04-010-6161) [79]. The XRD pattern shows the hexagonal structure and AlN phase was confirmed from the peak positions. The pattern shows that the [101] peak is more prominent at 37.84°. Other peaks [002], [103], [112] were also observed at 36.06°, 66.02° and 71.27°, respectively. Figure 40(b) shows the diffraction pattern for an AlN film deposited after long-term poisoning. However, after prolonged poisoning time, the [103] peak at 66.02° becomes more prominent and the intensity of [102] and [002] peaks also slightly increases. The FWHM of the [103] peak was also increased from 0.95° to 1.09° after longer poisoning time showing less crystalline films. AlN with [103] peaks is an attractive piezoelectric material previously deposited at higher sputtering power [80]. The [002] orientation has also been reported at higher sputtering power [81].

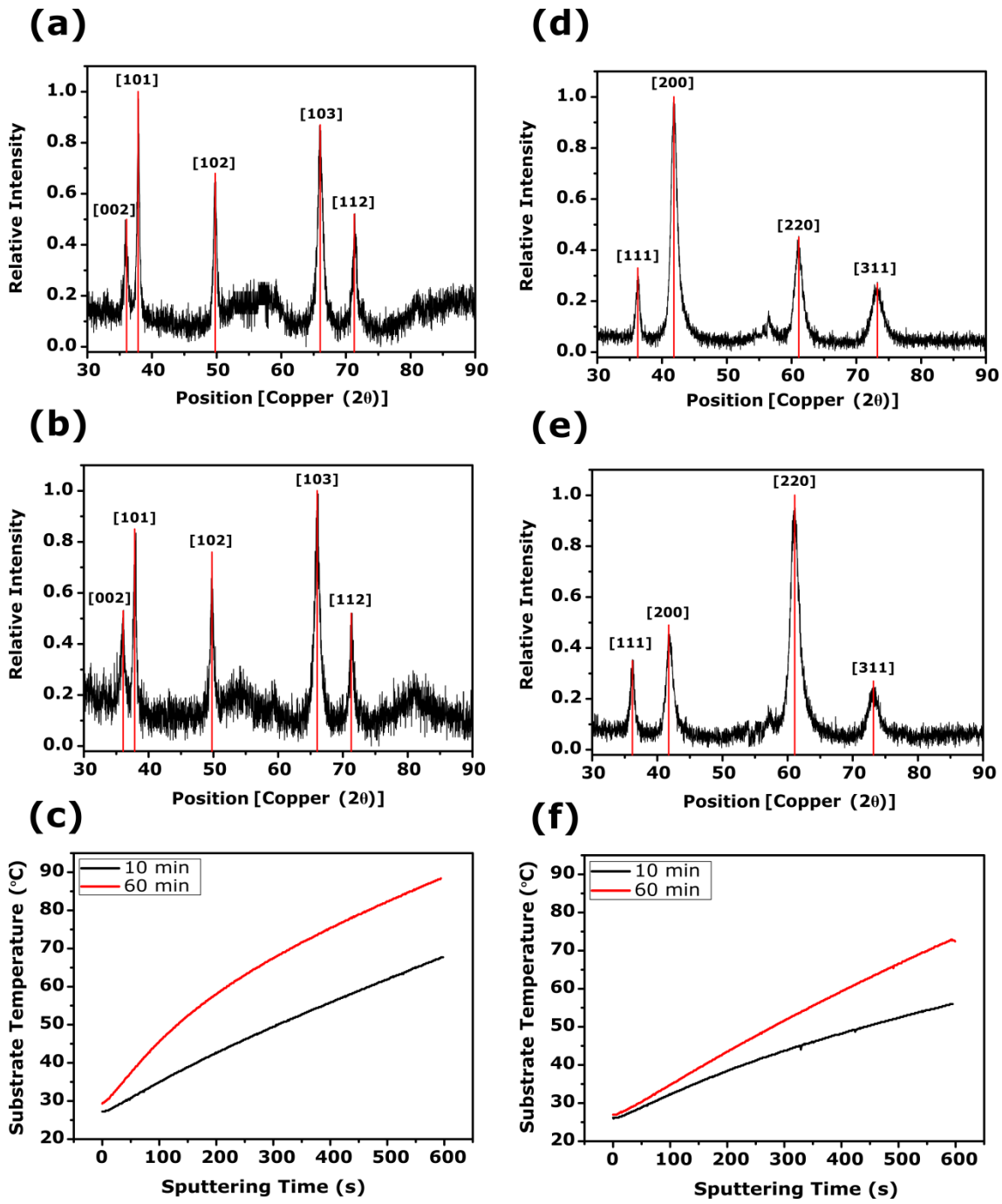

Figure 40: Relative intensities of the X-ray diffraction peaks for both AlN and TiN films deposited at different poisoning levels and corresponding temperature of the substrates during the deposition process. (a) XRD measurements for AlN film deposited at short-term poisoning. (b) XRD measurements for AlN film deposited at long-term poisoning. (c) Substrate temperature during deposition of AlN film at two different poisoning levels. (d) X-ray diffraction peaks of TiN film deposited at short-term poisoning. (e) X-ray diffraction peaks of TiN film deposited at long-term poisoning. (f) Substrate temperature during deposition of TiN film at two different poisoning levels.

The possible reason for the structural changes may be the higher energy flux of the impinging particles on the substrate after prolonged poisoning of the target. To check the effect of different energy of impinging particles on the substrate, the substrate temperature was also measured during the deposition process. It is worth mentioning that care was taken that the sputtering chamber had the same temperature for all investigated deposition conditions. To eliminate the effect of chamber temperature after long-term sputtering, the depositions were started at the same environmental temperature. For this purpose, during long-term poisoning, the target was poisoned for 60 min and then the sputtering power was cut off. Next day the film was deposited on a natively oxidized Si wafer at the same poisoning mode and initial temperature conditions similar to the ones of short-term poisoning (chamber temperature approx. 19 °C). Figure 40(c) shows the substrate temperature for AlN deposition at different poisoning conditions. A higher substrate temperature and a stronger temperature rise were observed for deposition after long-term poisoning as compared to that for short-term poisoning. This higher substrate temperature for deposition after 60 min of poisoning supports our assumption of the higher energy flux of the impinging particles on the substrate.

Figure 40(d) shows the x-ray diffraction pattern for a TiN film deposited during short-term poisoning. The standard XRD pattern file for TiN (04-007-4803) was used for the confirmation of the planes [82]. The pattern shows [111], [200], [220] and [311] peaks at 36.23°, 41.83°, 61.11° and 73.25°, respectively. The highest relative intensity was observed for the [200] peak. This preferred orientation has been reported due to a higher N_2 flow rate during the deposition process [83]. The reference pattern confirms the cubic structure but the peaks were slightly shifted to lower 2θ values (see table 2). Upon increasing 2θ values this shift was slightly increased which shows that it is not due to a measurement error. This shift is probably due to the compressive stress of the deposited films[32]. Using these 2θ values, the lattices inter planar distances *d* were determined for each peak/plane by using Bragg's law [84].

$$\lambda = 2d\sin\theta \tag{21}$$

with λ being the wavelength of the incoming x-rays, and θ the diffraction angle. The strain ϵ was calculated by comparing the unstressed (reference) lattice inter-planar spacing d_o with the strained inter-planar spacing *d* as given.

$$\varepsilon = \frac{d - d_0}{d_o} \tag{22}$$

Finally the stress σ was determined by using the relation

$$\sigma = E\varepsilon \tag{23}$$

Where *E* represents the modulus of elasticity for TiN (251 GPa). Higher compressive stress was observed for samples deposited after long-term poisoning as shown in table 2. High compressive stresses (-6 GPa to -1 GPa) have previously been observed in TiN films [85, 86]. It was found that the energy flux of the particles also influences the stress level of sputter deposited TiN films [87]. Due to these compressive stresses, also delaminations triggered by the buckling instability were observed for some samples prepared after long-term poisoning [88]. The diffraction pattern for the TiN film deposited after long-term poisoning is shown in Figure 40(e). The same peaks were observed but the relative intensity of [200] was decreased and that of [220] was increased. This transition to [220] is associated with a higher energy of incident particles [89]. The higher energy increases the mobility of the deposited atoms. This facilitates the diffusion of adsorbed atoms to dense lattice planes. At the same time, the shifting angle of the peaks with reference to the standard pattern was increased as shown in table 2. Similarly the substrate temperature was measured during the deposition at two different poisoning conditions. Figure 40(f) shows the substrate temperature for TiN during short-term and long-term poisoning. Higher substrate temperature was again observed during the deposition after long-term poisoning. Table 2 shows the position of peaks for TiN films deposited at the two different poisoning conditions and relative shifts from the reference peaks. The higher shifting angles correspond to higher compressive stress. Full widths at half maximum (FWHM) were also measured for different peaks. An increase in FWHM values was observed for [111], [200] and [220] orientations. However, for [311] orientation, the FWHM value was decreased. Increased FWHM corresponds to the more fine grained films observed in SEM and AFM. After prolonged sputtering in the poisoning mode, the content of the compound at the target surface increases. The different sputter yields of the target material and the compound could lead to the different energy flux to the substrate which subsequently changes the energy of the sputtered particles.

The energy flux of the sputtered atoms was also determined from the temperature gradients of the substrate for both AlN and TiN films deposited at different poisoning

levels. For a given thickness of the film, the number of deposited particles Z hitting the sensor can be estimated to be,

$$Z = \frac{A \cdot d \cdot \rho}{m_{At}} \tag{24}$$

Where A, d, ρ and m_{At} represent the sensor area, film thickness, density of coating material and atomic mass of coating material, respectively. An average density value of the coating material was used as per composition of the film as shown in table 3 and 5. The heat dissipated Q by the Cu plate (substrate holder as shown in figure 17(b), 30 mm in diameter and 3 mm in thickness) was then determined by the relation

$$Q = \rho \cdot V \cdot c \cdot (\Delta T) \tag{25}$$

Where ρ, V, c, $\triangle T$ and t represent the density of Cu, volume of the Cu plate, specific heat of Cu, change in temperature and coating time, respectively. The change in temperature, $\triangle T$, was determined by subtracting the initial temperature from the final temperature (at 600 s sputtering time) of the substrate. Finally, the energy of each atom was calculated by dividing the heat dissipated, Q, by the number of the particles, Z, determined by equation (24).

For AlN, the energy of the atoms, for short-term and long-term poisoning, reaching the substrate was calculated as 119 eV and 255 eV, respectively. A similar trend of increasing energy was observed for TiN films deposited after long-term poisoning. For short-term poisoning the energy of the atoms was calculated as 45 eV. The energy of the incident atoms was increased to a value of 66 eV after long-term poisoning. However, one should be cautious about these energy values while interpreting the sputtering parameters and the resulting structure of the films as the temperature gradient is not only due to the deposited atoms. In addition to sputtered particles, the electrons, backscattered neutrals and ions reaching the grounded substrate also contribute the total energy flux. Nonetheless, the different crystallographic orientations of the deposited films observed here can be correlated with the higher energy input for long-term poisoning.

Table 2.

Reference and measured XRD peak positions for TiN films deposited at short-term and long-term poisoning.

Reference angle & plane	Poisoning time	Measured angle (deg.)	Difference (deg.)	FWHM (deg.)	Stress (GPa)
36.67 [111]	Short-term	36.23	0.44	0.68	-2.92
	Long-term	36.17	0.60	0.82	-3.33
42.59 [200]	Short-term	41.83	0.76	1.22	-4.37
	Long-term	41.75	0.84	1.29	-4.84
61.81 [220]	Short-term	61.11	0.70	1.46	-2.60
	Long-term	61.07	0.74	1.60	-2.75
74.07 [311]	Short-term	73.25	0.82	2.09	-2.41
	Long-term	73.17	0.90	1.93	-2.65

6.4 Chemical composition

The chemical composition of the films deposited at different poisoning conditions (short-term and long-term) was determined by XPS. The detailed composition of the films was determined both at the surface and in the bulk. The content values are listed in units of relative atomic percent. The accuracy of XPS measurements is around 10–20 % of the values shown. Table 3 shows the composition of AlN films deposited at short-term (AlN-10) and long-term (AlN-60) poisoning. An increase in N_2 content was observed in AlN coatings after long-term poisoning. For surface analysis, the Al/N ratio was decreased from 1.14–1.07 between AlN samples deposited at short-term and long-term poisoning. This variation is more prominent for the bulk measurements where the Al/N ratio varies from 1.62–1.07 for short-term and long-term poisoning. The XPS results show that the longer poisoning time increases the nitrogen concentration in the deposited films. The sputtering of AlN from the poisoned target surface contributes to the higher N content. AlN with a high band gap (6.2 eV) has dominant metal-nitrogen interactions, so a higher concentration of nitrogen at the target surface could lead to a high AlN content. The sputtering of AlN

from the poisoned target surface can contribute to the increased amount of nitrogen in the deposited film after a prolonged poisoning of the target surface.

In addition to nitrogen, a significant concentration of oxygen was also observed in both AlN samples deposited at different poisoning levels. Previously it has been reported that oxygen exists in AlN films even under ultra high vacuum conditions and transforms the film structure towards amorphization [90, 91]. A higher oxygen content was observed at the surface of the samples. For samples prepared at short-term and long-term poisoning levels, the oxygen content at the surface was 19.6 and 17.4 atomic %, respectively. The environmental impact of oxygen could not be eliminated as samples have been stored in air and the atmospheric oxygen can react with the Al to form oxides. An oxygen content value of 12.3 and 17.3 atomic % was also found in the bulk for samples prepared at short-term and long-term poisoning levels, respectively. For the long-term poisoning sample, the higher nitrogen content could lead to less oxidation of the surface, thus leading to comparatively smaller oxygen content at the surface. In addition, implantation of oxygen during the Ar-ion sputter process employed for material removal in the XPS system could increase the registered oxygen content in the bulk.

Table 3.

Composition AlN films deposited at short-term (AlN-10) and long-term (AlN-60) poisoning.

Sample		**Al (at %)**	**N (at %)**	**O (at %)**
AlN-10	Surface	38.6	33.9	19.6
	Bulk	49.1	30.4	12.3
AlN-60	Surface	36.9	34.1	17.4
	Bulk	39.5	37.0	17.3

N1s detail spectra were analyzed as well to gain further insight into the bonding environments of nitrogen. Table 4 shows the detailed analysis of AlN and binding energies of the nitrogen components. N-I and N-II have a binding energy of 396.9 and 399.0 eV, respectively. The concentration of N-I, which is characteristic for the AlN bond increases for the samples deposited after long-term poisoning both for surface and bulk analysis. With larger content of AlN, the long-term poisoning shows more stoichiometric coatings. Similarly, the concentration of N-II, which is generally, referred as Aluminum oxynitride (Al-N-O) decreases for both samples for surface and bulk analysis after long-term

poisoning. The higher nitrogen content after long-term poisoning could lead to a smaller concentration of N-II.

Table 4.

Detailed analysis of AlN films deposited at short-term (AlN-10) and long-term (AlN-60) poisoning.

Sample		**N-I (**AlN**)**	**N-II (**Al-N-O**)**
AlN-10	Surface	90.6	9.4
	Bulk	89.6	10.4
AlN-60	Surface	92.2	7.8
	Bulk	92.4	7.6
Binding energy (eV)		396.9	399.0

For TiN, the XPS analysis showed a decrease in N_2 content and a substantial increase in Ti content for the film deposited after long-term poisoning as shown in table 5. Therefore, an increase in Ti/N ratio was observed for both surface and bulk measurements between short-term and long-term poisoning. For the surface, the Ti/N ratio value of 0.86 at short-term poisoning was increased to 1.62 for long-term poisoning. Also, for the bulk analysis, the Ti/N ratio value 0.81 at short-term poisoning was increased to 1.85 after long-term poisoning. Similarly, for TiN films the presence of oxygen was noticed for both samples.

Table 5.

Composition of TiN films deposited at short-term (TiN-10) and long-term (TiN-60) poisoning**.**

Sample		**Ti (at %)**	**N (at %)**	**O (at %)**
TiN - 10	Surface	32.2	37.7	14.0
	Bulk	32.9	40.5	11.8
TiN- 60	Surface	44.2	27.3	10.2
	Bulk	51.5	27.8	13.3

To quantify the effect of oxygen, Ti 2p spectra (split spin orbit components) were also analyzed. TiN spectra have a complex shape with several peaks overlapping. Figure 41 shows the XPS spectra for TiN films prepared after short-term poisoning at the surface and in the bulk. The three components of the Ti $2p^{3/2}$ are associated with TiN, Titanium oxynitride (Ti-O-N) and Titanium dioxide (TiO_2), respectively[92, 93]. Although all the three components of Ti 2p spectra are distinguishable, the third component consists of an overlap of satellite signals from TiN and the Ti-O-N signal. Therefore, numbers given in the table 6 for the TiN and Ti-O-N can only be understood as minimum and maximum estimates, respectively. Table 6 shows the concentration and binding energies of split spin orbit components of Ti. The concentration of TiN was decreased both at surface and bulk for the film deposited after long-term poisoning of the target. Overall a higher concentration of Ti-O-N, with binding energy of 456.0 eV was observed for both samples at the surface and in the bulk.

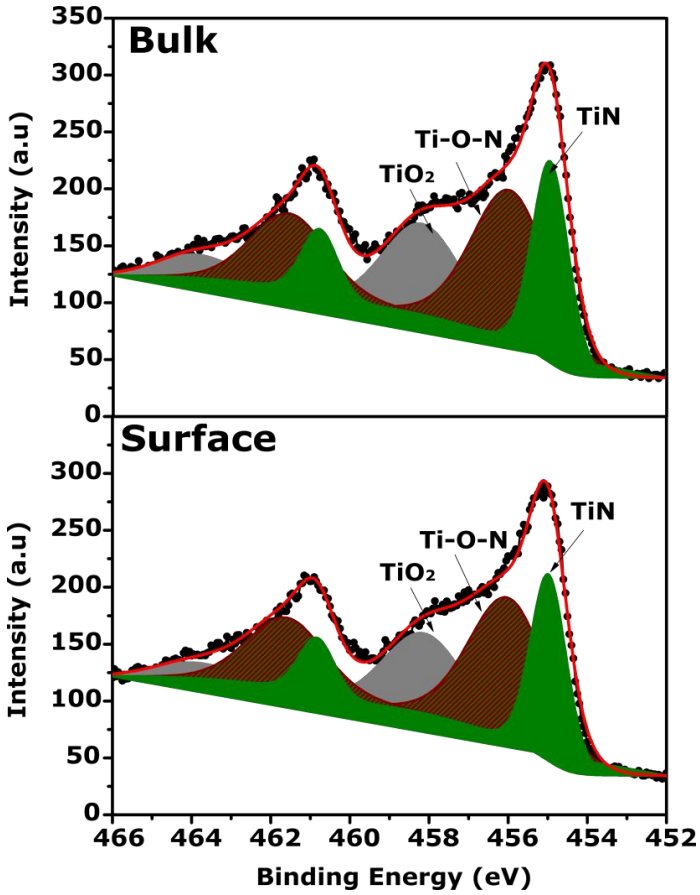

Figure 41: XPS Ti 2p spectra for TiN films at the surface and in the bulk prepared after short-term poisoning.

TiO_2 was also observed for both samples at the surface and in the bulk. However, a higher value of TiO_2 was observed in the bulk for the sample prepared after long-term poisoning. TiN with an intermediate band gap (3.4 eV) exhibits dominant metal-metal interactions and the compound is mostly sputtered as Ti and nitrogen atoms. As Ti getters oxygen in a more efficient way, a significant part of Ti was reacted with oxygen to form TiO_2 and Ti-O-N. In the bulk, during the long-term poisoning, the higher temperature of the substrates as observed in the heating curves (figure 40(f)) could have increased the reactivity for oxygen. However, films deposited with short-term poisoning are N-rich and after long-term poisoning transform to Ti-rich coatings.

Table 6.

Detailed analysis of TiN films deposited at short-term (TiN-10) and long-term (TiN-60) poisoning.

Sample		TiN **(at %)**	Ti-O-N **(at %)**	TiO_2 **(at %)**
TiN - 10	Surface	26.5	50.7	22.9
	Bulk	26.2	48.7	25.1
TiN- 60	Surface	21.8	51.0	27.2
	Bulk	23.3	44.9	31.9
Binding energy (eV)		455.0	456.0	458.0

To summarize the effect of target poisoning on the composition of AlN and TiN films it could be observed that at higher target poisoning level, a comparatively higher substrate temperature was measured. This can be attributed to a higher energy flux arriving at the substrate. At short-term poisoning, the preferred XRD peaks for AlN and TiN were observed at [101] and [200], respectively. However, after long-term poisoning, [103] and [220] preferred peaks were observed for AlN and TiN, respectively. Also changes in composition could be detected when comparing short and long-term poisoning, thus suggesting that the dynamics of the poisoning process is not stopping. So the ongoing change in the state of target poisoning finally also influences the growth of films deposited from targets with different degrees of poisoning.

7. Conclusions and outlook

In summary, we described an experimental approach to in-situ monitor the surface roughness of a uniformly eroded cylindrical sputtering target by reflection of a laser beam. The eroded region of the target was modeled as a random arrangement of microfacets. Using this approach, we reconstructed the roughness profiles by using the reflected pattern of the laser beam from the eroded surfaces of Al, Cu and Ti targets. We get a good agreement among different roughness parameters, RMS roughness, correlation length, skewness and kurtosis of both measured and generated profiles. With this in-situ surface analysis of a sputtering target, it is possible to monitor the onset of target roughening and temporal behaviour of roughness evolution upon erosion.

We applied this approach to the in-situ assessment of target poisoning evolution in magnetron sputtering. Cylindrical Al and Ti targets were reactively sputtered in metallic and poisoned modes under different flow rates of N_2 and O_2. The poisoned surface of the targets was hit by a laser beam and reflected intensity images were captured on a screen incorporated inside the sputtering chamber. From this intensity distribution, the mean tilt angle of the target surface was calculated at different flow rates of the reactive gases. Gradual changes in mean tilt angles were observed with increasing sputtering time. Particularly, a trend of decreasing roughness was observed in poisoning modes up to 60 minutes of sputtering. No saturation was observed in target roughness development even after 60 min of reactive sputtering, thus suggesting that chemical reactions and morphological changes occur at the target surface and sub-surface regions even after prolonged sputtering time. A decrease in deposition rate was also observed in poisoning modes between short (10 min) and long-term (60 min) poisoning. Therefore, the change in target roughness can be related to the formation of the compound layer. As a proof of concept, we also measured de-poisoning time after 10 and 60 minutes of reactive sputtering. For oxides, a longer de-poisoning time was observed after 60 minutes of reactive sputtering as compared to that for 10 minutes, while for nitrides this effect was absent or very minor. We established a good agreement between the roughness evolution and de-poisoning time for long-term poisoning up to 60 minutes. The technique of laser reflectometry can therefore be applied for the assessment of the target poisoning.

The effect of short-term and long-term target poisoning on the microstructure, preferred orientation and composition of AlN and TiN films was also investigated. The nitride films were deposited on natively oxidized Si wafers for 10 min duration during the

first 10 min (short-term) and after 60 min (long-term) of target poisoning. At higher poisoning level, a comparatively higher substrate temperature was observed due to higher energy of the sputtered particles arriving at the substrate. Smaller values of RMS roughness were observed for the samples prepared at long-term poisoning as compared to those prepared at short-term poisoning. At short-term poisoning, the preferred XRD peaks for AlN and TiN were observed at [101] and [200], respectively. However, after long-term poisoning, [103] and [220] preferred peaks were observed for AlN and TiN, respectively. Generally, the peaks observed after long-term poisoning are usually found in films deposited at higher sputtering power and particle energies. For AlN, the Al/N ratio was decreased for films deposited after long-term poisoning of the target surface. However, for TiN films, the Ti/N ratio was increased after long-term poisoning. Ti-rich coatings with higher compressive stress were observed after long-term poisoning of the target. Oxygen was also observed to be present in AlN and TiN films in both the surface and in the bulk of the coatings. The results show that the different target poisoning levels strongly influence the properties of the deposited films most probably by changing the composition of the vapor beam and by influencing the energy flux towards the substrate.

Finally, future work can comprise the following points:

First of all it can be considered to reconstruct the rough target surface more precisely by using the full field of reflected intensity. The restriction that facets are only tilted out of the tangential plane can be dropped and each point within this field can then be related to a certain tilt of a facet in three dimensions. From these data the full 2-D target surface may be reconstructed. Further on, in the case of reactive sputtering, by relating the target surface evolution to the composition of the compound layer, a multi layer reflection model based on the optical constants of both, the transparent compound layer and the underlying metal, can be constructed for the assessment of target poisoning. Also the energy distribution of the sputtered particles due to different surface binding energies at different poisoning levels of the target surface can be addressed and additional substrate biasing can be applied to regulate the temperature gradients and resulting stresses of the deposited films.

So, in conclusion, laser reflectometry cannot only be considered as an efficient in-situ target surface monitoring technique to extract the surface features, but also for the assessment of target poisoning evolution during reactive sputtering.

References

[1] J.A. Thornton, Magnetron sputtering: basic physics and application to cylindrical magnetrons, J. Vac. Sci. Technol. A, 15 (1978) 171-177.

[2] R.D. Gryse, J. Haemers, W.P. Leroy, D. Depla, Thirty years of rotatable magnetrons, Thin Solid Films 520 (2012) 5833-5845.

[3] F. Boydens, W.P. Leroy, R. Persoons, D. Depla, The influence of target surface morphology on the deposition flux during direct-current magnetron sputtering, Thin Solid Films, 531 (2013) 32-41.

[4] M.A. Makeev, A.-L. Barabási, Effect of surface morphology on the sputtering yields. I. Ion sputtering from self-affine surfaces, Nucl. Instr. Meth.Phys. Res. B, 222 (2004) 316-334.

[5] M.A. Makeev, A.-L. Barabási, Effect of surface morphology on the sputtering yields. II. Ion sputtering from rippled surfaces, Nucl. Instr. Meth. Phys. Res. B, 222 (2004) 335-354.

[6] Q. Wei, M. Eddy, K.-D. Li, L. Wang, Influence of surface morphology on sputtering yields, J. Phys. D: Appl. Phys., 42 (2009) 165304.

[7] T.R. Thomas, Rough Surfaces, Imperial College Press, London, 1999.

[8] G.M. Clarke, Roughness measurement with a laser scanning analyser, Wear, 57 (1979) 107-116.

[9] U. Persson, In-process measurement of surface roughness using light scattering, Wear, 215 (1998) 54-58.

[10] S. Wang, Y. Tian, C.J. Tay, C. Quan, Development of a laser-scattering-based probe for on-line measurement of surface roughness, Appl. Opt., 42 (2003) 18-24.

[11] K.E. Torrance, E.M. Sparrow, Theory for off–specular reflection from roughened surfaces, J. Opt. Soc. Am., 57 (1967) 1105-1114.

[12] M. Oren, S.K. Nayar, Generalization of the lambertian model and implications for machine vision, Int. J. Comput. Vis., 14 (1995) 227-251.

[13] L.B. Jonsson, T. Nyberg, S. Berg, Target compound layer formation during reactive sputtering, J. Vac. Sci. Technol. A, 17 (1999) 1827-1831.

[14] S.H.-O.B. Berg, T. Larsson and C. Nender, Modeling of reactive sputtering of compound materials, J. Vac. Sci. Technol. A, 5 (1987) 202-207.

[15] R. Schelfhout, K. Strijckmans, F. Boydens, D. Depla, On the target surface cleanness during magnetron sputtering, Appl. Surf. Sci., 355 (2015) 743-747.

[16] Y. Abe, K. Takamura, M. Kawamura, K. Sasaki, Target surface oxide layer formed by

reactive sputtering of Ti target in Ar+O[sub 2] mixed gas, J. Vac. Sci. Technol. A, 23 (2005) 1371-1374.

[17] Y. Chiba, Y. Abe, M. Kawamura, K. Sasaki, Formation process of Al2O3 thin film by reactive sputtering, Vacuum, 83 (2008) 483-485.

[18] D. Güttler, B. Abendroth, R. Grötzschel, W. Möller, D. Depla, Mechanisms of target poisoning during magnetron sputtering as investigated by real-time in situ analysis and collisional computer simulation, Appl. Phys. Lett., 85 (2004) 6134-6136.

[19] J.M. L. Combadiere, Study and control of both target-poisoning mechanisms and reactive phenomenon in reactive planar magnetron cathodic sputtering of TiN, Surf. Coat. Tech., 82 (1996) 145-157.

[20] T.B. Jackson, A.V. Virkar, K.L. More, R.B.D. Jr, R.A. Cutler, High-Thermal-Conductivity Aluminum Nitride Ceramics: The Effect of Thermodynamics, Kinetic, and Microstructural Factors, J. Am. Ceram. Soc., 80 (1997).

[21] C. Caliendo, P. Imperatori, E. Cianci, Structural, morphological and acoustic properties of AlN thick films sputtered on Si(001) and Si(111) substrates at low temperature, Thin Solid Films, 441 (2003) 32-37.

[22] M.-A. Dubois, P. Muralt, Stress and piezoelectric properties of aluminum nitride thin films deposited onto metal electrodes by pulsed direct current reactive sputtering, J. Appl. Phys., 89 (2001) 6389-6395.

[23] P.B. Legrand, M. Wautelet, B. Dugnoille, J.P. Dauchot, M. Hecq, Optical properties of sputter-deposited aluminium nitride films on silicon, Thin Solid Films, 248 (1994) 220-223.

[24] M.F. Zhu, A.H. Hamdi, M.-A. Nicolet, Stable ohmic contact to GaAs with TiN diffusion barrier, Thin Solid Films, 119 (1984) 5-9.

[25] M.H. Jacobs, Process and engineering benefits of sputter-ion-plated titanium nitride coatings, Surf. Coat. Tech., 29 (1986) 221-237.

[26] S. Niyomsoan, W. Grant, D.L. Olson, B. Mishra, Variation of color in titanium and zirconium nitride decorative thin films, Thin Solid Films, 415 (2002) 187-194.

[27] A. Scarano, M. Piattelli, G. Vrespa, S. Caputi, A. Piattelli, Bacterial Adhesion on Titanium Nitride-coated and Uncoated Implants: An In Vivo Human Study, J Oral Implantol., 29 (2003) 80-85.

[28] G.S. Chen, J.J. Guo, C.K. Lin, C.-S. Hsu, L.C. Yang, J.S. Fang, Evaluation of radio-frequency sputter-deposited textured TiN thin films as diffusion barriers between copper and silicon, J. Vac. Sci. Technol. A, 20 (2002) 479-485.

[29] R. Banerjee, K. Singh, P. Ayyub, M.K. Totlani, A.K. Suri, Influence of the Ar/N2 ratio on the preferred orientation and optical reflectance of reactively sputter deposited titanium nitride thin films, J. Vac. Sci. Technol. A, 21 (2003) 310-317.

[30] D. Mahéo, J.M. Poitevin, Structure of TIN films deposited on heated and negatively biased silicon substrates, Thin Solid Films, 215 (1992) 8-13.

[31] M. Clement, E. Iborra, J. Sangrador, A. Sanz-Hervás, L. Vergara, M. Aguilar, Influence of sputtering mechanisms on the preferred orientation of aluminum nitride thin films, J. Appl. Phys., 94 (2003) 1495-1500.

[32] C. Saringer, R. Franz, K. Zorn, C. Mitterer, Effect of discharge power on target poisoning and coating properties in reactive magnetron sputter deposition of TiN, J. Vac. Sci. Technol. A, 34 (2016) 041517.

[33] S. Berg, T. Nyberg, Fundamental understanding and modeling of reactive sputtering processes, Thin Solid Films, 476 (2005) 215-230.

[34] D. Depla, R. De Gryse, Target poisoning during reactive magnetron sputtering: Part I: the influence of ion implantation, Surf. Coat. Tech., 183 (2004) 184-189.

[35] D. Depla, R. De Gryse, Target poisoning during reactive magnetron sputtering: Part II: the influence of chemisorption and gettering, Surf. Coat. Tech., 183 (2004) 190-195.

[36] D. Güttler, W. Möller, The influence of non-uniform target poisoning on the energy distributions of atoms sputtered in a reactive dc magnetron discharge, Plasma Sources Sci. Technol., 17 (2008) 025016.

[37] R. Roth, J. Schubert, E. Fromm, Process control of magnetron sputtering of TiN coatings studied by in situ AES and plasma diagnostics, Surf. Coat. Tech., 74-74 (1995) 461-468.

[38] S. Mráz, J.M. Schneider, Energy distribution of O^- ions during reactive magnetron sputtering, Appl. Phys. Lett., 89 (2006) 051502.

[39] K. Wittmaack, Effect of surface roughening on secondary ion yields and erosion rates of silicon subject to oblique oxygen bombardment, J. Vac. Sci. Technol. A, 8 (1990) 2246.

[40] S. Berg, T. Larsson, C. Nender, H.O. Blom, Predicting thin-film stoichiometry in reactive sputtering, J. Appl. Phys., 63 (1988) 887.

[41] G. Buyle, W. De Bosscher, D. Depla, K. Eufinger, J. Haemers, R. De Gryse, Recapture of secondary electrons by the target in a DC planar magnetron discharge, Vacuum, 70 (2003) 29-35.

[42] W.D. Westwood, S. Maniv, P.J. Scanlon, The current-voltage characteristic of magnetron sputtering systems, J. Appl. Phys., 54 (1983) 6841-6846.

[43] N. Matsunami, Y. Yamamura, Y. Itikawa, N. Itoh, Y. Kazumata, S. Miyagawa, K. Morita, R. Shimizu, H. Tawara, Energy dependence of the ion-induced sputtering yields of monatomic solids, At. Data Nucl. Data Tables, 31 (1984) 1-80.

[44] L.B. Jonsson, T. Nyberg, S. Berg, Dynamic simulations of pulsed reactive sputtering processes, J. Vac. Sci. Technol. A, 18 (2000) 503-508.

[45] S.M. Diederik Depla, Reactive Sputter Deposition, Springer 2008.

[46] J. Schulte, G. Sobe, Magnetron sputtering of aluminium using oxygen or nitrogen as reactive gas, Thin Solid Films, 324 (1998) 19-24.

[47] S. Kadlec, J. Musil, J. Vyskocil, Influence of the pumping speed on the hysteresis effect in the reactive sputtering of thin films, Vacuum, 37 (1987).

[48] D. Depla, X.Y. Li, S. Mahieu, K. Van Aeken, W.P. Leroy, J. Haemers, R. De Gryse, A. Bogaerts, Rotating cylindrical magnetron sputtering: Simulation of the reactive process, J. Appl. Phys., 107 (2010) 113307.

[49] D. Depla, R. De Gryse, Target poisoning during reactive magnetron sputtering: Part III: the prediction of the critical reactive gas mole fraction, Surf. Coat. Tech., 183 (2004) 196-203.

[50] A.J.C. Brown, Rapid optical measurement of surfaces, Int. J. Mach. Tool. Manu., 35 (1995) 135-139.

[51] P. Sandoz, G. Tribillon, T. Gharbi, R. Devillers, Roughness measurement by confocal microscopy for brightness characterization and surface waviness visibility evaluation, Wear, 201 (1996) 186-192.

[52] T. Davies, X. Kun, A.R. Luxmoore, Digital measurement of surface profiles by automated optical sectioning, Meas. Sci. Technol., 5 (1994) 710-715.

[53] T.W. D.K. Hamilton, Three-dimensional surface measurement using the confocal scanning microscope, Appl. Phys. B, 27 (1982).

[54] T.U. Ken-ichi Nagata, Jien Nishiwaki, The determination of rms roughness and correlation length of rough surface by measuring spatial coherence function, Jpn. J. Appl. Phys., 12 (1973) 1693-1698.

[55] J.C. Leader, Analysis and prediction of laser scattering from rough-surface materials, J. Opt. Soc. Am., 69 (1979) 610-619.

[56] M. Giglio, S. Musazzi, U. Perini, Surface roughness measurements by means of speckle wavelength decorrelation, Opt. Commun., 28 (1979) 166-170.

[57] U. Persson, Measurement of surface roughness using infrared scattering, Measurement, 18 (1996) 109-116.

[58] G.H. J.C. Le Bosse, J. Lopez, J.C. Dumas, Characterisation of surface roughness by laser light scattering, diffusely scattered intensity measurement, Wear, 224 (1999) 236-244.

[59] B.R. C. Babu Rao, Study of engineering surfaces using laser-scattering techniques Sadhana, 28 (2003) 739-761.

[60] R.M. Brian Griffiths, Bruce Wilkie, Three-dimensional surface measurement using light scattering, Int. J. Mach. Tool. Manu., 35 (1995) 141-145.

[61] T. Horiuchi, Y. Tomita, R. Kammel, Surface roughness measurement with speckle intensity distribution usnig a linear image sensor, Jpn. J. Appl. Phys., 21 (1982) L743-L745.

[62] C. Cheng, C. Liu, S. Teng, N. Zhang, M. Liu, Half-width of intensity profiles of light scattered from self-affine fractal random surfaces and simulational verifications, Phys. Rev. E, 65 (2002).

[63] J.A. Ogilvy, Theory of wave scattering from random rough surfaces, IOP Publishing Ltd, London, 1991.

[64] D.J. Whitehouse, J.F. Archard, The properties of random surfaces of significance in their contact, Proc. Roy. Soc., 316 (1970) 97-121.

[65] J.A. Ogilvy, J.R. Foster, Rough surfaces, gaussian or exponential statistics, J. Phys. D: Appl. Phys., 22 (1989) 1243-1251.

[66] D. Depla, J. Haemers, G. Buyle, R. De Gryse, Hysteresis behavior during reactive magnetron sputtering of Al[sub 2]O[sub 3] using a rotating cylindrical magnetron, J. Vac. Sci. Technol. A, 24 (2006) 934-938.

[67] D. Depla, X.Y. Li, S. Mahieu, R. De Gryse, Determination of the effective electron emission yields of compound materials, J. Phys. D: Appl. Phys., 41 (2008) 202003.

[68] D.A.G. Mark A. Lewis, Jacob Jorne, Measurements of secondary electron emission in reactive sputtering of aluminum and titanium nitride, J. Vac. Sci. Technol. A, 7 (1989) 1019-1024.

[69] K. Koski, J. Hölsä, P. Juliet, Deposition of aluminium oxide thin films by reactive magnetron sputtering, Surf. Coat. Tech., 116-119 (1999) 716-720.

[70] D. Depla, S. Heirwegh, S. Mahieu, J. Haemers, R. De Gryse, Understanding the discharge voltage behavior during reactive sputtering of oxides, J. Appl. Phys., 101 (2007) 013301.

[71] S.W. MacLaren, Baker J. E. , Finnegan N. L. , Loxton C. M, Surface roughness development during sputtering of GaAs and InP: Evidence for the role of surface diffusion in ripple formation and sputter cone development, J. Vac. Sci. Technol. A, 10 (1992) 468.

[72] D. Güttler, R. Grötzschel, W. Möller, Lateral variation of target poisoning during reactive magnetron sputtering, Appl. Phys. Lett., 90 (2007) 263502.

[73] V. Naundorf, M.P. Macht, Surface roughening of copper by low energy ion bombardment, Nucl. Instr. Meth., 168 (1980) 405-409.

[74] K. Strijckmans, D. Depla, A time-dependent model for reactive sputter deposition, J. Phys. D: Appl. Phys., 47 (2014) 235302.

[75] D. Depla, S. Mahieu, R. De Gryse, Magnetron sputter deposition: Linking discharge voltage with target properties, Thin Solid Films, 517 (2009) 2825-2839.

[76] V.L. Stout, M.D. Gibbons, Gettering of Gas by Titanium, J. Appl. Phys., 26 (1955) 1488-1492.

[77] C. Eisenmenger-Sittner, The application of rate equations to describe nucleation and growth on rough substrates: tin and lead on aluminium, J. Cryst. Growth, 205 (1999) 441-452.

[78] P.B. Barna, M. Adamik, Fundamental structure forming phenomena of polycrystalline films and the structure zone models, Thin Solid Films, 317 (1998) 27-33.

[79] C. Rizzolia, P.S. Salamakha, O.L. Sologubb, G. Bocellia, X-ray investigation of the Al–B–N ternary system: isothermal section at 1500 °C: Crystal structure of the Al0.185B6CN0.256 compound, J. Alloys Compd., 343 (2002) 135-141.

[80] P.-F. Yang, S.-R. Jian, S. Wu, Y.-S. Lai, C.-T. Wang, R.-S. Chen, Structural and mechanical characteristics of (103) AlN thin films prepared by radio frequency magnetron sputtering, Appl. Surf. Sci., 255 (2009) 5984-5988.

[81] K.-H. Chiu, J.-H. Chen, H.-R. Chen, R.-S. Huang, Deposition and characterization of reactive magnetron sputtered aluminum nitride thin films for film bulk acoustic wave resonator, Thin Solid Films, 515 (2007) 4819-4825.

[82] N.W. Wong, H.F. McMurfie, B. Paretzkin, Y. Zhang, K.L. Davis, C.R. Hubbard, A.L. Dragoo, J.M. Stewart, Powder Diffraction, Cambridge University Press1987.

[83] N.K. Ponon, D.J.R. Appleby, E. Arac, P.J. King, S. Ganti, K.S.K. Kwa, A. O'Neill, Effect of deposition conditions and post deposition anneal on reactively sputtered titanium nitride thin films, Thin Solid Films, 578 (2015) 31-37.

[84] W.H. Bragg, W.L. Bragg, The Reflection of X-rays by Crystals, Proc. R. Soc. A, 88 (1913) 428-438.

[85] H. Köstenbauer, G.A. Fontalvo, M. Kapp, J. Keckes, C. Mitterer, Annealing of intrinsic stresses in sputtered TiN films: The role of thickness-dependent gradients of point defect density, Surf. Coat. Tech., 201 (2007) 4777-4780.

[86] R. Machunze, G.C.A.M. Janssen, Stress gradients in titanium nitride thin films, Surf. Coat. Tech., 203 (2008) 550-553.

[87] G. Abadias, W.P. Leroy, S. Mahieu, D. Depla, Influence of particle and energy flux on stress and texture development in magnetron sputtered TiN films, J. Phys. D: Appl. Phys., 46 (2013) 055301.

[88] A.G. Evans, J.W. Hutchinson, On the mechanics of delamination and spalling in compressed films, Int. J. Solid Struct., 20 (1984) 455-466.

[89] J.P. Zhao, X. Wang, Z.Y. Chen, S.Q. Yang, T.S. Shi, X.H. Liu, Overall energy model for preferred growth of TiN films during filtered arc deposition, J. Phys. D: Appl. Phys., 30 (1997) 5-12.

[90] V. Brien, P. Pigeat, Microstructures diagram of magnetron sputtered AlN deposits: Amorphous and nanostructured films, J. Cryst. Growth, 299 (2007) 189-194.

[91] A.v. Richthofen, R. Domnick, Metastable single-phase polycrystalline aluminium oxynitride films grown by MSIP: constitution and structure, Thin Solid Films, 283 (1996) 37-44.

[92] M.C. Biesinger, L.W.M. Lau, A.R. Gerson, R.S.C. Smart, Resolving surface chemical states in XPS analysis of first row transition metals, oxides and hydroxides: Sc, Ti, V, Cu and Zn, Appl. Surf. Sci., 257 (2010) 887-898.

[93] M.C. Biesinger, B.P. Payne, B.R. Hart, A.P. Grosvenor, N.S. McIntryre, L.W. Lau, R.S. Smart, Quantitative chemical state XPS analysis of first row transition metals, oxides and hydroxides, J. Phys. Conf. Ser., 100 (2008) 012025.

Acknowledgements

At first, thanks to Almighty Allah, the merciful and the beneficial for all his grants, he bestowed on me.

I would like to express my sincerest gratitude to my advisor, Prof. Christoph Eisenmenger-Sittner for his continuous guidance, support and encouragement. His positive outlook and confidence inspired me to complete this work.

I am thankful to my lab fellows at Vienna University of Technology for providing valuable suggestions and guidance, especially to Andreas Eder and Thomas Ernstbrunner for their excellent co-operation throughout in this research work. The SEM measurements were carried out using facilities at the University Service Centre for Transmission Electron Microscopy, Vienna University of Technology, Austria (TU Wien). XPS measurements and analysis were performed by the “Analytical Instrumentation Center” (AIC) at TU Wien. The X-Ray measurements were carried out within the X-Ray Centre of the TU Wien.

This work was supported by Higher Education Commission (HEC) of Pakistan at TU Wien, Austria (Project No. HEC-2014). I deeply acknowledge the financial support from HEC.

I express my gratitude to my parents, friends and well-wishers for their blessings that inspired me continuously. Last but not the least; I am grateful to my wife, for her quiet patience and sacrifices during my PhD studies. Thank you my kids, Ifra, Hareem and Uzair for being good kids with your mother when I was studying at TU Wien. I dedicate this thesis to my kids for being a primary motivation for my higher studies.

July , 2017

Appendix

Calculation of tilt angle

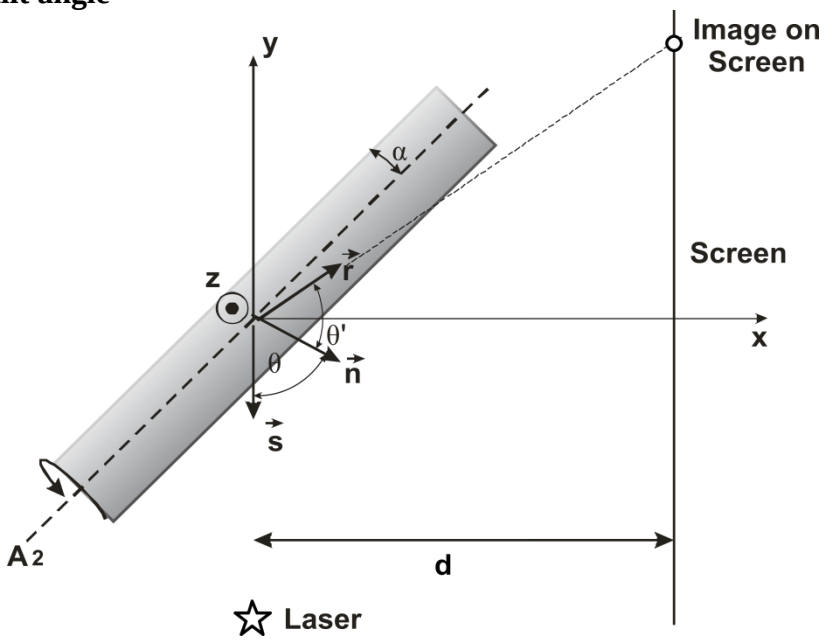

The vector $\vec{s}$ represents the incoming beam, $\vec{r}$ the reflected one and $\vec{n}$ the normal vector to the mirror plane. All three vectors lie in one plane, but this plane is not identical to the x/y-plane. $\vec{s}$ and $\vec{n}$ as well as $\vec{r}$ and $\vec{n}$ enclose the angle θ and θ', respectively, because of the reflection law $\theta = \theta'$. All three vectors shall be normalized to 1.

$\vec{s} = \begin{pmatrix} 0 \\ -1 \\ 0 \end{pmatrix}$. This vector remains unchanged for all time.

Tilting the mirror by an angle α means that the upper mirror edge shifts to the upper left hand side and the lower mirror edge shifts to the lower right hand side. The tilt axis A_2 is the first median of the *x/y*-plane. The normal vector of the mirror plane is tilted out of the *x/y*-plane and is given by

$\vec{n} = \begin{pmatrix} \frac{1}{\sqrt{2}} \cdot cos\,\alpha \\ -\frac{1}{\sqrt{2}} \cdot cos\,\alpha \\ sin\,\alpha \end{pmatrix}$. $\vec{n}$ is normalized, because $|\vec{n}|^2 = \frac{1}{2} \cdot cos^2\,\alpha + \frac{1}{2} \cdot cos^2\,\alpha + sin^2\,\alpha = 1$

Calculation of the angle θ between $\vec{s}$ and $\vec{n}$:

$$cos\,\theta = \vec{s}\cdot\vec{n} = \begin{pmatrix} 0 \\ -1 \\ 0 \end{pmatrix} \cdot \begin{pmatrix} \frac{1}{\sqrt{2}}\cdot cos\,\alpha \\ -\frac{1}{\sqrt{2}}\cdot cos\,\alpha \\ sin\,\alpha \end{pmatrix} = \frac{1}{\sqrt{2}}\cdot cos\,\alpha \cdot$$

Calculation of the normal vector $\vec{u}$ on the plane which is defined by $\vec{s}$ and $\vec{n}$ by the outer product $\vec{s}\times\vec{n}$:

$$\vec{s}\times\vec{n} = \begin{pmatrix} 0 \\ -1 \\ 0 \end{pmatrix} \times \begin{pmatrix} \frac{1}{\sqrt{2}}\cdot cos\,\alpha \\ -\frac{1}{\sqrt{2}}\cdot cos\,\alpha \\ sin\,\alpha \end{pmatrix}$$

$$\begin{pmatrix} 0 \\ -1 \\ 0 \end{pmatrix} \times \begin{pmatrix} \frac{1}{\sqrt{2}}\cdot cos\,\alpha \\ -\frac{1}{\sqrt{2}}\cdot cos\,\alpha \\ sin\,\alpha \end{pmatrix} = \begin{vmatrix} \hat{x} & \hat{y} & \hat{z} \\ 0 & -1 & 0 \\ \frac{1}{\sqrt{2}}\cdot cos\,\alpha & -\frac{1}{\sqrt{2}}\cdot cos\,\alpha & sin\,\alpha \end{vmatrix} = -\hat{x}\cdot sin\,\alpha + \hat{z}\cdot\frac{1}{\sqrt{2}}\cdot cos\,\alpha = \begin{pmatrix} -sin\,\alpha \\ 0 \\ \frac{1}{\sqrt{2}}\cdot cos\,\alpha \end{pmatrix}$$

$$\vec{u} = \vec{s}\times\vec{n} = \begin{pmatrix} -sin\,\alpha \\ 0 \\ \frac{1}{\sqrt{2}}\cdot cos\,\alpha \end{pmatrix}$$

To calculate the vector $\vec{r}$ of the reflected beam one has to observe:

(i) $\vec{r}$ is in the plane defined by $\vec{s}$ und $\vec{n}$. Therefore, for $\vec{u} = \vec{s}\times\vec{n}$ the following identity is valid $\vec{u}\cdot\vec{r} = 0$.

(ii) $\vec{r}$ shall be normalized to 1.

(iii) Angle between $\vec{n}$ and $\vec{r}$ has to be equal to θ (law of reflection).

That means:

$$\vec{u}\cdot\vec{r} = 0$$
$$\vec{r}\cdot\vec{r} = 1$$
$$\vec{r}\cdot\vec{n} = cos\,\theta$$

With

$$\vec{u} = \begin{pmatrix} -\sin\alpha \\ 0 \\ \frac{1}{\sqrt{2}} \cdot \cos\alpha \end{pmatrix}$$ and

$$\vec{n} = \begin{pmatrix} \frac{1}{\sqrt{2}} \cdot \cos\alpha \\ -\frac{1}{\sqrt{2}} \cdot \cos\alpha \\ \sin\alpha \end{pmatrix}$$ this yields:

$$-r_x \cdot \sin\alpha + r_z \cdot \frac{1}{\sqrt{2}} \cdot \cos\alpha = 0$$

$$r_x^2 + r_y^2 + r_z^2 = 1$$

$$r_x \cdot \frac{1}{\sqrt{2}} \cdot \cos\alpha - r_y \cdot \frac{1}{\sqrt{2}} \cdot \cos\alpha + r_z \cdot \sin\alpha = \cos\theta = \frac{1}{\sqrt{2}} \cdot \cos\alpha$$

Simplification yields:

$$r_z \cdot \cos\alpha - r_x \cdot \sqrt{2} \cdot \sin\alpha = 0$$

$$r_x^2 + r_y^2 + r_z^2 = 1$$

$$r_x - r_y + r_z \cdot \sqrt{2} \cdot \tan\alpha = 1$$

Solution of this system of equations:

$r_z \cdot \cos\alpha = r_x \cdot \sqrt{2} \cdot \sin\alpha$ or $r_z = r_x \cdot \sqrt{2} \cdot \tan\alpha$, it follows:

$$r_x - r_y + r_z \cdot \sqrt{2} \cdot \tan\alpha = 1$$

$$r_y = r_x + r_z \cdot \sqrt{2} \cdot \tan\alpha - 1$$

$$r_y = r_x + 2 \cdot r_x \cdot \tan^2\alpha - 1$$

$$r_y = r_x \cdot \left(1 + 2 \cdot \tan^2\alpha\right) - 1$$

Further on it follows with:

$$r_x^2 + r_y^2 + r_z^2 = 1$$
$$r_x^2 + \left(r_x \cdot \left(1 + 2 \cdot tan^2\,\alpha\right) - 1\right)^2 + 2 \cdot r_x^2 \cdot tan^2\,\alpha = 1$$
$$r_x^2 + r_x^2 \cdot \left(1 + 2 \cdot tan^2\,\alpha\right)^2 - 2 \cdot r_x \cdot \left(1 + 2 \cdot tan^2\,\alpha\right) + 1 + 2 \cdot r_x^2 \cdot tan^2\,\alpha = 1$$
$$r_x^2 + r_x^2 \cdot \left(1 + 2 \cdot tan^2\,\alpha\right)^2 - 2 \cdot r_x \cdot \left(1 + 2 \cdot tan^2\,\alpha\right) + 2 \cdot r_x^2 \cdot tan^2\,\alpha = 0$$
$$r_x^2 \cdot \left(1 + 2 \cdot tan^2\,\alpha\right) - 2 \cdot r_x \cdot \left(1 + 2 \cdot tan^2\,\alpha\right) + r_x^2 \cdot \left(1 + 2 \cdot tan^2\,\alpha\right)^2 = 0$$
$$\left(1 + 2 \cdot tan^2\,\alpha\right) \cdot r_x \cdot \left[r_x - 2 + r_x \cdot \left(1 + 2 \cdot tan^2\,\alpha\right)\right] = 0$$

This again yields

$$r_x = 0$$

or

$$r_x - 2 + r_x \cdot \left(1 + 2 \cdot tan^2\,\alpha\right) = 0$$
$$r_x + r_x \cdot \left(1 + 2 \cdot tan^2\,\alpha\right) = 2$$
$$r_x \cdot \left(1 + 1 + 2 \cdot tan^2\,\alpha\right) = 2$$
$$r_x = \frac{2}{2 + 2 \cdot tan^2\,\alpha} = \frac{1}{1 + tan^2\,\alpha}$$

For $r_x = 0$ one obtains

$$r_y = -1$$

and for $r_x = \frac{1}{1 + tan^2\,\alpha}$

one obtains with $r_y = r_x \cdot (1 + 2 \cdot \tan^2 \alpha) - 1$

$$r_y = r_x \cdot (1 + 2 \cdot tan^2\,\alpha) - 1$$
$$r_y = \frac{1}{1 + tan^2\,\alpha} \cdot (1 + 2 \cdot tan^2\,\alpha) - 1$$
$$r_y = \frac{1 + 2 \cdot tan^2\,\alpha - 1 - tan^2\,\alpha}{1 + tan^2\,\alpha} = \frac{tan^2\,\alpha}{1 + tan^2\,\alpha}$$

Calculation of r_z:

For $r_x = 0$ and $r_y = -1$ it follows that $r_z = 0$.

For $r_x = \frac{1}{1 + tan^2\,\alpha}$ there is:

$$r_z = r_x \cdot \sqrt{2} \cdot tan\alpha$$

$$r_z = \frac{\sqrt{2} \cdot tan\alpha}{1 + tan^2\alpha}$$

In conclusion the components of $\vec{r}$ are:

$$r_x = \frac{1}{1 + tan^2\alpha}$$

$$r_y = \frac{tan^2\alpha}{1 + tan^2\alpha}$$

$$r_z = \frac{\sqrt{2} \cdot tan\alpha}{1 + tan^2\alpha}$$

To calculate the position of the reflected beam on the screen, the line given by has to be intersected with the plane of the screen:

The equation of the screen plane is:

$$x = d$$

The parameter equation of the line given by $\vec{r}$ is

$$\begin{pmatrix} x \\ y \\ z \end{pmatrix} = \lambda \cdot \begin{pmatrix} \frac{1}{1 + tan^2\alpha} \\ \frac{tan^2\alpha}{1 + tan^2\alpha} \\ \frac{\sqrt{2} \cdot tan\alpha}{1 + tan^2\alpha} \end{pmatrix}.$$

The x-co-ordinate always has to be equal to *L*, this yields:

$$d = \lambda \cdot \frac{1}{1 + \tan^2\alpha}$$

$$\lambda = d \cdot \left(1 + \tan^2\alpha\right)$$

Therefore the co-ordinates of the image point on the screen are:

$$x_i = d \cdot \left(1 + \tan^2 \alpha\right) \cdot \frac{1}{1 + \tan^2 \alpha} = d$$

$$y_i = d \cdot \left(1 + \tan^2 \alpha\right) \cdot \frac{\tan^2 \alpha}{1 + \tan^2 \alpha} = d \cdot \tan^2 \alpha$$

$$z_i = d \cdot \left(1 + \tan^2 \alpha\right) \cdot \frac{\sqrt{2} \cdot \tan \alpha}{1 + \tan^2 \alpha} = d \cdot \sqrt{2} \cdot \tan \alpha$$

And one finally obtains

$$x_i = d$$

$$y_i = d \cdot \tan^2 \alpha$$

$$z_i = d \cdot \sqrt{2} \cdot \tan \alpha$$

Curriculum Vitae

Muhammad Arif

National Institute of Vacuum Science and Technology (NINVAST), National Centre for Physics, Islamabad 44000, Pakistan

E-mail: marif2093@yahoo.com
Office: +92-51-9038200
Cell: +92-345-5334151
Date of Birth: January 02, 1971

Education

2009 – 2011	Master of Science, Physics, Seoul National University, South Korea
1991 – 1995	Bachelor of Science, University of the Punjab, Pakistan

Professional Research Experience

2004 – 2009	Research Assistant, National Institute of Vacuum Science and
2012 – To date	Technology, Islamabad, Pakistan.

Technical Skills

- Laser reflectometry for the study of stuttering target conditions
- In situ assessment of sputtering target surface roughness
- Assessment of target poisoning by laser reflectometry
- Characterization of sputter deposited films
- SEM, XRD, XPS and surface characterization
- Nanowires synthesis: AAO-template assisted growth of metallic nanowires on graphene by electrodeposition
- Nanotubes synthesis: CNTs-wrapped Ni nanotubes by electrodeposition
- Nano and micro-fabrication: Photolithography, metal deposition using thermal evaporator
- Measurements of electron field emission of metallic nanowires and CNTs-wrapped Ni nanotubes

Publications in refereed journals

[1] **Muhammad Arif** and Christoph Eisenmenger-Sittner, Characterization of Aluminum and Titanium nitride films prepared by the reactive sputtering under different poisoning conditions of target, *J. Vac. Sci. Technol. A.* (under review).

[2] **Muhammad Arif** and Christoph Eisenmenger-Sittner, In situ assessment of target poisoning in magnetron sputtering, *Surf. Coat. Technol*., **324** (2017) 345-352 (https://doi.org/10.1016/j.surfcoat.2017.05.047)

[3] **Muhammad Arif**, Thomas Ernstbrunner and Christoph Eisenmenger-Sittner, In situ assessment of the roughness of a uniformly eroded cylindrical magnetron target, *Vacuum*, **138** (2017) 205-212. (https://doi.org/10.1016/j.vacuum.2016.09.015)

[4] Kwang Heo, Byung Yang Lee, Hyungwoo Lee, Dong-guk Cho, **Muhammad Arif**, Kyu Young Kim, Young Jin Choi and Seunghun Hong, Carbon and metal nanotube hybrid structures on graphene as efficient electron field emitters, *Nanotechnology*, **27** (2016) 275301.

[5] **Muhammad Arif**, Kwang Heo, Byung Yang Lee, Joohyung Lee, David H Seo, Sunae Seo, Jikang Jian and Seunghun Hong, Metallic nanowire–graphene hybrid nanostructures for highly flexible field emission devices, *Nanotechnology*, **22** (2011) 355709.

[6] **Muhammad Arif**, Kwang Heo, Byung Yang Lee, Joohyung Lee, David H Seo, Sunae Seo, Jikang Jian and Seunghun Hong, Graphene makes field emission devices flexible and more efficient, Published online as a news item for the new development at the official website of IOP on September 02, 2011. http://nanotechweb.org/cws/article/lab/47076

Oral Presentations

[1] **Muhammad Arif** and Christoph Eisenmenger-Sittner, An in situ assessment of the roughness of a uniformly eroded cylindrical magnetron target, *16th Joint Vacuum Conference & 14th European Vacuum Conference (JVC-6 & EVC-14)*, June 6-10, 2016, Portoroz, Slovenia.

[2] **Muhammad Arif** and Christoph Eisenmenger-Sittner, Investigation of target poisoning in reactive sputtering by optical reflectometry, *20th International Vacuum Congress (IVC-20)*, August 21-26, 2016, Busan, South Korea.

[3] **Muhammad Arif**, Kwang Heo, Byung Yang Lee, Joohyung Lee, David H Seo, Sunae Seo, Jikang Jian and Seunghun Hong, Flexible and transparent field emission devices based on graphene-nanowire hybrid structures, *American Physical Society (APS)*, March Meeting, (2011) Dallas, Texas, USA.

Poster Presentations

[1] **Muhammad Arif** and Christoph Eisenmenger-Sittner, In situ assessment of target poisoning evolution in magnetron sputtering, *15th International Conference on Reactive Sputter Deposition (RSD-16)*, December 1-2, 2016, Ghent, Belgium.